Universität Bonn

Physikalisches Institut

Measurement of the inclusive $Z + b\bar{b}$ cross section in pp-collisions at 7 TeV with ATLAS

Dennis Hellmich

In this thesis, the measurement of the inclusive cross section of the process $Z + b\bar{b}$ is measured where the Z can decay to an electron-positron pair or to a muon-antimuon pair. The analysed data was recorded by the ATLAS experiment in 2011 at a centre-of-mass energy of $\sqrt{s} = 7\,\text{TeV}$ and includes $4.58\,\text{fb}^{-1}$ of proton-proton collisions. The resulting cross sections are unfolded to particle level and compared to LO and NLO predictions from different Monte Carlo generators.

Physikalisches Institut der
Universität Bonn
Nussallee 12
D-53115 Bonn

BONN-IR-2014-06
July 2014
ISSN-0172-8741

Measurement of the inclusive $Z + b\bar{b}$ cross section in pp-collisions at 7 TeV with ATLAS

Dissertation
zur
Erlangung des Doktorgrades (Dr. rer. nat.)
der
Mathematisch-Naturwissenschaftlichen Fakultät
der
Rheinischen Friedrich-Wilhelms-Universität Bonn

von

Dennis Hellmich
aus
Euskirchen

Bonn, 2014

Dieser Forschungsbericht wurde als Dissertation von der
Mathematisch-Naturwissenschaftlichen Fakultät der Universität Bonn angenommen und ist
auf dem Hochschulschriftenserver der ULB Bonn
http://hss.ulb.uni-bonn.de/diss_online elektronisch publiziert.

1. Gutachter:	Prof. Dr. Norbert Wermes
2. Gutachter:	Prof. Dr. Ian Brock
Tag der Promotion:	02.07.2014
Erscheinungsjahr:	2014

"Le seul véritable voyage ne serait pas d'aller vers de nouveaux paysages, mais d'avoir d'autres yeux."

Marcel Proust

Abstract

In this thesis, the measurement of the inclusive cross section of the production of two b-jets in association with a Z boson is measured where the Z can decay to an electron-positron pair or to a muon-antimuon pair. The analysed data was recorded by the ATLAS experiment in 2011 at a centre-of-mass energy of $\sqrt{s} = 7\,\text{TeV}$ and includes $4.58\,\text{fb}^{-1}$ of proton-proton collisions. The resulting cross sections are unfolded to particle level and compared to LO and NLO predictions from different Monte Carlo generators. Relevant systematic uncertainties have been studied. The measurement has been found to be in agreement with NLO predictions within the quoted uncertainties.

Contents

CHAPTER 1

Introduction

It is a simple idea that all kinds of matter are composed of only a few elementary particles. But despite its simplicity, this concept has permitted to explore and successfully describe the structure of matter at smaller and smaller scales. It has led to a formulation of our current understanding of the most fundamental particles and their interactions among each other: the Standard Model (SM) of particle physics. This model is extremely succesful in the description of the phenomena that were observed in a wide range of experiments since the 1970s. It furthermore allowed predictions of missing pieces, the experimental discovery of which constitutes milestones in the history of particle physics. Examples are the discovery of the top quark in 1995 [1, 2] and the tau neutrino in 2000 [3]. A more recent breakthrough and confirmation of the Standard Model is the discovery of a new particle [4, 5] at the Large Hadron Collider (LHC) which is very likely the Higgs boson that has been postulated around 50 years ago [6–11] and that is responsible for the masses of the particles in the SM.

The ATLAS experiment (**A** **T**oroidal **L**HC **A**pparatu**S**) is one of the two large general-purpose detectors which are used to study collisions from the LHC. It is designed to give access to a wide range of physics measurements in high energetic proton-proton collisions. Besides the search for new physics it is also an important task to measure processes which are described within the framework of the SM. This is necessary for the optimisation of theoretical predictions that are based on phenomenological models and also for the understanding of the detector. One crucial process is the production of a Z-boson, a high mass, uncharged particle that is responsible for the neutral weak current. The production of such a boson in association with b-quarks provides an efficient handle to test perturbative QCD predictions. The two leptons are generally high energetic and form an ideal signature for event selection and reconstruction. Furthermore the $Z + b\bar{b}$ process is the dominant background in the production of a Higgs boson together with a Z boson. This is one of the most challenging channels in the search for the Higgs boson and hence a very precise knowledge of the backgrounds is crucial. Even after the discovery of the Higgs boson, this channel remains of particular importance in testing whether its properties, especially its coupling to fermions, is consistent with SM expectations.

This thesis describes the first cross section measurement of a Z-boson in association with

two or more b-quarks at the ATLAS detector [12]. The measurement is based on 4.58 fb^{-1} of proton-proton collisions at a centre-of-mass energy of 7 TeV. The data has been taken between March and October 2011.

This thesis starts with a description of the experimental environment, the ATLAS detector and the LHC (Chapter 2), followed by the concepts that are necessary in understanding the theoretical background of boson and heavy flavour production at hadron colliders in Chapter 3. This chapter also describes the toolkit used to provide simulations and summarises the theoretical predictions that are available. Chapter 4 illustrates the object reconstruction and selection, i.e. the necessary steps to obtain physics objects from raw detector output. Chapter 5 depicts the simulated dataset and the analysed data sample and gives an overview of the event selection. The analysis procedure is described in Chapter 6 and the systematics uncertainties are discussed in Chapter 7. The results are summarised together with the conclusions in Chapter 8. The last chapter concludes with a summary (Chapter 9).

CHAPTER 2

The LHC and the ATLAS experiment

The experimental environment that is utilized in this analysis is the ATLAS detector which is provided with high intensity and high energy collisions of proton beams from the LHC machine. This experimental environment is described in the following chapter.

2.1 The Large Hadron Collider

The LHC (Large Hadron Collider) [13] is a circular particle accelerator designed to accelerate and collide beams of protons [1]. It is located at the European Center for Nuclear Research (CERN) in a tunnel of about 27 km of circumference and is located on average 100 m below ground level. The design centre-of-mass energy of the two colliding beams is $\sqrt{s} = E_1 + E_2 = 14\,\text{TeV}$. The targeted design luminosity[2] is $10^{34}\,\text{m}^{-2}\,\text{s}^{-1}$ and will be achieved by bunches of about 10^{11} protons at a collision rate of 40 MHz.

Before the injection into the LHC, the protons' energy is increased to a value of 450 GeV in a successive series of linear and circular accelerators which are depicted in Figure 2.1: after being accelerated to 50 MeV in the linear collider LINAC 2 the protons pass a chain of circular colliders to increase their energy: Proton Synchrotron Booster (PSB, 1.4 GeV), Proton Synchrotron (PS, 26 GeV) and Super Proton Synchrotron (SPS, 450 GeV).

After the injection into the LHC the bunches of protons are collimated and accelerated to their final collision energy. This acceleration is achieved by eight super-conducting 400.8 MHz cavity resonators per beam providing a gradient of $5.5\,\text{MV}\,\text{m}^{-1}$. To bend the particles on their orbit a system of super-conducting dipole magnets with field strengths of about 8 T is embedded into supra-fluid helium which is cooled down to a temperature of 1.9 K. In addition,

[1] A further operation mode of the LHC is the acceleration and collision of heavy ions with each other and with protons. The collision of heavy ions, however, is not part of this thesis and is therefore only mentioned for the sake of completeness.

[2] The instantaneous luminosity L is a quantity that describes the number of interactions per unit area and time. To obtain the interaction rate $\dot{N}$ the luminosity is multiplied by the cross section σ.

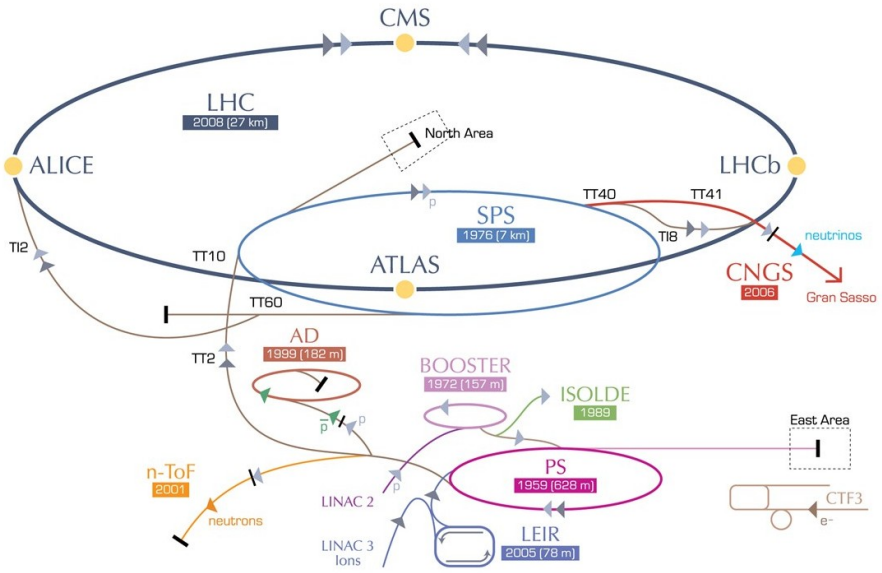

Figure 2.1: The LHC acceleration scheme [14]. After being accelerated to 50 MeV in the linear collider LINAC 2 the protons pass a chain of circular colliders to increase their energy: Proton Synchrotron Booster (PSB, 1.4 GeV), Proton Synchrotron (PS, 26 GeV) and Super Proton Synchrotron (SPS, 450 GeV).

quadrupole and higher multipole magnet systems are used for focusing and correcting the trajectory of the beams.

The first proton beams began circulation in September 2008. After a technical intervention the first collisions at an unprecedented centre-of-mass energy of $\sqrt{s} = 7$ TeV took place in March 2010. The total recorded data in 2010 correspond to an integrated luminosity of 48.1 pb^{-1} and a peak luminosity of 0.21×10^{33} m^{-2} s^{-1}. The dataset that is used in this analysis was recorded in 2011 and contains 5.61 fb^{-1} of data and the peak luminosity was 3.6×10^{33} m^{-2} s^{-1}. After a short maintenance shutdown the centre-of-mass energy was increased to 8 TeV at a peak luminosity of 7.73×10^{33} m^{-2} s^{-1}. In February 2013 the LHC has started a long shutdown scheduled to last until 2015 to prepare the machine for the design centre-of-mass energy of 14 TeV. The number of colliding bunches as a function of time can be seen in Figure 2.2a for the three running periods in 2010, 2011 and 2012.

Such high luminosities are necessary to obtain high collision rates which enable the study of rare physics processes. However, the resulting large number of protons per beam introduces a new difficulty: pile-up. This occurs if two intersecting bunches cause more than one proton-proton interaction. Since hard interactions have a relatively low cross section the contribution from additional interactions (so-called *Minimum Bias interactions*) is usually of very low energy. The exact definition of pile-up varies from experiment to experiment and is comprised of two classes within ATLAS:

- One speaks of *in-time pile-up* if the additional soft collisions occur within the same bunch crossing as the hard process. This causes usually a large number of particles in an event.

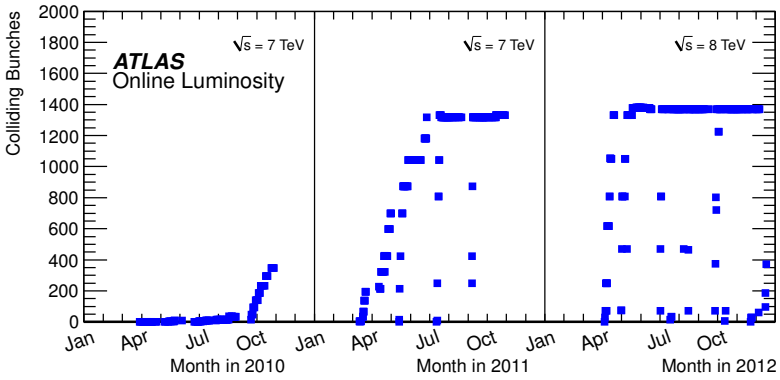

(a) Colliding bunches versus time

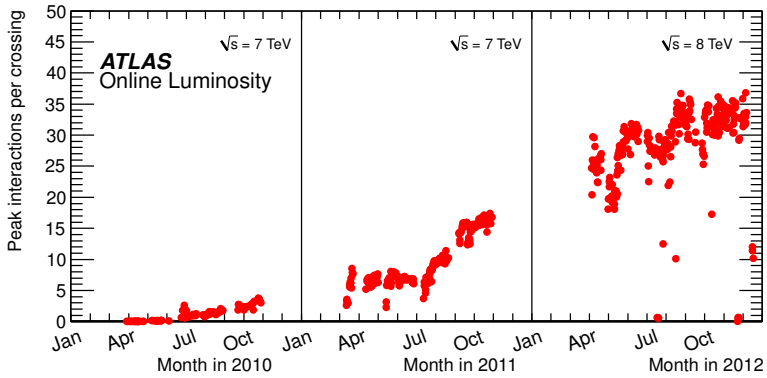

(b) Peak interactions versus time

Figure 2.2: ATLAS collision plots for the years 2010, 2011 and 2012 [15]: (a) Number of colliding bunches versus time, (b) maximum mean number of events per bunch crossing averaged for all crossings in a lumi-block. This corresponds to the peak pile-up.

- On the other hand *out-of-time pile-up* is given by additional interactions from previous bunch crossings that are overlapping into the actual event because of finite integration times of the detector components. This results usually in additional energy depositions in the calorimeters.

Figure 2.2b shows the maximum mean number of events per bunch crossing. It is averaged for all crossings in a Luminosity Block (LB) which corresponds to the basic time-unit for storing luminosity information and has usually a duration of one minute. The plotted quantity describes the peak number of interactions in is therefore a measure for pile-up.

The counter rotating proton beams are brought to collision at four different interaction points which are surrounded by the four large LHC experiments: the two general-purpose detectors ATLAS and CMS, ALICE which was built with focus on heavy-ion collisions and LHCb which is optimized for b-physics.

The ATLAS experiment at which this analysis has been performed is presented in the next section.

2.2 The ATLAS experiment

ATLAS (**A** **T**oroidal **L**HC **A**pparatu**S**) is a general-purpose detector and designed to study a wide range of high energy physics processes. It has an extension of 25 m perpendicular to the beam axis and 44 m along the beam axis and weighs 7000 tons. With the exception of the beam pipe the cylindrically shaped detector surrounds the interaction point almost hermetically. Beginning at the interaction point the particles arising from the collision first traverse the high precision inner detector system consisting of the pixel detector, the SCT and the TRT. Afterwards they pass the electromagnetic and the hadronic calorimeters. The outermost layer is the muon detector. The components that are relevant for this thesis are described in the following sections. For more comprehensive information, see [16].

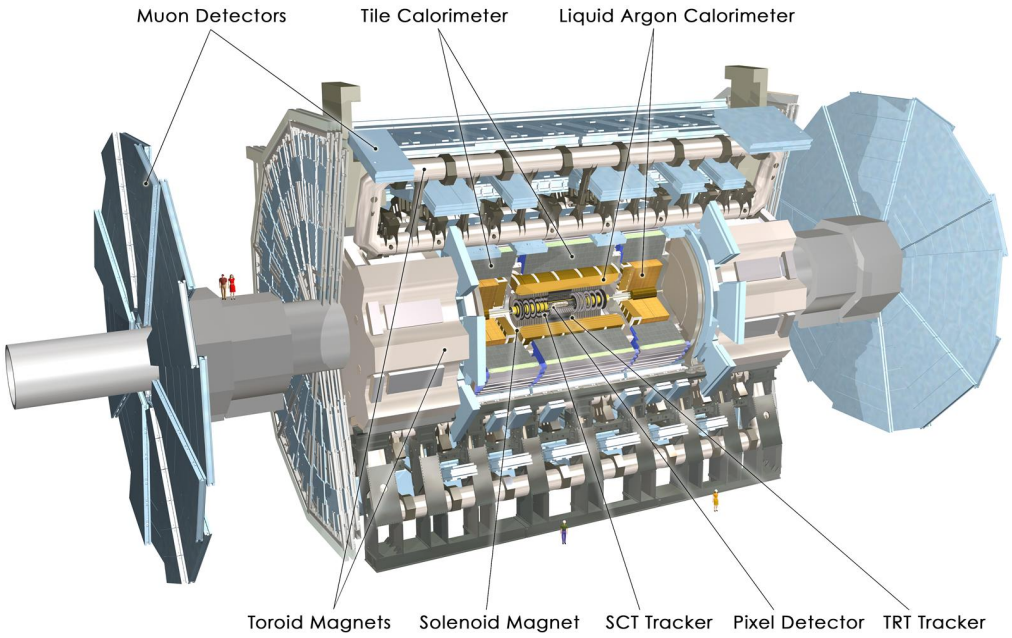

Figure 2.3: A computer generated image of the ATLAS detector [17]

Figure 2.3 shows a computer generated image of the ATLAS detector which illustrates the layout of the detector system. A right-handed coordinate system which has its origin in the interaction point is used in ATLAS. It is defined as follows: the x-axis points to the centre of the LHC ring, the y-axis points upwards and the z-axis points into the direction of the beam pipe. As can be seen from Figure 2.3 the ATLAS detector has a cylindrical symmetry. Hence it is often useful to describe interactions in a cylindrical coordinate system with the distance r to the interaction point, the azimuthal angle ϕ (which is the angle to the x-axis after projection on the $x-y$-plane) and the longitudinal angle Θ (which is the angle to the beam axis projected on the $y-z$-plane. With the three momentum components p_x, p_y and p_z the convenient quantities transverse momentum p_T and transverse energy E_T are introduced:

$$p_T = \sqrt{p_x^2 + p_y^2} \tag{2.1}$$

$$E_T = \sqrt{E_x^2 + E_y^2} \tag{2.2}$$

The rapidity y is defined as:

$$y = \frac{1}{2} \cdot \left(\ln \frac{E + p_z}{E - p_z} \right) \tag{2.3}$$

Differences of two rapidities are invariant under longitudinal Lorentz transformations along the z-direction. It also has the advantage that in hadron-hadron collisions the flux of particles is constant per rapidity-interval. For massless particles or in the limit of very high energies the rapidity becomes approximated by the pseudo-rapidity η which follows directly from using the polar angle $\cos\Theta = p_Z/|p|$ and the relativistic energy-momentum-mass relation $E^2 = |p|^2 + m^2$ (see Equation 2.4). A particle that moves along the direction of the y-axis (i.e. perpendicular to the beam) has $\eta = 0$ and a particle moving into the direction of the z-axis (i.e. parallel to the beam pipe) has infinite rapidity $\eta = \pm\infty$.

$$\eta = -\ln \tan \frac{\Theta}{2} \tag{2.4}$$

Distances between two particles are often described by the quantity ΔR:

$$\Delta R = \sqrt{(\Delta\phi)^2 + (\Delta\eta)^2} \tag{2.5}$$

The detection of neutrinos is a key component for the study of many physics processes. However, they usually don't interact with the detector material and are therefore only indirectly measurable. The total amount of transverse energy in a proton-proton collision is a conserved quantity and a large amount of missing transverse energy is usually a good hint for neutrinos in an event.

2.2.1 Inner detector system

The three innermost detectors around the beam-pipe form the inner detector (ID) system (see Figure 2.4) ranging from radii around the beam pipe of 5.05 cm for the innermost layer of the pixel detector to 1.07 m for the outer edge of the transition radiation tracker (TRT). The pixel detector is surrounded by the semiconductor tracker (SCT) which is surrounded by the TRT. They provide coverage within $|\eta| < 2.5$ ($|\eta| < 2.0$ for the TRT) and full coverage in ϕ. The inner detector is placed inside a solenoidal magnetic field produced by a magnet of field strength 2 T. Under the influence of this magnetic field, charged particle trajectories are bent with a curvature that is directly proportional to the particle momentum.

A key ingredient to this analysis is the accurate knowledge of the primary interaction vertex and of additional possibly displaced secondary interaction vertices. The latter occur if longer lived particles like B-hadrons decay and can be used to discriminate those from short lived particles. The very high efficiency in track reconstructing and momentum resolution are essential for the reconstruction of the exact position of these interaction vertices.

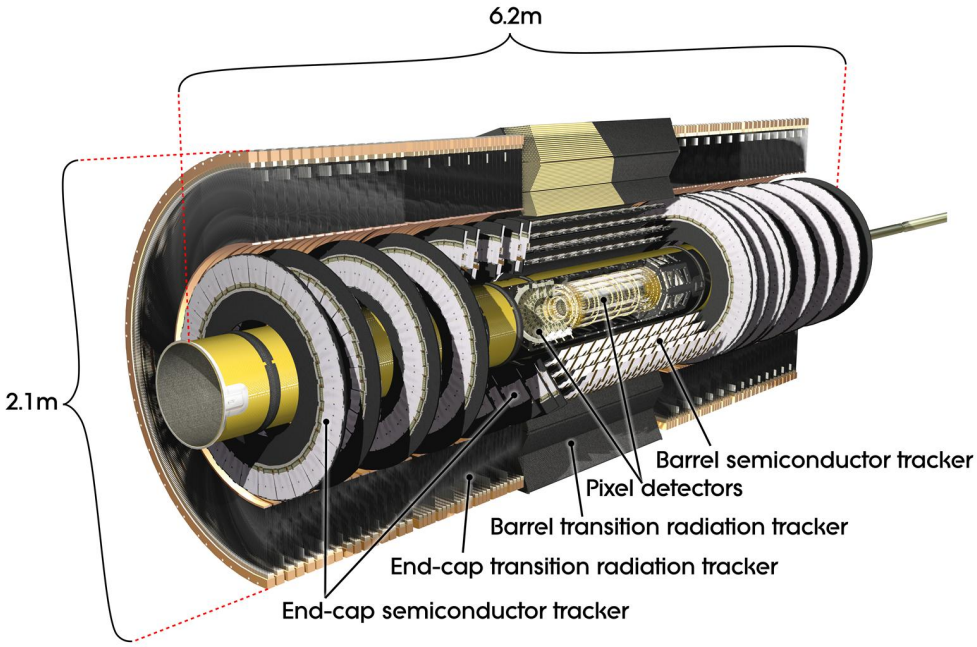

Figure 2.4: A computer generated image of the inner detector system [18].

Pixel detector

The pixel detector is the innermost detector system and the 80 million readout channels represent approximately 80 % of all readout channels of the ATLAS detector. The pixel detector consists of three layers in the barrel region and end-caps on both sides of the detector, each comprising three disks. There are in total 1744 identical modules in the barrel and in the end-caps. Each of these modules has a length of 60.8 mm and a width of 16.4 mm and houses 47232 pixels with a size of 50 µm × 400 µm. Each pixel is part of a 250 µm thick silicon sensor that detects charged particles that pass through the depleted material and create an electron-hole pair. The intrinsic resolution is 10 µm ($R - \phi$) and 115 µm in z (respectively in R for the end-caps). The resolution of the measured primary vertex position in a typical event is 30 µm in the transverse plane and 50 µm in the longitudinal direction [19].

SCT

The silicon strip detector (SCT) is composed of 4088 modules with silicon microstrips. About half of these modules are distributed over four layers in the barrel region and the other half forms the 9 end-cap disks on each detector side. Each barrel module consists of 768 strips with a length of 128 mm and a pitch of 80 µm which are oriented along the beam axis. Each module is two-sided where the backside pair of strips is placed at a small stereo offset angle of 40 mrad to provide position information in the z-direction. The intrinsic resolution of the SCT is 17 µm ($R - \phi$) and 580 µm in z (respectively in R for the end-caps).

TRT

The low number of very precise hits in the two silicon detectors in complemented by a large number of hits (typically 36 per track) in the transition radiation tracker (TRT). It consists of more than 300 000 straw shaped drift tubes with a diameter of 4 mm. In the barrel region they have a length of 144 cm and are mounted along the beam axis and therefore position determination is only possible in the transverse plane. In the end-caps 37 cm long straw tubes are arranged radially. In between the straws radiation material generates transition radiation emitted by electrons and is therefore used for the identification of those. The intrinsic resolution is 130 µm per straw in the $R - \phi$ plane.

2.2.2 Calorimeters

The calorimeter-system is surrounding the inner detector and the magnet that produces the solenoidal magnetic field(see Figure 2.5 for a computer generated image of the calorimeter system). It provides precise energy measurement of particles that are created during the interaction. These are in particular electrons, photons and hadrons. To reconstruct the missing transverse energy in a collision full hermeticity is necessary. Therefore the full coverage in angular direction of the electromagnetic and the hadronic calorimeters are complemented by an additional forward calorimeter that covers the range up to $|\eta| < 4.9$. The functional principle is referred to as sampling calorimetry which means that active detection material and passive absorbing material are alternatingly arranged. This has the consequence that the energy measurement is destructive i.e. the whole energy of the particle should be absorbed by the material. The response of the calorimeter to an electron with respect to a hadron with the same energy is not one. This property of the calorimeter system is called non-compensation and needs to be accounted for in the reconstruction of physics objects.

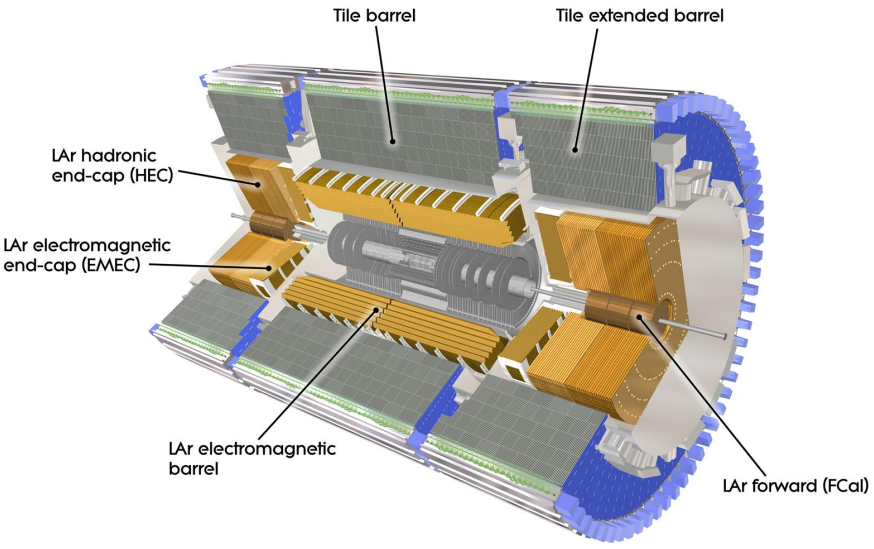

Figure 2.5: A computer generated image of the calorimeter system [20]

Electromagnetic calorimeter

Due to its very fine granularity the electromagnetic calorimeter is very precise. It is divided into a barrel region ($|\eta| < 1.475$) and two end-cap wheels on each side ($1.375 < |\eta| < 3.2$). Both regions are placed in separate cryostats.

This part of the calorimeter is optimized to measure electromagnetic showers from electrons and photons. To achieve this precision it consists of three layers. The thickness integrated over all three sampling layers is > 22 radiation lengths (X_0) in the barrel and $> 24X_0$ in the end-caps. The first layer provides a very fine granularity in η and is called strip-layer. The second layer is the thickest layer (about $16X_0$) within the EM calorimeter and most of the energy is deposited here. The third layer (about $2X_0$) helps to distinguish electromagnetic showers from hadronic showers. The active material in the electromagnetic calorimeter is liquid argon (LAr) and the absorbing material in between is provided by lead plates. It has an energy resolution of $\sigma_E/E = 10\%/\sqrt{E} \oplus 0.7\%$

Hadronic calorimeters

The hadronic calorimeter measures the energy of particles that pass the electromagnetic calorimeter and interact strongly (hadrons). Its design in the barrel differs from that in the end-caps. The central barrel ($|\eta| < 1.0$) and the extended barrel ($0.8 < |\eta| < 1.7$) are using steel as absorber material and scintillating tiles as active region. On the other hand the end-cap calorimeter consists of two wheels that are integrated into the LAr cryostats of the end-caps of the electromagnetic calorimeter. In the end-caps. liquid argon is used as active material, the same choice as for the electromagnetic part of the calorimeter. The absorbers are made of copper. The energy resolution is $\sigma_E/E = 50\%/\sqrt{E} \oplus 3\%$.

The forward calorimeter is also included into the end-cap cryostats. It provides coverage between $3.1 < |\eta| < 4.9$ and uses the combination LAr (active material) and copper/tungsten (absorber). The energy resolution is $\sigma_E/E = 100\%/\sqrt{E} \oplus 10\%$.

2.2.3 Muon spectrometer

The outermost layer (and the largest in volume) is formed by the muon systems. Since typical momenta of muons at the LHC are near the range where energy losses due to ionisation become minimal [21] they leave the calorimeter system almost unaffected whereas all other particles are stopped in the inner parts of the detector. In the muon system, muons are not only detected but also their momentum is measured. For this purpose a toroidal magnetic field of 0.5 T in the barrel (1.0 T in the end-cap) is provided by three superconducting magnets (for $|\eta| < 2.7$). Four different detector types are used: the first two for precise tracking measurements and the other two for trigger purposes. The muon drift tubes (MDT) which are supported by the cathode strip chambers (CSC) are located in the high multiplicity region between $2.0 < |\eta| < 2.7$. They are multiwire proportional chambers with cathodes segmented into strips. For the triggering resistive plate chambers (RPC) are used in the barrel ($|\eta| < 1.05$) and thin gap chambers (TGC) in the end-cap region ($1.05 < |\eta| < 2.7$). The latter two also provide the muon coordinate in direction orthogonal to the MDT and CSC.

2.2.4 Trigger

At the design luminosity of the LHC bunches of protons collide every 25 ns each with 25 proton-proton collisions on average. This corresponds to a 1 GHz event rate. However, only a very small fraction of these events contain high momentum interactions that are interesting for physics analyses. To reduce the number of events that are kept a three-level trigger procedure is applied. In the first level (L1) only a limited amount and granularity of detector information is used to make a decision whether the event processing should be continued or not. It searches for high p_T leptons, jets or photons or for events with a large missing E_T or large $\sum E_T$. By the directions of these objects, regions of interest (RoI) are defined which seed the second trigger level (L2). By using full detector information and highest precision in the RoI's it refines the trigger selection of L1. The event rate is reduced to approximately 70 kHz after L1 and 3.5 kHz after L2. The third trigger level is called event filter (EF). It fully reconstructs the events offline which gives the possibility to apply sophisticated trigger decisions. With an average processing time of 1 s and an event size of one to two MB the required event rate of 200 Hz can only be reached with high-grade parallel computing. All events that pass the EF are written on bulk-storage and are available for offline physics analyses.

2.2.5 Luminosity determination

An essentiel ingredient for any cross section measurement is the accurate knowledge of the delivered luminosity. The luminosity determination in this analysis is based on two detector systems [22]:

- The Beam Conditions Monitor (BCM) consists of four small diamond sensors arranged around the beam pipe. They are located on each side of the interaction point at a distance of $z = \pm 184$ cm.
- LUCID is a Cherenkov detector located at a distance of 17 m on each side of the beam spot. The Cherenkov photons are produced by charged particles passing through gas tubes and are detected by photomultipliers. The detector registers inelastic proton-proton scattering in the η range between 5.6 and 6.0 which is directly correlated with the number of collisions.

CHAPTER 3

Boson and heavy flavour production at LHC

In this chapter the theoretical formulation for hadron-hadron collisions and the relevant physical processes are presented. The current knowledge of the structure of matter at a fundamental level: its elementary constituents and their interactions are described by the Standard Model of particle physics (SM). In this model all matter that can be observed consists of 12 elementary spin $1/2$ particles. These so-called fermions are the three charged leptons electron, muon and tau as well as the corresponding three neutrinos and the six types of quarks labelled as: up, down, charm, strange, bottom and top. Each fermion also has a corresponding antiparticle with opposite charge-like quantum numbers. The interactions among these particles can be described by the exchange of force mediating gauge bosons. The forces relevant for collider experiments are the electromagnetic force mediated by the photon, the weak force mediated by the Z^0 and the $W^{\pm}$ bosons and the strong interaction mediated by the gluons. The electromagnetic and the weak force are combined within the formalism the electroweak theory. Gravitation which is the fourth known force is not incorporated in the SM and is not important in the characteristic length and energy scales regime of high energety particle physics. A comprehensive and detailed description of the Standard Model can e.g. be found in the textbooks [23] and [24].

Unless stated otherwise all masses and energies are given in natural units where the Planck constant $\hbar$ and the speed of light are defined as $c = \hbar = 1$. Therefore the dimensions of frequently used quantities in high energy physics are given in terms of energy. Energies, masses and momenta are written in electron-volt (eV).

3.1 Particle interactions

3.1.1 Perturbation theory and Feynman diagrams

The calculation of cross sections for transformations between particles in an initial state and particles in a final state is based on the idea of integrating the transition probability over an appropriate phase space region. This transition probability is proportional to the squared transition amplitude which is also called matrix element. For a particular process it is defined as a perturbative expansion in the coupling constant of the interaction α, the sum of all possible transition amplitudes each being specified by a mathematical calculation prescription: the so-called Feynman rules which are derived from the Lagrangian of the Standard Model. With the help of these rules interactions between initial and final states can be translated into a graphical representation, the Feynman diagrams. They prescribe a perturbative calculation of the transition amplitude, being proportional to the number of vertices in the diagram. The lowest order in the perturbative expansion corresponds to the diagrams with the smallest number of vertices. For example, Figure 3.1a shows a leading order Feynman diagram for a process called quark pair creation. By including further vertices, higher order corrections are applied (see an example in Figure 3.1b and (c)).

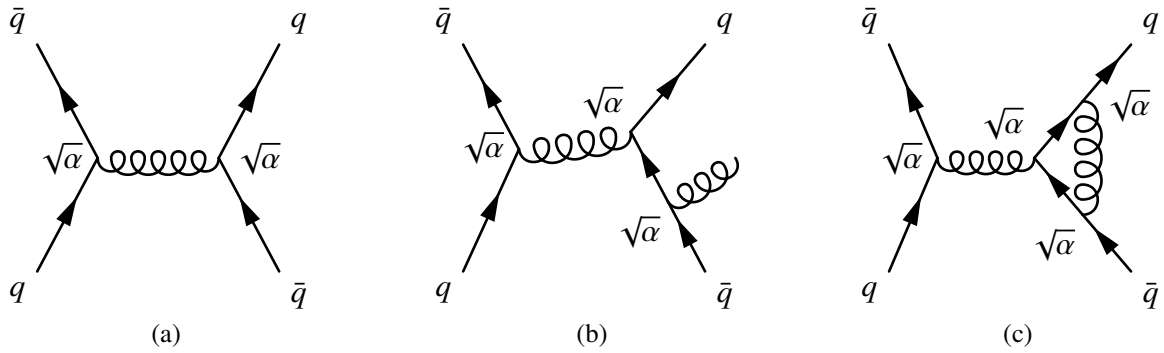

Figure 3.1: Feynman diagram for quark pair creation in (a) leading order (LO), (b) and (c) higher orders of the coupling constant α.

3.1.2 Quantum Chromodynamics

The theory of strong interactions is a non-abelian quantum field theory based on an $SU(3)$ symmetry gauge group. The quantum number in this theory is named colour. It can take three values, by convention referred to as red, green and blue. Hence the theory is named Quantum Chromodynamics (QCD). A characteristic property of this theory is the fact that not only the matter particles, but also the mediators of the force, the so-called gluons, carry a colour charge and therefore interact with each other. As a consequence the strength of the strong force, given by the coupling constant $\alpha_S(Q^2)$ depending on the momentum transfer Q^2, is small at low distances (large momentum transfers) and becomes larger at higher distances (small

momentum transfers). Two opposing phenomena are closely related to these two extreme regimes of momentum transfers. At large distances, the coupling strength becomes so large that no free color charged objects can be observed, but that the elementary quarks and gluons form compound states that are color neutral, the so-called hadrons. This is referred to as confinement. For shorter distances the coupling decreases and the force becomes weaker. This effect is known as asymptotic freedom. For sufficiently small distances coloured particles can almost be treated as free particles and only in this regime perturbation theory becomes applicable. In perturbative calculations, observables that depend on the strong coupling α_S are approximated by the first few terms of an expansion in α_S, which needs to have a sufficiently small value so that higher orders become negligible compared to the experimental uncertainty of the observable considered.

3.1.3 Electroweak theory

The electroweak theory [25–27] is the theory describing the electroweak interactions. It unifies the electromagnetic and the weak force under an $SU(2) \times U(1)$ gauge group with the weak hypercharge Y being the generator of the $U(1)$ group and the weak isospin vector I being the generator of the $SU(2)$ group. Due to a spontaneous symmetry breaking caused by the Brout-Englert-Higgs (BEH) mechanism the Z^0 boson and the photon eigentstate fields are created by mixing the W^0 and the B^0 which are uncharged and massless eigenstates of the initial, unbroken symmetries. The charged W^+ and W^- eigenstate represent the $W^\pm$ bosons. The mixing is characterised by the masses of the $W^\pm$ and Z^0 and is reflected in the weak mixing angle Θ_W:

$$\cos\Theta_W = \frac{m_W}{m_Z} = \frac{g}{\sqrt{g^2 + g'^2}} \tag{3.1}$$

Here g and g' are the group coupling constants associated with $U(1)_Y$ and $SU(2)$.

3.2 Particle collisions at hadron-hadron colliders

Since hadrons are composed of pointlike quarks and gluons, it is these components that scatter when two beams of hadrons are brought to collision. Therefore, in contrast to collisions between leptons that are pointlike particles themselves, in hadron-hadron collisions only a fraction of the hadrons' energies is available in the collision.

According to the strength of the QCD coupling as described in Section 3.1.2 the scattering processes at high energy hadron colliders as described by their momentum transfer can be classified as hard or soft interactions:

- **Hard collisions** can be calculated with high precision using perturbation theory, and
- on the other hand **soft processes** are dominated by non-perturbative QCD effects.

A method to separate the calculations of the high energetic hard interactions from the soft scattering is given by the factorisation theorem [28]. For the cross section of proton-proton scattering to a given final state, denoted by X: $PP \to X$, the matrix elements can be factorised:

$$\sigma(PP \to X) = \sum_{i,j} \int dx_1 dx_2 \; f_{i,P}(x_1,\, Q^2)\; f_{j,P}(x_2,\, Q^2) \cdot \hat{\sigma}_{ij\to X}(x_1 x_2 s,\, Q^2) \tag{3.2}$$

In the summation, all partons i and j that can contribute to the final state X are considered. $\hat{\sigma}_{ij\to X}$ specifies the partonic cross section between the initial state partons i and j. The so-called parton distribution functions (PDF) $f_{i,P}(x_1,\, Q^2)$ and $f_{j,P}(x_2,\, Q^2)$ describe the probabilities to find the partons with the given flavours i and j with the momentum fractions $x_{1/2}$ of the protons. The Q^2 is the momentum scale at which the product-ansatz is performed. A specific choice for this scale is the so-called factorisation scale μ_F which allows to distinguish between hard and soft scattering. Partons above this scale usually contribute directly to the hard interaction while partons below this scale are treated within the PDF. After the factorisation the perturbative expansion is calculated separately in orders of the running coupling constant α_S which is evaluated at the renormalisation scale μ_R:

$$\sigma(PP \to X) = \sum_{i,j} \int dx_1 dx_2 \; f_{i,P}(x_1,\, \mu_F^2)\; f_{j,P}(x_2,\, \mu_F^2) \cdot [\hat{\sigma}_0 + \alpha_S \mu_R^2 \hat{\sigma}_1 + \ldots]_{ij\to X} \tag{3.3}$$

The leading order cross section is denoted as σ_0 and the higher order corrections are σ_1 and so on. Typically, μ_F and μ_R are set equal and chosen to be at the order of the momentum scale of the hard scattering process.

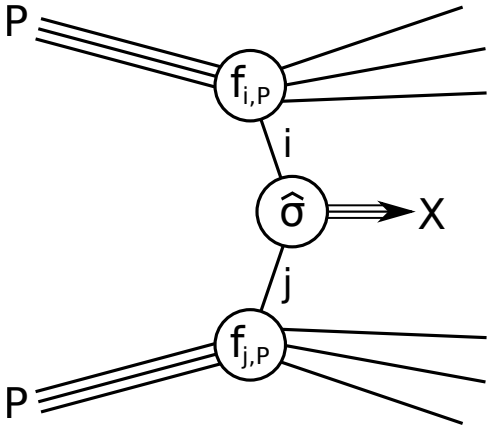

Figure 3.2: Schematic representation of a proton-proton scattering process. Two protons P, each contributing to the interaction by a parton i and j, respectively. The proton remnants that do not interact hard leave the frame at the top and the bottom. The partons i and j carry a fraction of the protons momentum that is being defined by the parton density functions $f_{i,P}$ and $f_{j,P}$ and participate in the hard scattering process defined by the cross section $\hat{\sigma}$ and depicted by the circle in the middle. In this interaction the final state particles X are produced.

Figure 3.2 illustrates such a generic scattering process of two protons. The PDFs describe the soft part and therefore can not be calculated from perturbation theory. However, they were determined from experimental data on deep inelastic scattering obtained at the electron-proton collider HERA at DESY and inclusive jet production studies at the Tevatron. Even though the PDFs themselves are not accessible by perturbative QCD their evolution with the

momentum transfer is. This is achieved by the DGLAP equations [29–32] at scale α_S, provided the measured distributions at a particular scale, chosen e.g. as $\alpha_S(m_Z)$. There are several sets of PDFs from different working groups differing amongst others in the experimental data that is used, the parametrisations of x, the treatment of heavy quarks and the value of α_S. An example for parton density functions labelled MSTW2008 [33] is shown in Figure 3.3 for two factorisation scales $Q^2 = 10\,\mathrm{GeV}^2$ and $Q^2 = 10^4\mathrm{GeV}^2$.

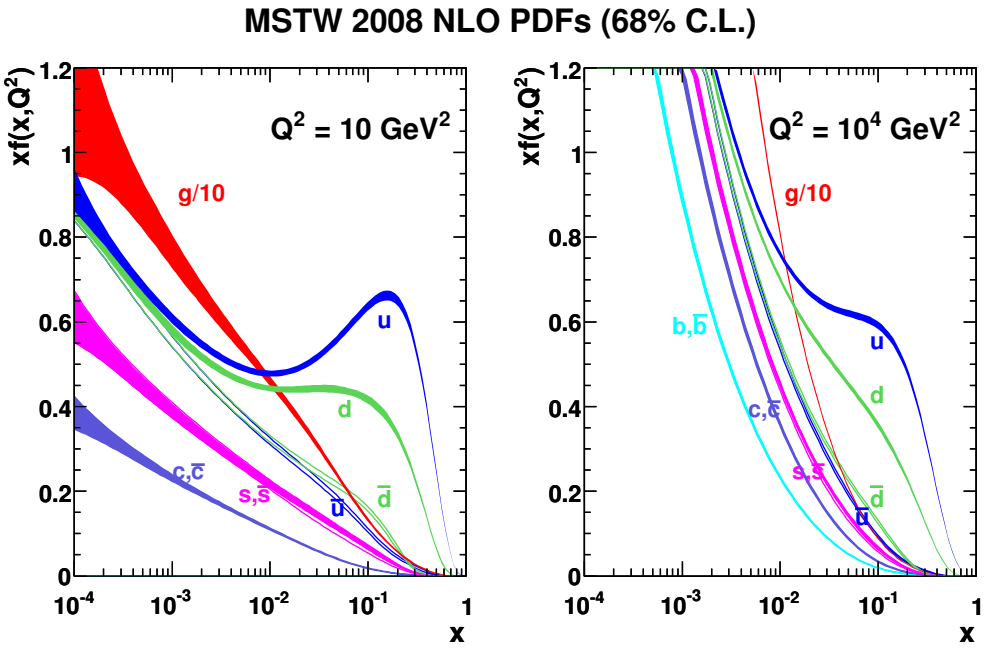

Figure 3.3: Parton distribution functions (PDF) for the proton for factorisations scales $Q^2 = 10\,\mathrm{GeV}^2$ and $Q^2 = 10^4\mathrm{GeV}^2$ determined for the MSTW2008 PDF set. Figure taken from [33]

A further aspect of hadron collisions is the so-called Underlying Event (UE) which refers to accompanying soft interactions that are involving partons from the proton remnants that are not contributing to the hard interaction. Most of these interactions have a very low transverse momentum and therefore add only few energy depositions in the detector. But in addition hard interactions may occur and can contribute in the form of multiple parton interactions (MPI). Both effects need to be quantified and studied in detail. A measurement of the characteristics of the UE at the ATLAS experiment can be found in [34].

The partonic cross section $\hat{\sigma}_{ij\to X}$ as given in Equation 3.3 is calculated in a pertubation expansion in the coupling constants. As mentioned before, the order in perturbation theory corresponds to the number of vertices in the Feynman diagrams. The first non-trivial order in the perturbation series is named leading order (LO), the next expansion is next-to-leading order (NLO). Typically these calculations become already very complex at this stage and only for few processes the next-to-next-to-leading order (NNLO) calculations are available. However for certain phase space regions, like the collinear parton splitting or radiation of a soft gluon from a parton, higher orders can not be neglected. To treat those the so-called method of parton showers is utilised. It starts from the matrix element final state partons and applies

iteratively $1 \rightarrow 2$ branchings. The probability that no resolvable splitting occurs between the two energy scales Q_{init} and Q_{split} is expressed by the Sudakov form factors [35]. Due to the stepwise decreasing energy scale the coupling α_S becomes larger and larger and at some cut-off scale $Q_{cutoff} \approx 1\,\text{GeV}$ the branching becomes non-perturbative and the evolution process terminates.

In a next step, the final partons undergo hadronisation. This requires phenomenological models for the non-perturbative transition between partons and hadrons. There are two models available:

- The **string model** [36] is based on the idea that partons are connected by a colour string. For example, in the production of a quark-antiquark pair the potential energy between the two particles increases linearly with their distance and the gluonic string is stretched. When the potential energy is of the order of the hadron masses it becomes energetically more favourable to produce additional quark-antiquark pairs where the original quark is connected to the new antiquark and vice versa. When additional gluons are present the string connection depends on the colours of the participating partons and is usually formed with the gluon in the middle. This causes a kink on the string the sharpness of which depends on the momentum of the gluon.

- The **cluster model** is based on a property of QCD called preconfinement: at energy scales much below the hard scale the partons in the shower are clustered into colour-neutral groups. These clusters subsequently decay into the visible mesons and baryons.

3.3 Production and decay of weak gauge bosons

The force carriers of the weak interaction are the neutral Z^0-boson and the charged $W^{\pm}$-boson. The so-called Drell-Yan process [37] describes the dominant production of a lepton-antilepton pair by quark-antiquark annihilation via the exchange of a gauge boson (see Figure 3.4). As a consequence of the electroweak unification the neutral exchange particle can also be virtual photon $\gamma*$ instead of the Z boson. The Drell-Yan process is of particular importance at hadron colliders because it is theoretically calculable and can be experimentally measured with high precision due to its copious occurrence.

The full decay width of the Z boson and the W boson are $\Gamma_Z = (2.4950 \pm 0.0023)\,\text{GeV}$ and $\Gamma_W = (2.085 \pm 0.042)\,\text{GeV}$ respectively [21]. Both the W and the Z can decay leptonically or hadronically as listed in Table 3.1. The only fermion that is excluded as a decay product is the top quark whose large mass exceeds the masses of the W and Z.

Figure 3.5 shows the expected cross section as a function of the centre-of-mass energy for various physics processes in pp- and $p\bar{p}$-collisions. The cross section for the production of a Z^0 boson is about six orders of magnitude lower than the total cross section.

For this thesis the neutral current processes including a Z^0 boson are more important than those with a $W^{\pm}$ boson. Therefore the focus of the following sections is placed on the production of the Z^0 boson with additional quarks or gluons.

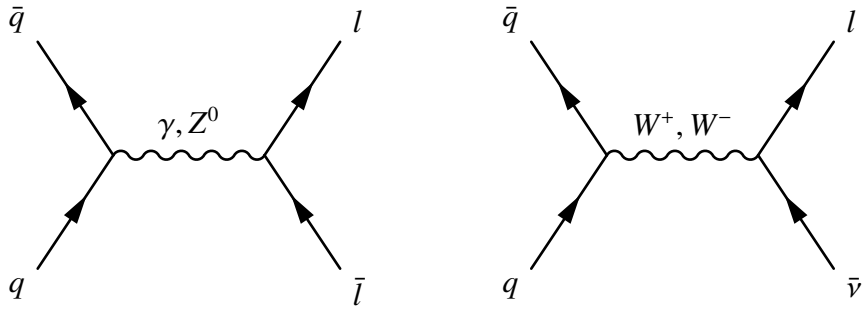

(a) $Z^0/\gamma*$ production (b) $W^\pm$ production

Figure 3.4: Leading order Feynman diagrams for the production of a $Z^0/\gamma*$ or $W^\pm$ boson via the Drell-Yan process and the subsequent leptonic decay.

Table 3.1: Characteristic properties of the Z^0 and the $W^\pm$ bosons [21]. The mass, width and the dominant decay modes are summarised.

Z^0-boson	
$m_Z = (91.1876 \pm 0.0021)\,\text{GeV}$	
$\Gamma_Z = (2.4950 \pm 0.0023)\,\text{GeV}$	
Decay mode	Branching ratio [%]
e^+e^-	3.363 ± 0.004
$\mu^+\mu^-$	3.366 ± 0.007
$\tau^+\tau^-$	3.370 ± 0.008
invisible	20.00 ± 0.06
hadronic	69.91 ± 0.06
$W^\pm$-boson	
$m_W = (80.385 \pm 0.015)\,\text{GeV}$	
$\Gamma_W = (2.085 \pm 0.042)\,\text{GeV}$	
Decay mode	Branching ratio [%]
$e^+\nu$	10.75 ± 0.13
$\mu^+\nu$	10.57 ± 0.15
$\tau^+\nu$	11.25 ± 0.20
invisible	1.4 ± 2.9
hadronic	67.60 ± 0.27

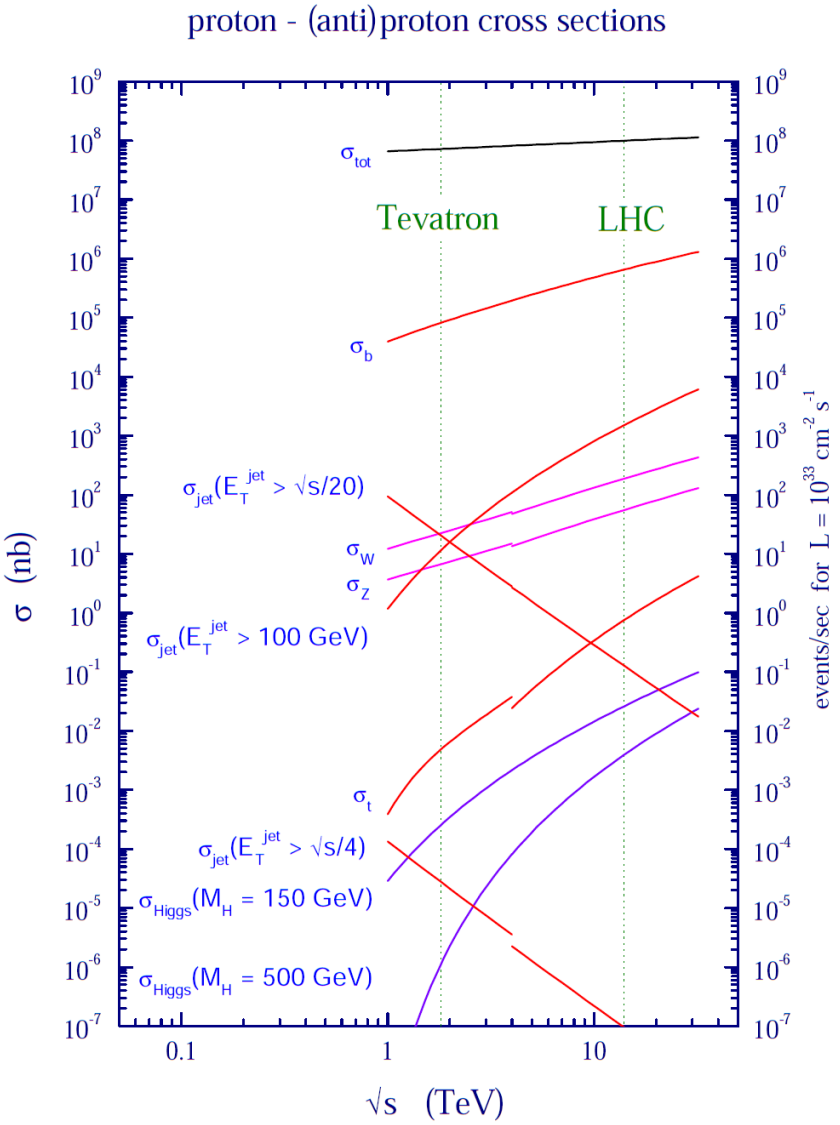

Figure 3.5: Expected event rates and cross sections for various physics processes as a function of the centre-of-mass energy. The gap at $\sqrt{s} = 4\,\text{TeV}$ is caused by the transition from proton-antiproton (Tevatron) to proton-proton collisions (LHC). [38]

3.4 Z+jets production

The measurement of the final state cross section of a Z^0 boson in association with additional quarks or gluons that are detected as hadron jets is of particular importance. Not only is it a background to many physics searches (including the $Z + b\bar{b}$ production that is described in this thesis), but it is also a stringent test for perturbative QCD calculations.

Some Feynman diagrams for leading order production of a Z^0 boson with one and with two additional jets are given in Figure 3.6. Any of these processes can also be transformed to higher

jet multiplicities by adding initial state and final state radiation.

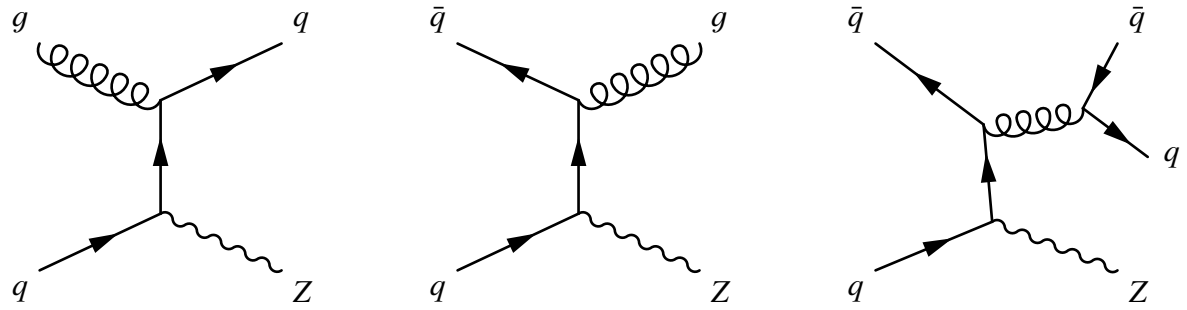

(a) $Z + q$ production (b) $Z + g$ production (c) $Z + q\bar{q}$ production

Figure 3.6: Leading order Feynman diagrams for the production of a Z^0 boson in addition with one and two additional partons.

At ATLAS the cross section for a Z^0 boson in addition to jets has been measured up to a jet multiplicity of seven [39]. The cross section decreases by a factor of about four when going from Z to Z + 1jet to Z + 2jets etc. The special case when the the Z^0 boson is produced in association with heavy jets is of particular interest when studying perturbative QCD and provides information about heavy flavour content of the proton.

3.5 $Z + b\bar{b}$ production

An important sub-process of the Z+jets production that is described in the previous section is the production of a Z^0 boson with additional b-jets. b-jets occur when final state bottom quarks hadronise into b-hadrons. A characteristic property of b-hadron is relatively large lifetime which results in a displaced decay vertex and hence provides the possibility to distinguish b-jets from light jets [1] (see Section 4.5). Besides the fact that a reliable identification of b-quarks is an experimental difficulty, a challenging aspect is the much lower cross section of $Z + 1b$ compared to Z+light jets.

Theoretical calculations for the production of Z^0 bosons in association with b-quarks can be performed in two different approaches that are classified by the underlying PDF. In the fixed flavour scheme only PDF's for the four lightest quarks and the gluon are used. b-quarks in the final state can therefore only arise from gluon splitting. The corresponding production processes for Z^0 plus two b-quarks for gluon-gluon fusion are shown in Figure 3.7a. With a frequency of 80 % [40] this is the dominant production mechanism at the LHC [2]. Of less importance at the LHC setup is the quark-antiquark annihilation as shown in Figure 3.7b.

[1] Light jets collectively refer to jets arising from up-quark, down-quark, strange-quark and gluons.

[2] At the Tevatron accelerator this process contributed only to 30 % of the production rate because due to the lower centre-of-mass energy the gluon luminosity was lower. In addition at Tevatron protons were colliding with antiprotons and hence antiquarks are available as valence quarks.

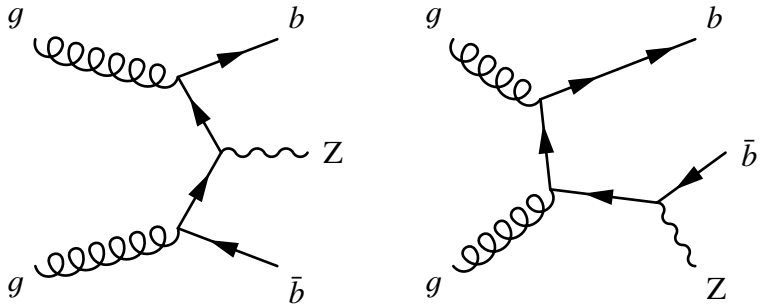

(a) gluon-gluon fusion

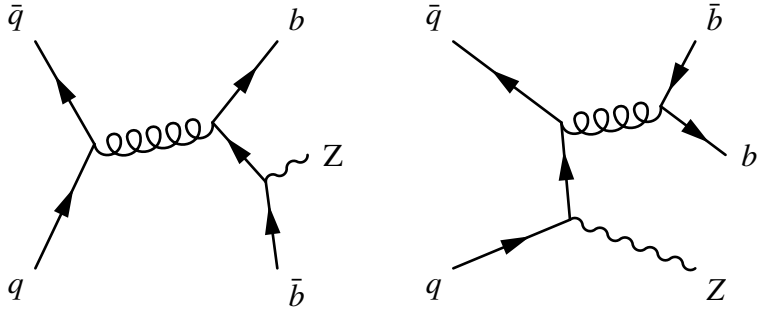

(b) quark-antiquark annihilation

Figure 3.7: Feynman diagrams for the production of a Z^0 boson in association with two b-quarks. The dominant production process (a) is the gluon-gluon fusion, the minor production process (b) is the quark-antiquark annihilation.

An improvement to the 4-flavour-number scheme (4FNS) is the so-called variable-flavour scheme or five-flavour-number scheme (5FNS). It allows the direct occurrence of the b-quark in the incoming protons and therefore processes like the one in Figure 3.6 become possible if the kinematic constraints are fulfilled. While both approaches can give very different results at LO in QCD it has been shown that they become consistent at NLO ([41]).

Theoretical calculation of the production of $Z + b\bar{b}$ processes have been performed at NLO with the approximation of a vanishing bottom-quark mass [42]. These calculations form the basis for theoretical predictions of the $Z + b\bar{b}$ cross section with the MCFM tool [43] as it will be discussed in Section 3.7. In addition, calculations with non-zero bottom-quark masses were performed [41, 44] for the Tevatron and the LHC for $\sqrt{s} = 14\,\text{TeV}$ and $\sqrt{s} = 10\,\text{TeV}$.

The most recent calculation additionally includes off-shell effects of the Z^0 boson and hence full spin correlations of the final-state leptons are retained [40]. The predicted cross section for the $l^+l^-b\bar{b}$ process is evaluated at a centre-of-mass energy of $\sqrt{s} = 7\,\text{TeV}$ as $\sigma = 9.66\,\text{pb}$ at LO and $\sigma = 16.1\,\text{pb}$ at NLO where l can be any charged lepton including τ-leptons. The relative contribution of events with three or more b-jets is 0.6 %. These calculations have been included into the aMC@NLO event generation framework which enables the determination of the cross section with identical phase space requirements as used in this analysis. Details are presented in Section 3.7.

Even though the results of the different theory predictions are compatible with each other the uncertainties are large and a precise measurement of the $Z + b\bar{b}$ final state is therefore a

crucial benchmark for the different theoretical approaches and a constraint on b-quark PDF's. Moreover, $Z + b\bar{b}$ is the dominant irreducible background to a Higgs boson produced in association with a Z^0 boson because the light Higgs boson is predominantly decaying into $b\bar{b}$ pairs [45]. Additionally, $Z + b\bar{b}$ is a background for supersymmetric Higgs models. But also SM measurements with similar signatures (like top-pair production in dileptonic final states or diboson processes) can benefit from a precise measurement of this channel.

3.6 Monte Carlo simulation and event production

A widely used tool in particle physics is the Monte Carlo (MC) simulation of high energetic particle collisions as an approximation of theoretical models. The comparison between data and the predictions given by such simulation tools is an essential method in measurements and searches. The first level in a chain of simulation steps is the generation of particle four-vectors for specific physics processes. There are currently three classes of tools available:

- Multi-purpose generators (like PYTHIA [46] and HERWIG [47]) cover a wide range of physics processes at leading order. Higher orders are approximately taken care of by the parton shower.
- Multi-leg generators provide exact tree-level matrix element calculations for up to six partons in the final state. Examples are ALPGEN [48] and SHERPA [49].
- NLO generators (e.g. MC@NLO or POWHEG) are based on matrix element calculations including the full NLO corrections and therefore include the radiation of an additional parton with exact tree-level calculations and virtual loop corrections.

The following list provides a short overview of the MC event generators that are used in this thesis:

- **PYTHIA** is a leading order multi-purpose generator describing hard interactions as well as soft interactions such as parton showers in the initial and in the final state and simulation of the underlying event. For hadronisation the string model is used (see Section 3.2). PYTHIA is available in two versions which differ significantly in the underlying implementation. In this thesis PYTHIA 6 is used.
- **HERWIG** is another leading order multi-purpose event generator. It contains initial and final state radiation, hadronisation (cluster model, see Section 3.2) and parton showering. For the generation of multiple parton interaction scattering events HERWIG can be interfaced to JIMMY [50]. The original implementation of HERWIG is based on Fortran. An updated version implemented in C++ is also available and named HERWIG++ [51].
- **ALPGEN** is a tree-level matrix element generator for a fixed number of final state partons which are described without virtual corrections. The evaluation of the matrix element is giving a more correct description for processes with large transverse momenta in high jet multiplities than the parton shower approach in PYTHIA or HERWIG is able to provide. Since ALPGEN does not calculate parton showers and hadronisation it has to be

interfaced to e.g. PYTHIA for this purpose. However in such a combination a theoretically equivalent parton can be created by the parton shower. The procedure to combine these complementary approaches is called matching. The approach that is used within ALPGEN is called MLM matching [52].

- **SHERPA** is another multi-parton generator. Compared to ALPGEN a different matching scheme called CKKW matching is implemented within SHERPA.

- **MC@NLO** [53] is a next-to-leading order generator for hadronic processes. For the showering MC@NLO is interfaced to HERWIG and to avoid double counting the events can have negative event weights. This has to be considered in all succeeding steps of the analysis.

- **POWHEG** [54–56] is like MC@NLO another NLO generator which overcomes the occurence of negative weights by generating radiations sorted by their transverse momentum.

- **MCFM** [43] is a parton-level perturbative QCD Monte Carlo program which gives results for a series of processes including those resulting in final states with W- and Z-bosons with additional heavy quarks.

- **EvtGen** [57] is an event generator optimised for B-hadron physics. It has been tuned with the latest results of the high precision B factories and therefore gives a very precise description of B decays.

- **AcerMC** [58] is a parton level generator designed to simulate hard interactions for a number of SM background processes in pp-collisions. Matrix element calculations are provided by using the MADGRAPH package. For initial and final state radiation, simulation of the underlying event and hadronisation it has to be interfaced to multi-purpose generators like PYTHIA or HERWIG.

- **aMC@NLO** [59] is a framework combining tools that perform cross section calculations, event generation and matching to event generators. It is based on MadGraph 5 [60], a tree-level ME generator, for the event generation and the parton shower matching is based on the MC@NLO formalism.

The generation of the particle four vectors for a given physics process is just the first step in the MC event generation chain at ATLAS. It is followed by the event simulation in which the particle interaction with the detector is simulated. A full simulation is applied using the GEANT4 [61] simulation package[3]. In a next step the energy depositions and other material interactions of the simulation step are transformed to simulated detector output. The output of this so-called digitisation is stored as Raw Data Objects (RDO) the same way it is also done during real data taking. The subsequent steps are performed for simulated data as well as for

[3] Beside the CPU intensive full simulation provided by GEANT4 a fast simulation based on ATLFAST II is possible. This has the disadvantage that some detector components and their interactions with the particles may not be modelled as precisely as with the full simulation.

real collision data: the reconstruction of tracks and energy clusters from detector readout, the creation of analysis objects and finally the creation of files in the so-called D3PD format which are accesible within the ROOT framework [62].

3.7 Theoretical predictions for the $Z + b\bar{b}$ cross section

The measured results from data are compared to several theory predictions. A comprehensive and technical description can be found in [63].

A next-to-leading order perturbative QCD prediction is obtained from MCFM. The implemented MCFM process number 51 allows the calculation of the production of a Z^0 boson (or virtual photon) in association with a $b\bar{b}$ pair both being produced within the acceptance region. The bottom quark mass is neglected. The calculations were carried out in the five-flavour scheme using three different sets of PDF: MSTW08 [33], CT10 [64] and NNPDF2.3 [65]. The spread of the predictions arising from different PDF sets is used as a systematic uncertainty. The renormalization and factorisation scales are set to the quadratic sum of the invariant mass of the Z boson and its transverse momentum on an event-by-event basis. To assess an uncertainty on the scale choice, μ_F and μ_R are indepedently scaled up and down by a factor of two. A further effect of the uncertainty of α_S is obtained from using different PDF sets with α_S being shifted up and down by one σ around the central value. For a comparison to the data, the parton level results obtained from MCFM need to be corrected to the particle level by taking into account several effects:

- The QED final-state radiation is obtained with PHOTOS [66, 67] being interfaced to the ALPGEN +HERWIG +JIMMY samples used in the data analysis.
- The effects of hadronisation, underlying event and multiple parton interactions are quantified by correction factors obtained from both PYTHIA and SHERPA. Differences between these correction factors are assigned as systematic uncertainty.

Another NLO prediction has been found using aMC@NLO which is implemented in the MadGraph 5 framework. This prediction is based on the 4FNSwith the MSTW2008 PDF set and incorporates b-quarks masses. A similar prediction using aMC@NLO has been performed for an associated $Z + 1b$ analysis in the 5FNSand the approximation of massless b-quarks: the minimal set of final states which is well defined at NLO containing $Z+1b$ is $Z+$jet. This is why the $Z+ \geq 1$-jet process is used as the underlying process. From this sample, the $b\bar{b}$ selection is processed after generation. HERWIG++ is used to simulate hadronisation, underlying event and MPI in both cases. For the aMC@NLO predictions no systematic uncertainties were estimated. However it is assumed that the uncertainties obtained from MCFM correctly represent the uncertainties for these calculations.

Beside the NLO predictions described above, ALPGEN and SHERPA were used to calculate the $Z + b\bar{b}$ cross section. ALPGEN is used for the standard analysis sample as described in Section 5.2 and uses the 4FNS. SHERPA uses the CT10 PDF set in the 5FNS.

All predictions are performed using the same phase space definition that is used in this analysis as described in Section 5.2.3. The predictions that were obtained as described above

are summarised in Table 3.2. The effect of the variation of the PDF set for MCFM is about 10 %. Furthermore it can be seen that the inclusion of the b-mass in the aMC@NLO $Z + b\bar{b}$ increases the cross section prediction. The aMC@NLO Z+jet prediction is relatively lower since after requiring a second jet it misses an order in perturbation theory and is therefore only comparable to leading order predictions. As expected the LO prediction from ALPGEN results in a very low predicted cross section. Since the major contribution of $Z + b\bar{b}$ events is coming from the matrix element, which in turn is almost independent of the flavour scheme, no strong dependence on the choice of the flavour scheme is expected. This is confirmed by the fact that differences due to the calculational order or the treatment of the b-mass are dominating and no clear dependence of the flavour scheme is observable.

Table 3.2: Theory predictions for the total fiducial cross sections in comparison. Errors from the MC statistics are quoted for all generators. For MCFM, the second uncertainty is the sum in quadrature of all systematic theory uncertainties.

	Generator	PDF set	FNS	$\sigma(Zbb)$ prediction in [fb]
NLO	MCFM	MSTW2008	5	$413 \pm 8\ ^{+57}_{-58}$
	MCFM	CT10	5	$386 \pm 4\ ^{+55}_{-50}$
	MCFM	NNPDF23	5	$423 \pm 9\ ^{+67}_{-51}$
	aMC@NLO Zbb	MSTW2008	4	485 ± 7
	aMC@NLO Zj	MSTW2008	5	314 ± 9
LO	SHERPA	CT10	5	421.6 ± 2.3
	ALPGEN	CTEQ6L1	4	316.9 ± 1.8

CHAPTER 4

Object reconstruction

In this chapter the reconstruction of detector output like energy depositions in the calorimeter system or cell hits in the inner detector into higher-level physics objects are described.

4.1 Primary vertex

An important issue in hadron-hadron collisions is the precise knowledge of the primary interaction vertex, the event vertex. In the presence of pileup many interaction vertices can exist within the same event. In the environment of this analysis values of up to 20 reconstructed vertices can arise per event. The number of vertices is correlated with the level of pileup and is therefore used to adjust the amount of pileup in Monte Carlo simulation to that in running conditions (see Section 5.2.2).

The primary vertex is determined using an iterative vertex finding approach. First a vertex seed is found by searching for a maximum in the distribution of z-coordinates of all tracks. In a second step the vertex position is determined by fitting the tracks and at the same time down-weighting outlying tracks. Incompatible tracks seed a new vertex and the procedure is repeated until all tracks in the event are associated or no further vertices can be found.

The tracks fulfil a list of quality requirements [19]:

- Transverse momentum $p_{\mathrm{T}} > 150\,\mathrm{MeV}$,
- transverse impact parameter $d_0 < 4\,\mathrm{mm}$,
- impact parameter uncertainty $\sigma(d_0) < 5\,\mathrm{mm}$,
- uncertainty on the longitudinal impact parameter $\sigma(z_0) < 10\,\mathrm{mm}$,
- at least four hits in the SCT detector and
- at least six hits in the pixel and SCT detectors.

The event vertex candidates are required to have at least three associated quality tracks. The vertex candidate with the largest p_{T} is chosen as primary vertex. Events that have no vertex with at least three associated tracks are rejected.

4.2 Muons

4.2.1 Muon identification and reconstruction

Several muon identification strategies are used in ATLAS. There are in particular two different families, called Muid and Staco, of which in this analysis only the latter is used and will be described here. As described in Section 2.2 muons can be measured in the inner detector (ID) and in the muon spectrometer (MS). This permits different muon definitions and reconstruction methods:

The simplest approach is the so-called **standalone** method that builds tracks from track segments found in all three parts of the muon spectrometer. The flight direction of the muon is obtained by extrapolating the track back to the beam line. For **segment tagged** muons, ID tracks are extrapolated to the innermost layer of the MS and matched to nearby segments. All kinematic information of the track is reconstructed from the ID measurement only. This method is particularly useful for muons with low transverse momentum that would not traverse the second station of the MS. For **combined muons** an independent track reconstruction is performed in the ID and in the MS. Resulting track segments are then matched by weighting the difference between outer and inner track vectors by their covariance matrix.

4.2.2 Muon selection

In this analysis Staco muons are used. It has been found that combined muons have the best momentum resolution and the highest purity and are therefore used in this analysis. The following selection criteria are applied to obtain muon candidates in this analysis:

- Transverse momentum greater than 20 GeV,
- $|\eta| < 2.5$,
- a longitudinal distance to the primary vertex of $|z_0| < 1\,\mathrm{mm}$, and an impact parameter significance $|d_0/\mathrm{cov}(d_0)| < 3$,
- quality criteria on the inner tracks as listed on page 27,
- isolation: $\sum p_{\mathrm{T}}(\mathrm{track})/p_{\mathrm{T}}(\mathrm{muon}) < 0.1$ where the sum extends over all charged-particle track momenta in the inner detector within a cone of $\Delta R < 0.2$ around the muon, excluding the track of the muon itself.

A data-MC comparison for the leading and sub-leading muon can be found in Figure 4.1. It is generated after the signal selection as described in Section 5.1.

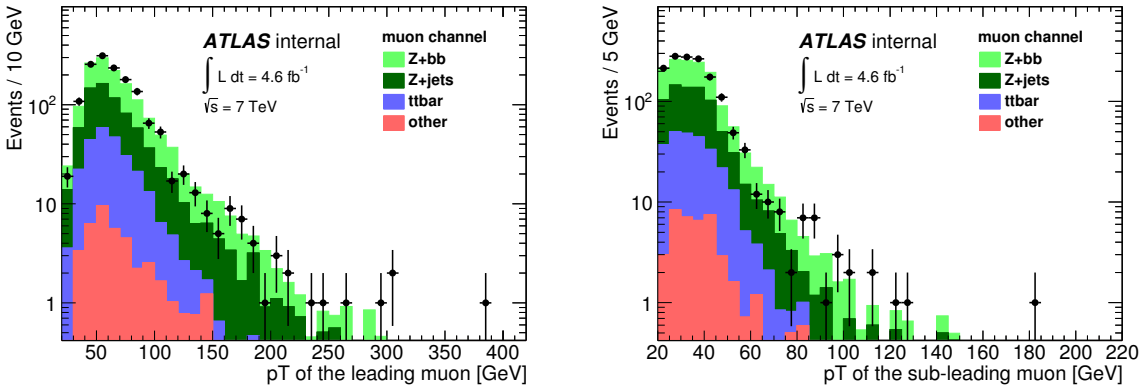

(a) Leading muon

(b) Sub-leading muon

Figure 4.1: Data-MC comparison for the p_{T} of the leading and sub-leading muon after $Z + b\bar{b}$ signal selection. The distribution for $Z + b\bar{b}$ is normalised according to the cross section measurement that was performed in this analysis. All other distributions are normalised according to the MC prediction.

4.3 Electrons

4.3.1 Electron identification and reconstruction

An efficient electron reconstruction algorithm is necessary to reduce the background which is approximately 10^5 larger caused by falsely identified jets. A detailed description of all used algorithms can be found in Ref. [68]. The following section summarises the electron reconstruction method that is used in this thesis. All methods are described for the central region ($|\eta| < 2.47$). Similar methods are also available for the forward region but are not relevant in the context of this analysis.

The basic idea for finding an electron candidate is the identification of energy deposits (clusters) in the electromagnetic calorimeter that are matched to tracks in the ID. For the cluster finding a sliding window algorithm is used. This algorithm forms rectangular clusters with a size of 3×5 cells[1] in the middle layer of the electromagnetic calorimeter by maximising the energy within the window. The position of this rectangular cluster is used to match extrapolated tracks within $\Delta\eta \times \Delta\phi = 0.05 \times 0.10$. In the case of several matched tracks, those with a higher number of silicon hits (i.e. hits in the Pixel and SCT) are preferred. For the energy measurement a larger window with a size of 3×7 cells is used. Energy losses due to the material in front of the calorimeter as well as energy leakage beyond the EM calorimeter and outside the cluster is estimated and taken into account in the energy determination.

In addition to this preselection three different sets of selection cuts were developed within ATLAS each providing an operating point classified by the electron identification efficiency and background rejection [2]. The **loose** electron identification requires certain criteria to be met on the shower shape variables based on the EM middle layer and on hadronic leakage which

[1] One unit corresponds to a size of $\Delta\eta \times \Delta\phi = 0.025 \times 0.025$ which is given by the granularity of the calorimeter.
[2] The rejection is usually defined as the inverse efficiency and is commonly used for background quantifications.

is given by the ratio of E_{T} in the ECAL over E_{T} in the first layer of the HCAL. The **medium** electron identification is based on several criteria in addition to the loose identification. It uses the shower width from the EM strip layer and has refined requirements on the track quality and track-cluster matching. The electron identification efficiency is expected to decrease by about 10 % whereas the jet rejection increases by a factor of four when using the medium electron selection (see Table 4.1). A **tight** selection is also implemented but it is not used in this thesis. A refined set of electron identification has been developed incorporating improved performance for higher pile-up environment. Those are labelled as **loose++**, **medium++** and **tight++**.

Table 4.1: Expected electron efficiencies and jet rejection for the different sets of identification cuts (from [69]). The numbers are evaluated for electrons with $E_T > 20\,\mathrm{GeV}$ and $\eta < 2.5$ on a $Z \to ee$ inclusive MC sample.

Cut	Efficiency (%)	Jet rejection
Reco	97.58 ± 0.03	91.5 ± 0.1
Loose	94.32 ± 0.03	1065 ± 5
Medium	90.00 ± 0.03	6840 ± 70
Tight	71.59 ± 0.03	$(1.39 \pm 0.45) \cdot 10^5$

4.3.2 Electron selection

In this analysis electrons fulfilling the medium++ quality criteria are selected. The subsequent list of criteria are applied to select electron candidates:

- Transverse momentum greater than 20 GeV,
- $|\eta| < 2.47$ to avoid edge effects at the outer boundaries of the ID,
- excluding the transition region between barrel and end-caps ($1.37 < |\eta| < 1.52$),
- a longitudinal distance of the electron track to the primary vertex of $|z_0| < 1$ mm and
- an impact parameter significance $|d_0/\sigma(d_0)| < 10$,

A data-MC comparison for the leading and sub-leading electron can be found in Figure 4.2. It is generated after the signal selection as described in Section 5.1.

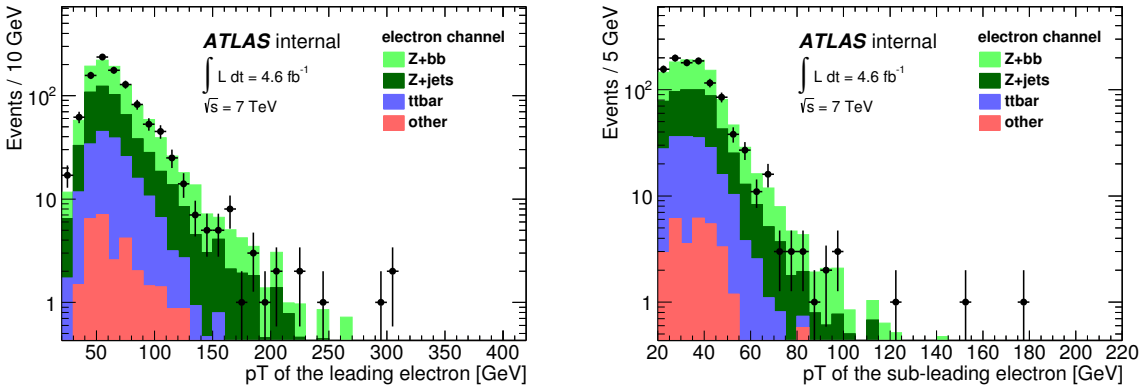

(a) Leading electron

(b) Sub-leading electron

Figure 4.2: Data-MC comparison for the p_{T} of the leading and sub-leading electron after $Z + b\bar{b}$ signal selection. The distribution for $Z + b\bar{b}$ is normalised according to the cross section measurement that was performed in this analysis. All other distributions are normalised according to the MC prediction.

4.4 Jets

4.4.1 Jet reconstruction

As explained in Section 3.2, partons can not exist in an unbound state and hence hadronise. In addition, via the process of parton showering a large number of particles is created, for which the average direction and the total energy are correlated to the direction and energy of the initial parton. To approximately reconstruct the properties of the final state partons it is therefore possible to utilise their correlation with the kinematics of the hadrons in the final state by defining a clustering algorithm. The output of this so-called *jet algorithm* are objects with physical quantities like direction and energy and are called *jets*. Since the jet algorithm is defined in a very general way it can use partons, hadrons and also detector signals like energy depositions in the calorimeter as input.

The jet algorithm that is used in this analysis is the anti-k_{T} algorithm [70] with a jet radius parameter $R = 0.4$. The input to the algorithm are three-dimensional topological calorimeter clusters [71]. The jet finder is implemented in the FastJet package [72, 73] that reduces the algorithmic complexity for the jet clustering from N^3 to $N \log(N)$ and thus enables the use of clustering algorithms in hadron collisions with high jet multiplicities.

The anti-k_{T} jet algorithm is a variation of the k_{T} algorithm [74, 75] and makes use of the transverse momentum of the input objects. For two given objects i and j a distance measure is defined as

$$d_{ij} = \min\left(k_{T,i}^{2p}, k_{T,j}^{2p}\right) \cdot \frac{(\Delta R)_{ij}^2}{R} \tag{4.1}$$

with the transverse momentum $k_{T,i}$ of the object i with respect to the beam direction, the jet radius parameter R, an arbitrary parameter p and the distance ΔR in η and ϕ. In addition a

reference distance is defined as:

$$d_i = k_{T,i}^{2p} \tag{4.2}$$

With these definitions the following rules are applied for two given objects i and j:

1. if $d_{ij} < d_i$, merge the objects i and j,
2. if $d_{ij} > d_i$, the object i is a jet,
3. repeat this procedure until all objects are merged into jets.

The merging of several objects is prescribed by the recombination scheme which in ATLAS simply is the sum of the four-momenta.

For the specific value of $p = 1$ the jet algorithm is called k_T algorithm and for the case of $p = -1$ it is called anti-k_T algorithm. The advantage of the anti-k_T algorithm compared to the k_T algorithm is the regular shape of the final jets and the robustness against soft radiation. In addition, all jet finders that are defined in the illustrated way fulfil the theoretical requirements of *collinear* and *infrared safety*. These requirements are equivalent with the set of reconstructed jets being independent of the collinear splitting of any object (e.g. parton splitting) and independent of the emission of soft objects (e.g. soft gluon radiation).

4.4.2 Jet energy calibration

Several calibration schemes with different level of complexity have been developed in the ATLAS collaboration [76]. All of these calibrations have in common that they start with calorimeter cells that are initially calibrated using test-beams of electrons [77]. However, the shape and the density of electromagnetic showers are different compared to hadronic showers. The jets are formed directly from these clusters (as described in the previous section) and they are said to be at the electromagnetic (EM) scale. In addition, the clusters are calibrated before the jet finding to achieve a better energy resolution. The method is called local cell weighting (LCW) and classifies clusters according to the shower depth and energy density as electromagnetic or hadronic. For hadronic showers energy corrections are derived from simulated pion events. Further corrections address instrumental effects like the non-compensation of the calorimeter, energy losses in dead material and noise thresholds.

In a four step procedure the jets are corrected from the EM- or LCW scale to the final energy scale:

1. **Pile-up correction**: The principal approach of this correction is to calculate the amount of transverse energy that is originating from pileup. This offset is estimated as a function of the number of primary vertices and the expected number of interactions per bunch-crossing μ and subtracted from the jet energy. This method is derived from MC simulations and is able to treat both in-time and out-of-time pileup.
2. **Origin correction**: The direction of the jet is changed such that it points back to the primary interaction vertex of the event instead of the nominal centre of the detector.

3. **Energy correction**: Based on simulated dijet events the jet energy is corrected as a function of p_T and η.

4. **Residual in-situ corrections**: In contrast to the other calibration steps the in-situ corrections are based on data events and makes use of the p_T balance between the jet and an additional reference object (e.g a Z-boson in Z+jet events). These corrections are only applied to data events.

The jet energy scale that is obtained with this calibration procedure is called EM+JES (LCW+JES) for clusters at EM-scale (LCW-scale) as jet inputs.

4.4.3 Jet selection

As already mentioned above, this analysis uses the AntiKt jet algorithm with a distance parameter $R = 0.4$. The jets are calibrated using the EM+JES prescription and if not stated otherwise are required to have a transverse momentum of greater than 20 GeV. Even though jet identification at ATLAS is established within $|y| < 4.5$, this analysis uses the reduced rapidity range $|y| < 2.4$ because the identification of b-jets (see Section 4.5) is only applicable in this range. To suppress jets originating from additional primary vertices, caused by pileup events, the so-called jet vertex fraction (JVF) is used. This quantity is defined as the p_T sum of all tracks from the jet that are associated to the primary vertex divided by the p_T sum of all tracks from the jet. If no track can be associated to the jet JVF has a value of -1. In this analysis jets are only selected when they fulfil $|\text{JVF}| > 0.75$.

Electrons in particular, but also muons, deposit a certain amount of energy in the calorimeters and therefore lead to a misidentified jet. To reduce the impact of this object overlap all jets that are within $\Delta R < 0.5$ to a signal lepton are removed.

Additional jet quality criteria are introduced to remove jets that are associated to energy depositions resulting from hardware problems, LHC beam conditions and cosmic-ray showers [78].

4.5 Identification of b-jets

One important instrument in this analysis is the robust identification of jets originating from bottom-quarks. There are several algorithms implemented within the ATLAS software most of which exploit the relatively long lifetime of the hadronised bottom-quarks[3] which is about 1.5 ps. As a consequence, a high energetic b-hadron travels a significant distance before decaying: the average flight path length is of the order of a few mm. A b-jet identification algorithm is usually benchmarked by two characteristic quantities: the efficiency ϵ_b that a jet originating from a b-quark is tagged and the mistag rate (the probability of wrongly tagging a jet originating from a light parton as a b-jet). Two approaches are used to analyse such event topologies [79]:

[3] There are also b-tagging algorithms that exploit the decay of b-hadrons to muons but this so-called soft muon tagger (SMT) is not important in this analysis.

- **Impact parameter (IP) based algorithms:** the impact parameter of a track is the closest distance to the primary vertex. It can be defined in the transverse plane ($r-\phi$ projection) and in the longitudinal projection (in z direction). The best performing b-tagging algorithm of this class is **IP3D**. It is combining both, the transverse and the longitudinal impact parameters and their correlations by using a log-likelihood ratio (LLR) where the IP significances for each track are compared to specific distributions for b-, c- and light jets obtained from simulation.

- **Vertex reconstruction algorithms:** a more sophisticated approach is the explicit reconstruction of the b-decay vertex. To reconstruct this secondary vertex, an iterative procedure is used, in which all two-track vertices are combined into a single inclusive vertex. Poorly reconstructed tracks are removed until a good χ^2 of the vertex fit is reached. The mass of the vertex is calculated and used as a criterion to reject tracks originating from the decay of long-lived particles (like K_S mesons or Λ baryons) or interactions with the detector material (e.g. photon conversions). The **SV0 tagger** uses the decay length significance $L/\sigma(L)$ (the ratio of the weighted distances between primary vertex and the secondary vertices and the spatial uncertainty) of the reconstructed secondary vertex (see [80]). Further discrimination between b-, c- and light flavour jets is given by the invariant mass of the set of charged particles associated to the reconstructed secondary vertex. This mass is denoted as *SV0 mass*. The **SV1 tagger** uses a likelihood ratio with a set of variables to discriminate between b-jets and other jets. These variables are the invariant mass of all tracks associated to the secondary vertex, the ratio of the energy sum of the tracks associated to the secondary vertex over the energy sum of all tracks associated to the jet and the number of two-track vertices. The **JetFitter** algorithm makes use of the decay structure of the b-hadron that is usually followed by at least one other decay of a c-hadron. With this method the two secondary vertices are not necessarily merged when they fulfil the structural requirements of the decay chain even if they consist only of a single track. In addition to the variables used by IP3D, the flight length significance L/σ_L and some further track variables are used. Those variables are used within a neural network trained to separate b-jets, c- and light jets. The probabilities of the corresponding jet flavour hypotheses are P_b, P_c and P_l. A common variable to discriminate between b-jets and light-jets is $\ln(P_b/P_l)$. To discriminate between b-jets and charm jets a similar variable is used: $\ln(P_b/P_c)$.

In addition, both classes of algorithms can be improved by evaluating a lifetime sign that is negative for secondary vertices behind the primary vertex as seen from the jet direction and positive for secondary vertices that lie within the jet cone. Since decays with negative lifetime sign are kinematically strongly suppressed, a better discrimination can be achieved by the additional sign.

Due to the lower number of tracks stemming from secondary vertices as compared to the event vertex, the efficiency of reconstructing secondary vertices is lower than that of reconstructing primary vertices. This disadvantage however, is compensated by better mistag rate. In order to achieve the best performance, algorithms from both approaches are combined. The combination of the two likelihood ratio taggers IP3D and SV1 can easily be obtained

by summing the two individual weights. The resulting tagger is named **IP3D+SV1**. By extending the neural network inputs of the JetFitter algorithm with the output weight of IP3D the **IP3D+JetFitter** combination is obtained. Similar probabilities of the jet flavour hypothesis (P_b, P_c, P_l) and the combinations of those ($\ln(P_b/P_l)$, $\ln(P_b/P_c)$) as given by the JetFitter algorithm are also defined for the IP3D+JetFitter.

Another widely used combination at ATLAS is called **MV1** using the output weights of IP3D, SV1 and IP3D+JetFitter as input in a neural network.

A plot that shows the light-jet rejection as a function of the b-jet tagging efficiency for selected algorithms is shown in Figure 4.3.

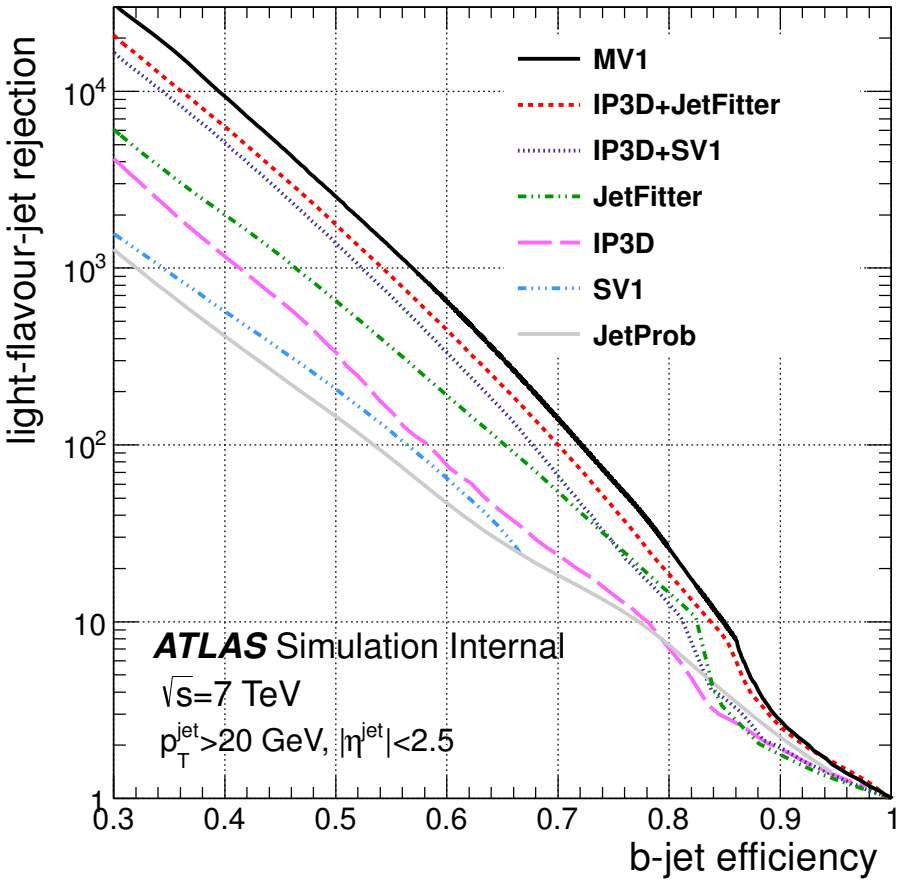

Figure 4.3: Light-jet rejection as a function of the b-jet tagging efficiency for various tagging algorithms [79]. Jets from simulated $t\bar{t}$ events with $p_T > 20\,\text{GeV}$ and $|\eta| < 2.5$ were used.

All the b-tagging methods that are described above, are sensitive to mismodelling of the discrimination variables in the simulation. To compensate for this the b-tag and the c-tag efficiency as well as the mistag rate have been measured in data events with several complementary methods. The resulting calibrations are applied as scale factors to the Monte Carlo. One class of methods to measure the b-tagging efficiency are exploiting jets containing muons [81]. Those jets are very likely originating from semi-leptonic b-hadron decays and therefore provide an

enriched b-jet sample. The p_T^{rel} method uses the momentum of the muon perpendicular to the direction of the combined jet/muon axis. This variable is tending towards higher momenta for muons from b-hadron decays. The efficiency is then obtained by fitting the p_T^{rel} spectra for b-, c- and light jets to the data-distribution with and without applying the b-tagging cut. The second method uses a system of eight linear equations that is obtained by three independent selection criteria: the investigated b-jet classifier, $p_T^{rel} > 700\,\text{MeV}$ and the requirement of at least one other jet with a secondary vertex having a signed decay length significance greater than one. This leads to eight observables (including the measured b-tag efficiency) that can be obtained by solving the linear equations using a χ^2 minimisation. Correlations between the three selections are expected to be small but are taken into account by a set of correlation coefficients within the equation system.

In addition to these dijet-based calibration methods another physics scenario is used for measuring the b-tagging efficiency: $t\bar{t}$ events [82]. Since the branching fraction of $t \to Wb$ is very close to one, $t\bar{t}$ events are an instrument to obtain b-jets that are not restricted to semileptonic decays as jets in the dijet methods are. Due to detector acceptance effects, the observed b-jet multiplicity can be smaller than two. Also additional b-jets can be produced e.g. caused by gluon splitting. The tag counting method extracts the b-tagging efficiency by fitting the expected b-jet multiplicity in $t\bar{t}$ events to the observed b-jet multiplicity. The second method is called kinematic selection and measures the b-tagging rate of the leading jet in $t\bar{t}$ events. Both methods can be evaluated in the semileptonic and in the dileptonic $t\bar{t}$ decay channels. The third method, the kinematic fit, exploits the masses of the W bosons and the top quarks as constraints. This method can therefore only be applied in the semileptonic decay channel because the occurrence of two neutrinos in the dileptonic channel results in an under-determined event topology reconstruction.

4.6 Missing transverse energy

The individual colliding protons carry almost no momentum transverse to the beam axis. As a consequence, because of momentum conservation in the transverse plane, the total transverse momentum per event can be assumed to be zero. Missing transverse energy is defined by the amount and direction of the p_T imbalance and can result from undetectable particles like neutrinos. The negative vector sum of momenta of all particles in an event is denoted as $\vec{E}_T^{miss}$. The magnitude of this quantity is E_T^{miss}. There are several problems that complicate the calculation of the missing transverse energy like the limited detector coverage and finite resolution, dead channels and noise. A detailed review of the E_T^{miss} calculation and performance can be found in [83] and a short overview is given in this section.

For the calculation of the missing transverse energy the cells in the calorimeter with $|\eta| < 4.5$ that are associated to physics objects are summed. The association to the physics objects is necessary because the energy calibration of the associated objects is used. They are assigned in the following order:

- Electron term $E_T^{\text{miss},e}$: cells in clusters that are associated to electrons passing the medium selection with $p_T > 10\,\text{GeV}$.

- Photon term $E_T^{\text{miss},\gamma}$: same for photons passing a tight selection (see [84]).
- τ term $E_T^{\text{miss},\tau}$: same for hadronically decaying τ-leptons passing a tight selection scheme (see [85]).
- Jet term $E_T^{\text{miss,jets}}$: cells that are in clusters associated to jets calibrated at the LCW+JES scale with $p_T > 20\,\text{GeV}$.
- Soft-jet term $E_T^{\text{miss,softjets}}$: cells that are in clusters associated to jets with $7\,\text{GeV} < p_T < 20\,\text{GeV}$.
- Muon term $E_T^{\text{miss},\mu}$: energy of the muons that is deposited in the calorimeters.

All cells that have a significant non-noise energy deposition at LCW calibration scale are summed up in $E_T^{\text{miss,CellsOut}}$-term. Each term is calculated as the negative sum of calibrated cell energies assigned to the physics objects:

$$E_x^{\text{miss}} = -\sum E_i \sin\Theta_i \cos\phi_i \tag{4.3}$$

$$E_y^{\text{miss}} = -\sum E_i \sin\Theta_i \sin\phi_i \tag{4.4}$$

Since muons leave only a minor part of their energy in the calorimeters the muon term is complemented by the p_{T} measurement from the tracks for $\eta < 2.7$. Depending on whether the muon is isolated from jets (i.e. $\Delta R(\mu, \text{jet}) > 0.3$) or not, only the track term or a combination of both terms is used.

The final $E_{x/y}^{\text{miss}}$ term is the sum of the terms described above. The absolute value and direction are calculated from the x- and y-components as:

$$E_T^{\text{miss}} = \sqrt{\left(E_x^{\text{miss}}\right)^2 + \left(E_y^{\text{miss}}\right)^2} \tag{4.5}$$

$$\phi^{\text{miss}} = \arctan\left(E_x^{\text{miss}}, E_y^{\text{miss}}\right) \tag{4.6}$$

Figure 4.4 shows the transverse energy distribution of the E_T^{miss} terms in data events after the final signal selection. In both channels there is no contribution from the $E_T^{\text{miss},\gamma}$ term and only a small contribution from $E_T^{\text{miss},\tau}$ and $E_T^{\text{miss},\mu}$ term. The dominating contributions are given by the $E_T^{\text{miss,jets}}$ terms and in the electron channel furthermore by the $E_T^{\text{miss},e}$.

It should be noted here that badly reconstructed jets can bias the calculation of E_T^{miss}. For this reason all events that contain jets that do not fulfil the jet quality criteria are rejected.

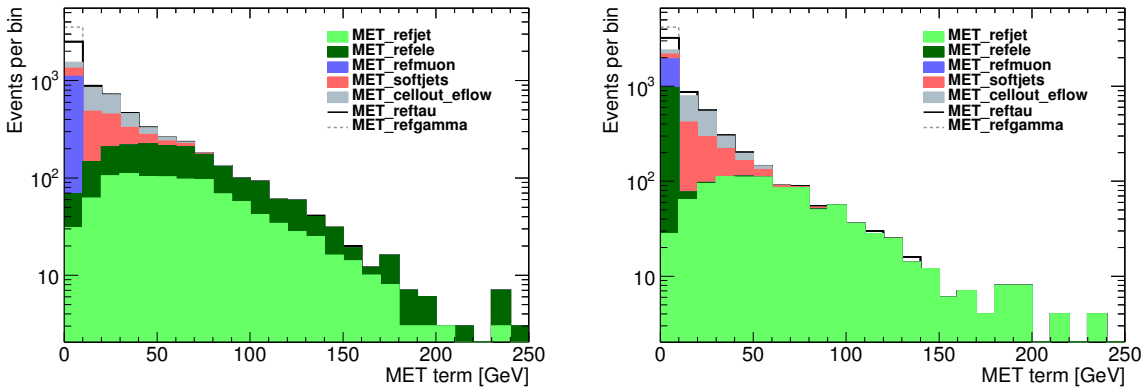

(a) Electron channel

(b) Muon channel

Figure 4.4: Distribution of the transverse energy for the E_T^{miss} terms for data events after signal event selection.

CHAPTER 5

Data sample and Monte Carlo simulation

5.1 Data sample and event selection

The datasets that are analysed in this thesis were collected between March and October 2011 at a centre-of-mass energy of 7 TeV with the ATLAS detector. All analysed data is collected from proton-proton collisions with stable LHC beams. In addition the data have to pass a strict quality control which evaluates the data based on quality flags that are related to error free detector operation of the relevant systems. In the so-called Good Run List (GRL) each luminosity block is listed that fulfils the required criteria. The total amount of available good quality data corresponds to an integrated luminosity of $4.58\,\text{fb}^{-1}$ [22]. The data is grouped into data periods D to M that are characterised by the run conditions like for instance the instantaneous luminosity. A summary of the used data periods can be found in Table 5.1. This analysis is performed in the final state with two electrons and in the final state with two muons. In the following, these are labelled as "electron channel" and "muon channel" respectively. Events in both channels are classified into different so-called streams. This classification is done by a set of unprescaled online triggers which are fully efficient and looser than the triggers used in this analysis. Hence the selection criteria of the streams are not described in more detail here.

In the electron channel the trigger used (EF_2e12_medium) is a di-electron trigger requiring at least two electrons in $|\eta| < 2.5$ with $E_T > 12\,\text{GeV}$ per event. In the later data periods the collision rate increased and as a consequence additional tighter cuts had to be included into the L1 trigger. This change in the L1 seed is marked with an additional 'T' respective 'vh' in the trigger name (see Table 5.1 and refer to [86] for more details). In the muon channel a single muon trigger (EF_mu18_MG) with an E_T threshold of 18 GeV is used. With higher luminosities the L1 trigger threshold has been increased and this change is labelled with the additional suffix 'medium' in the trigger name [87]. The triggers in both channels require different lepton multiplicities. The reason behind this different treatment is that trigger efficiencies for the

corresponding di-muon trigger are not available at ATLAS.

Table 5.1: Summary of the collected data with periods grouped according to the applied trigger. Information is given separately for the electron channel and the muon channel.

Channel	Periods	Luminosity [fb^{-1}]	Trigger
$Z \to ee$	D - J	1.64	EF_2e12_medium
	K	0.57	EF_2e12T_medium
	L - M	2.37	EF_2e12Tvh_medium
$Z \to \mu\mu$	D - I	1.42	EF_mu18_MG
	J - M	3.16	EF_mu18_MG_medium

The following description of the event selection is based on the reconstruction and selection of physics objects as described in Section 4. Collision events are required to have at least one good primary vertex. The event must contain exactly two selected oppositely charged leptons: two electrons in the electron channel or two muons in the muon channel. If any additional lepton passing all the selection requirements is found a veto is imposed on the event and therefore an overlap between the two channels is excluded. With the so-called trigger matching it is furthermore checked that the two selected leptons can be spatially associated to the leptons that fired the trigger signal. In the next step it is ensured that the two-lepton system corresponds to the decay products of a Z^0 boson by requiring that the invariant dileptonic mass m_{ll} is between 76 and 106 GeV. To further suppress the contribution from top pair background events an upper limit on the missing transverse energy of $E_T^{\text{miss}} < 70\,\text{GeV}$ is applied. At least two selected jets tagged as b-jets with the MV1 algorithm at an efficiency of 75 % are required. The given operation point corresponds to a cut on the b-jet tagging weight of $w_{\text{MV1}} > 0.4042$.

A data-MC comparison for the leading and sub-leading b-tagged jet can be found in Figure 5.1.

Table 5.2 shows the number of data events after each selection step for the electron and the muon channel. The fraction of events containing a Z^0 boson and three b-tagged jets is 2.3 % (3.0 %) of the signal events for the electron (muon) channel. The constribution from these events is negligibly low and only listed for completeness.

5.2 Monte Carlo simulation of signal and background events

Data events are compared with Monte Carlo simulation in order to study the physics phenomena. In this analysis the signal as well as the background events are simulated and a good modelling of both is essential for a comprehensive understanding of the measurement.

The Z + jets events, both in the electron and in the muon channel, are simulated using ALPGEN v2.13 for the matrix element calculation using the CTEQ6L1 PDF set [88]. HERWIG

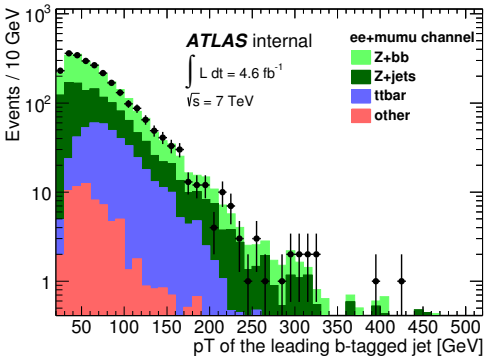

(a) Leading b-tagged jet p_{T}

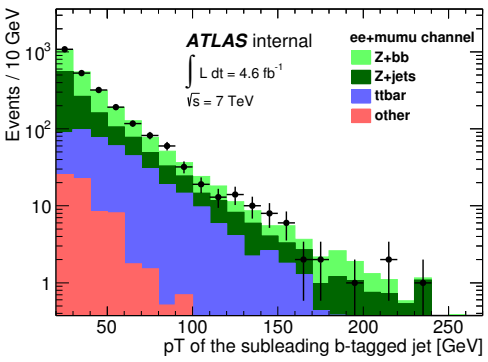

(b) Sub-leading b-tagged jet p_{T}

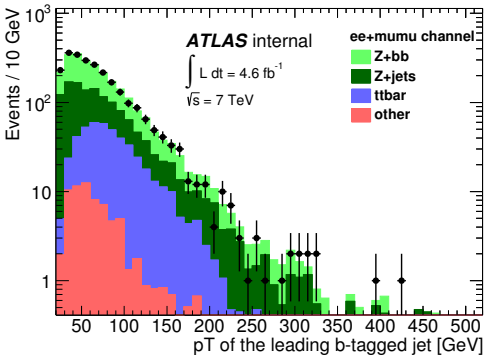

(c) Rapidity of the leading b-tagged jet

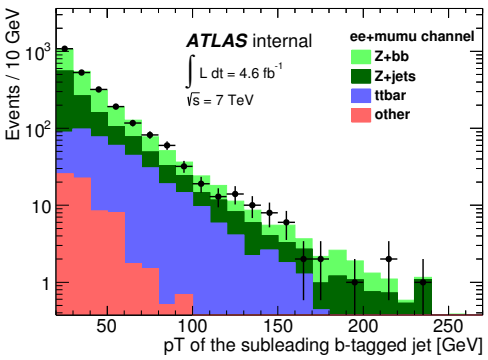

(d) Rapidity of the sub-leading b-tagged jet

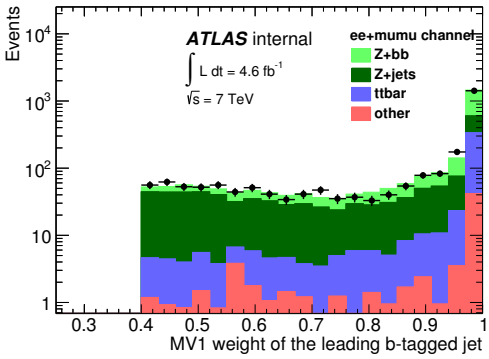

(e) MV1 weight of the leading b-tagged jet

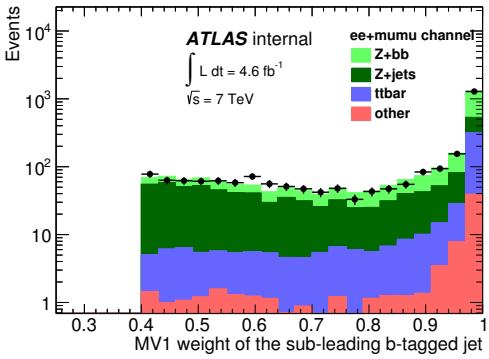

(f) MV1 weight of the sub-leading b-tagged jet

Figure 5.1: Data-MC comparison for the rapidity, p_{T} and MV1 weight of the leading and sub-leading b-tagged jet after $Z + b\bar{b}$ signal selection. The distribution for $Z + b\bar{b}$ is normalised according to the cross section measurement that was performed in this analysis. All other distributions are normalised according to the MC predictions.

6.520 is used for the parton shower and hadronisation and JIMMY 4.31 for the simulation of the underlying event. Matrix element and parton shower are matched by using the MLM ap-

Table 5.2: Number of data events after the specified analysis selection steps for the electron and the muon channel. Only statistical errors are included.

Selection step	Electron channel	Muon channel
Trigger	1438965 ± 1199	2243234 ± 1497
Exactly two leptons	1264405 ± 1124	1762748 ± 1327
Trigger matching	1264206 ± 1124	1762696 ± 1327
Invariant Z mass	1126553 ± 1061	1572237 ± 1253
$E_T^{\text{miss}} < 70\,\text{GeV}$	1123077 ± 1059	1567408 ± 1251
≥ 1 jet	257920 ± 507	354446 ± 595
≥ 1 b-tagged jets	20089 ± 141	27065 ± 164
≥ 2 jets	9010 ± 94	12177 ± 110
≥ 2 b-tagged jets	1033 ± 32	1461 ± 38
≥ 3 b-tagged jets	24 ± 4	44 ± 6

proach. The parameter set for HERWIG + JIMMY is the AUET2-CTEQL1 tune [89] which includes previous results from ATLAS as well as from the Tevatron and LEP experiments. However the $Z + b\bar{b}$ contribution is strongly suppressed and only results from gluon splitting in the parton shower in this sample and therefore a particular sample with the same specifications but containing only signal events is used in addition. To avoid double-counting signal events from the Z + jets sample, an overlap removal procedure is applied which will be described in Section 5.2.1. Both samples are generated with an invariant dileptonic mass cut $m_{ll} > 40\,\text{GeV}$ and include leading order matrix element calculations with up to five partons (three in addition to the two signal jets of the $Z + b\bar{b}$ sample).

The dominant background in this analysis is the dileptonic decay of $t\bar{t}$ events. For the simulation of those events MC@NLO 4.01 with the CT10 PDF set [64, 90] is used. Like the Z + jets sample the $t\bar{t}$ sample is also interfaced to HERWIG + JIMMY. For systematic studies an alternative $t\bar{t}$ sample produced with POWHEG and interfaced to PYTHIA is used.

Further backgrounds events are expected from single-top events and diboson production (WW, WZ and especially ZZ). The single-top contribution in the t-channel is simulated with AcerMC and PYTHIA is used for showering and underlying event modelling. The t-channel as well as the associated Wt production and the diboson sample use the same MC@NLO and HERWIG + JIMMY configuration as the nominal $t\bar{t}$ dataset.

In-time as well as out-of-time pile-up are included in all simulations by overlaying the hard processes and the underlying event with additional soft di-jet events, so-called minimum-bias events.

A more detailed summary of the used samples can be found in Appendix A.

5.2.1 Overlap removal between $Z + b\bar{b}$ and Z + jets

The final state with a lepton pair and a pair of bottom quarks is produced in the matrix element in dedicated ALPGEN $Z + b\bar{b}$ signal samples. However, this final state can also occur when a lepton pair is produced in association with a gluon in the matrix element where the gluon splits into a bottom quark pair in the parton showering as included in the ALPGEN Z + jets samples. As a consequence there is a possible overlap between the ALPGEN $Z + b\bar{b}$ and the ALPGEN Z+jets sample. It is therefore necessary to reject certain events that have identical heavy flavour final states but arise from different samples. The overlap removal (OR) procedure is based on the assumption that events with a small angle $\Delta R(b - b)$ between the two bottom quarks are better described by the collinear parton shower approach in terms of event kinematics. On the other hand, for large angles the description from the exact matrix element calculation achieves more correct predictions.

The angular separation distribution for bottom quark pairs with $p_{\mathrm{T}}(b) > 20\,\mathrm{GeV}$ for the $Z + b\bar{b}$ and the Z + jets datasets is shown in Figure 5.2a where the bottom quark pairs are classified as originating from gluon splitting or from the matrix element. This classification is based on the truth information in the Monte Carlo and is described in detail in [63]. The corresponding classification cut is at $\Delta R(b - b) = 0.4$, which means that

- events with $\Delta R(b - b) < 0.4$ are kept from the Z + jets sample and rejected in the $Z + b\bar{b}$ sample, whereas
- events with $\Delta R(b - b) > 0.4$ from the Z + jets sample are rejected and kept when they are from the $Z + b\bar{b}$ sample.

Figure 5.2b shows the angular separation after applying the overlap removal procedure and it can be seen that there is a smooth transition between the two regions at $\Delta R(b - b) = 0.4$.

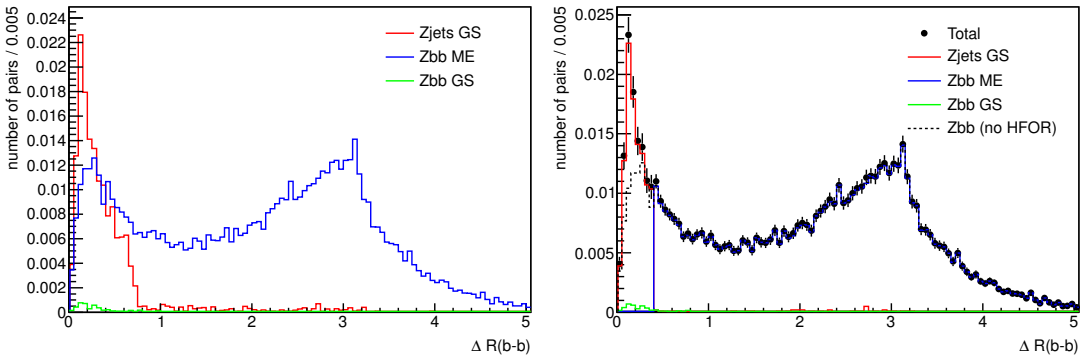

(a) before OR (b) after OR

Figure 5.2: Angular separation distribution $\Delta R(b - b)$ for gluon splitting (GS) events from ALPGEN Z + jets and $Z + b\bar{b}$ sample originating from the gluon splitting or the matrix element (ME) calculation [63].

5.2.2 Corrections applied to Monte Carlo simulation

Pileup reweighting

Usually the Monte Carlo production starts before or during the data taking and therefore before knowing the exact pileup conditions in the recorded data. The MC events are hence reweighted to be in accordance with the true pileup in data. This reweighting is based on the average number of pileup interactions $< \mu >$ which is proportional to the instantaneous luminosity and is determined per luminosity block. Figure 5.3. shows the distribution of $< \mu >$ for the different data taking periods. The average number of interactions in the electron channel and in the muon channel before and after the reweighting can be seen in Figure 5.4. After reweighting a better description of the high statistics bins is achieved.

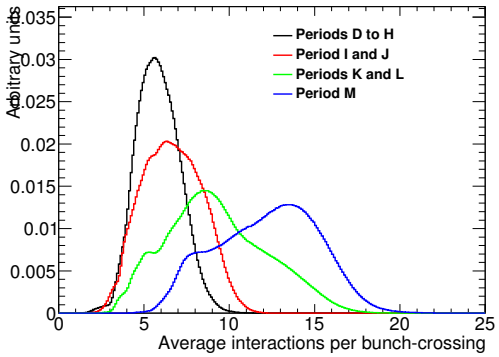

Figure 5.3: Average number of interactions $< \mu >$ grouped by data taking periods.

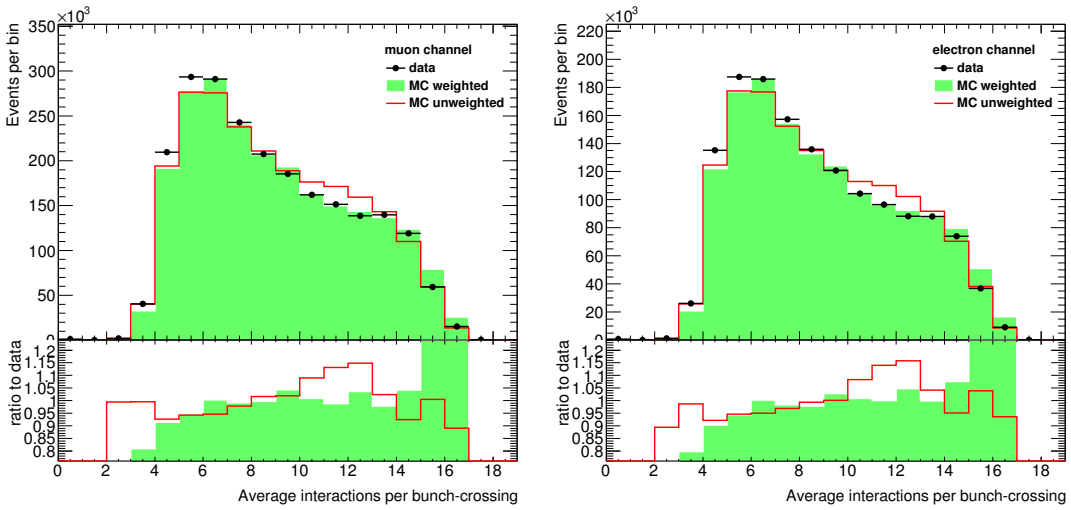

(a) $Z \rightarrow \mu\mu$ (b) $Z \rightarrow ee$

Figure 5.4: The average number of interactions before and after the pileup reweighting.

Reweighting of the z-vertex position

Comparisons between data and simulation has shown a significant mismodelling of the z-coordinate of the primary vertex. To correct for this effect, weights have been applied to MC. The weights were derived as documented in [91].

b-tagging reweighting

The performance of flavour tagging algorithms at ATLAS is usually described by two characteristic quantities for a given cut (the so-called operation point): the b-tagging efficiency and the mistag rates for light and charm jets. Several methods have been developed to measure the performance of the b-tagging algorithm (see Section 4.5). It is evaluated on data and is usually not modelled correctly in simulation. Therefore scale factors are applied to MC. These scale factors are defined as the ratio of the b-tag efficiency in data and simulation and are parametrised as a function of the jet kinematics. Similar scale factors are defined for the probability of wrongly tagging a jet originating from a charm quark (c-tag efficiency) or originating from a light parton (mistag rate). The scale factors for all selected jets in an event are multiplied to obtain the overall scale factor.

Trigger efficiency reweighting

The efficiencies of the triggers in data and Monte Carlo are not identical. However they have been measured on data using tag-and-probe methods: in selected $Z \to ll$ or $J/\Psi \to ll$ decays one lepton has been selected to identify the event (tag) and the other lepton is used to measure the efficiency (probe). Detailed descriptions can be found in [87] and [92] for the muon trigger and [86] for electron trigger. As a result of these efficiency measurements, scale factors with their corresponding uncertainties are provided by the ATLAS performance groups to compensate for the differences between data and MC.

Lepton reconstruction and identification efficiency reweighting

Similar to the trigger efficiencies, scale factors for the lepton reconstruction and identification efficiencies are estimated with tag-and-probe methods and provided by the performance groups. The electron reconstruction and identification efficiencies for data and MC are shown in Figure 5.5a. A similar plot for the muon reconstruction efficiency is shown in Figure 5.5b.

Lepton momentum smearing

Due to a better detector resolution modelling in MC compared to the resolution in data the reconstructed lepton momenta are smeared to describe the data. This procedure is described for electrons and for muons and the impact on the Z mass lineshape can be seen in Figure 5.6.

Jet momentum smearing

In order to account for a disagreement in the jet energy resolution a smearing to the jet energy has to be applied. The smearing factor is obtained by calculating the difference between the

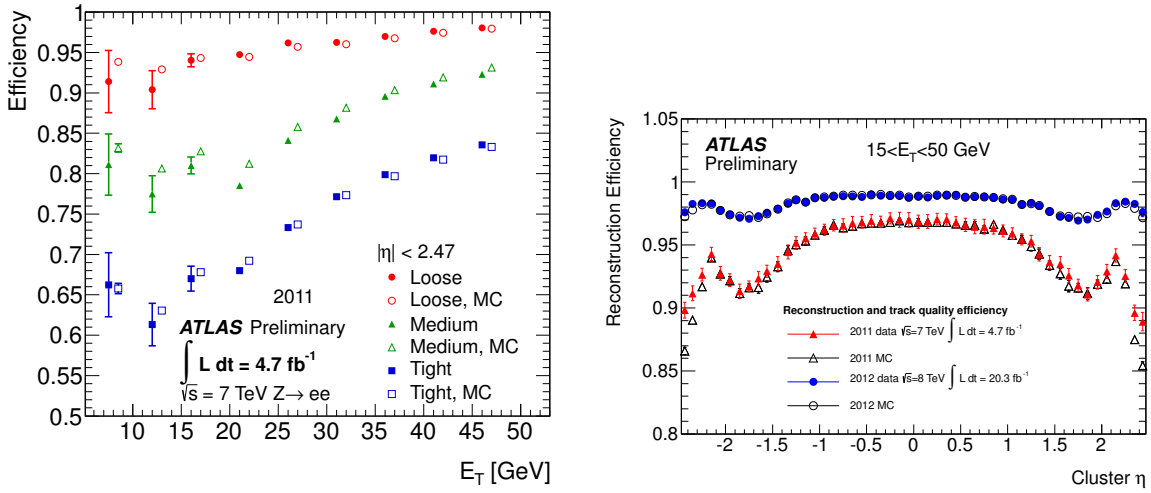

(a) Electron identification and reconstruction efficiency

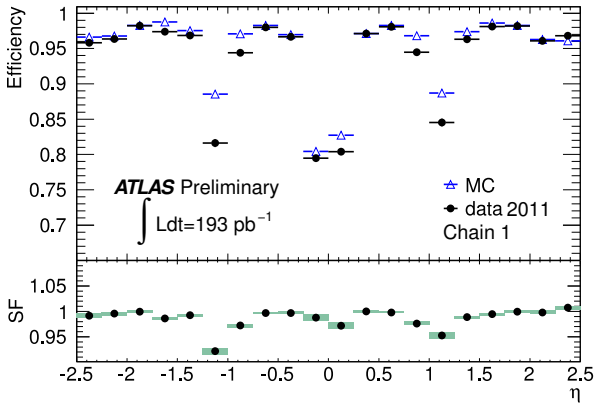

(b) Muon reconstruction efficiency

Figure 5.5: Lepton reconstruction efficiencies in data and MC. (a) Electron identification efficiency as a function of η and reconstruction efficiency as a function of E_{T} [93]. (b) Combined muon reconstruction efficiency for Chain 1 (Staco muons) as a function of the pseudorapidity [94].

squares of the unsmeared resolution of reconstructed jets in MC $\mathrm{res}_{\mathrm{MC}}$ and the total resolution in data $\mathrm{res}_{\mathrm{data}}$:

$$\text{smearing factor} = \sqrt{(\mathrm{res}_{\mathrm{data}})^2 - (\mathrm{res}_{\mathrm{MC}})^2} \tag{5.1}$$

The p_{T} of the jet is multiplied by a random factor obtained by a Gaussian function with mean of 1 and the variance being represented by the smearing factor.

5.2.3 Event selection on particle level

To correct for detector effects and for comparisons with theoretical predictions the measured cross sections are unfolded to particle level which is defined based on truth particle information from the MC generator. In order to reduce theoretical uncertainties due to extrapolations to a larger phase space, the particle level definition and the detector level definition of the signal

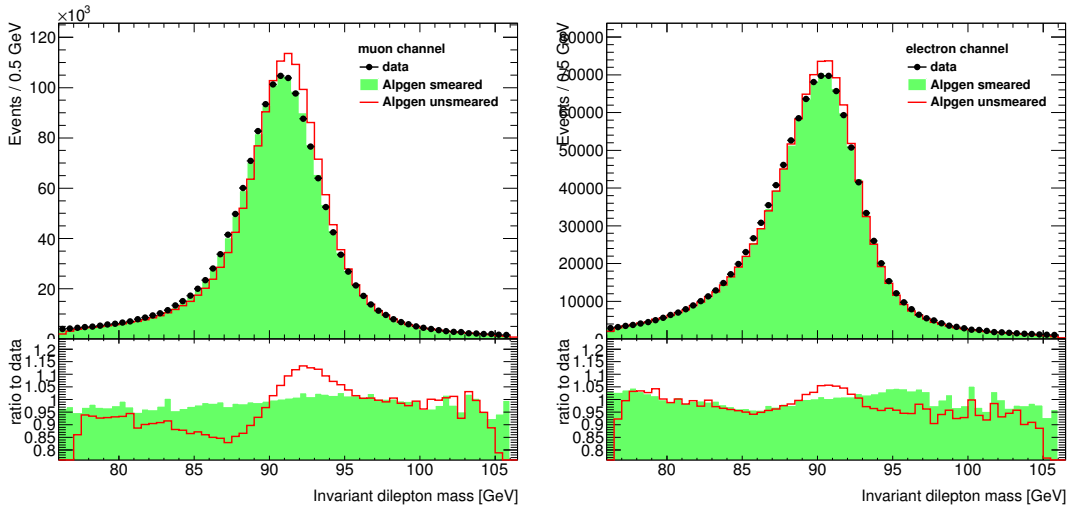

(a) $Z \to \mu\mu$ (b) $Z \to ee$

Figure 5.6: The invariant mass of the reconstructed Z boson in data as well as in MC before and after the lepton momentum smearing for (a) the $Z \to \mu\mu$ and (b) the $Z \to ee$ decay.

are chosen to be as close as possible. For this purpose a so-called lepton dressing is applied in which all photon four-vectors within $\Delta R < 0.1$ around stable muons or electrons are added to those. Since also the lepton direction can be changed during this process the initial four-vector is used for the ΔR matching. Dressed leptons are required to have $p_{\mathrm{T}} > 20\,\mathrm{GeV}$ and $|\eta| < 2.5$. An event is selected when there are two leptons of the same flavour but with opposite charge and an invariant dilepton mass $76\,\mathrm{GeV} < m_{ll} < 106\,\mathrm{GeV}$.

The jet definition is based on all other further particles including neutrinos, hadrons and low energetic muons. These are passed to the same anti-k_{T} jet algorithm with a distance parameter of $R = 0.4$ as used on detector level and identical kinematic selection of $p_{\mathrm{T}} > 20\,\mathrm{GeV}$ and $|\eta| < 2.5$ is required. Any so-called truthjet within $\Delta R < 0.5$ to a signal lepton is discarded.

Truthjets are matched to weakly decaying b-hadrons with $p_{\mathrm{T}} > 5\,\mathrm{GeV}$ and if they fulfil $\Delta R(\text{jet, hadron}) < 0.3$ they are labelled true b-jets. The list of b-hadrons includes the bottom mesons B^0, $B^{\pm}$, B_s^0, $B_c^{\pm}$ and the bottom baryons Λ_b^0, Σ_b^0, $\Sigma_b^{\pm}$, Ξ_b^0, $\Xi_b^{\pm}$, $\Omega_b^{\pm}$, Ξ_{bc}^0, $\Xi_{bc}^{\pm}$. If the jet is not a true b-jet and matched to a charm quark using the same matching criterion as above the jet is labelled as true c-jet. If a truthjet is neither a b-jet nor a c-jet it is labelled as a true light-jet which includes all other flavours and also jets from gluons and τ leptons.

The following MC reweightings are also applied on particle level:

- The pileup reweighting as described in Section 5.2.2 and the
- z-vertex reweighting as described in Section 5.2.2.

CHAPTER 6

Measurement of the $Z + b\bar{b}$ cross section

The measurement of inclusive production cross sections σ for physics processes can be performed by determining the total number of signal events within a dataset and follows the formula:

$$\sigma = \frac{N_{\text{data}} - N_{\text{background}}}{\mathcal{U} \cdot \mathcal{L}} = \frac{N_{\text{signal}}}{\mathcal{U} \cdot \mathcal{L}} \tag{6.1}$$

The number of signal events N_{signal} is the number of data events passing the selection N_{data} minus the number of background events $N_{\text{background}}$ and $\mathcal{L}$ is the integrated luminosity of the dataset. The correction factor $\mathcal{U}$ is derived from Monte Carlo simulation and represents the event selection efficiency to transform the measured cross section from detector level to particle level which makes the measurement independent of the specific detector properties and hence allows a better comparison of the results with other measurements and theory predictions.

This chapter describes the measurement of the inclusive event cross section of a Z-boson which is produced in association with two b-quarks. The measurement is performed independently for the Z boson decaying into two electrons or two muons and for the combination of both channels. The selected data events still contain a large fraction of light jets mistakenly identified as b-jets. The number of data events N_{data} is therefore estimated from a fraction fit using additional information from the shape of a distribution related to b-tagging which is described in Section 6.2. The number of background events $N_{\text{background}}$ is estimated from data or MC simulation depending on the background process and the procedure is described in Section 6.1. The transformation to particle level is factorised into two components: the efficiency of the double b-tagging ϵ_{bb} and all the other efficiencies are contained in one correction factor C. It hence follows $\mathcal{U} = C \cdot \epsilon_{bb}$ (see Section 6.3).

A description of the systematic uncertainties is presented in the next chapter and the results will be summarised in Chapter 8.

6.1 Background estimation

After the $Z + b\bar{b}$ event selection the data contains backgrounds from misidentified leptons or misidentified b-jets. By far the largest contribution is from events where one or both jets are light or charm jets and falsely identified as b-jets. The distinction between those events and the ensemble of signal events is performed on a statistical level in a fit procedure which is described in Section 6.2. The remaining backgrounds are estimated from Monte Carlo simulations (see Section 6.1.1) except for the multijet contribution which is estimated with a data-driven method as described in Section 6.1.2.

6.1.1 Background estimation from simulation

Top pair events

The process whichc dominates the irreducible background is $t\bar{t}$ production, where both W bosons decay to leptons, which contributes about 15 % of all background events. The size of this contribution is estimated from the MC@NLO Monte Carlo sample where the normalisation is obtained from the theoretically predicted cross section scaled to the data luminosity. It is already largely suppressed by the invariant dileptonic mass cut. To further reduce the contamination from $t\bar{t}$ events the veto on the missing transverse energy $E_T^{\text{miss}} < 70\,\text{GeV}$ is applied. Figure 6.1 shows the E_T^{miss} distribution of the selected signal and of top pair events in the electron and the muon channel without the E_T^{miss} cut being applied. The cutflow for the $t\bar{t}$ sample, the rejection efficiencies and the corresponding signal losses are listed in Table 6.1.

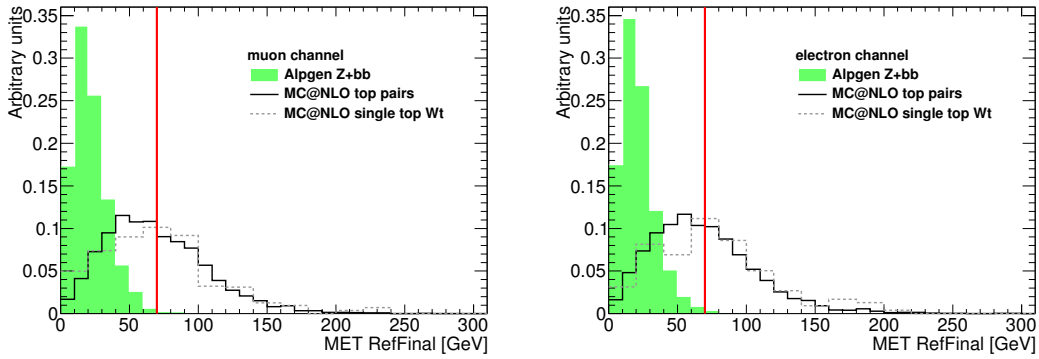

(a) $Z \to \mu\mu$ (b) $Z \to ee$

Figure 6.1: E_T^{miss} distributions after signal selection but without applying the E_T^{miss} cut for $Z + b\bar{b}$ events, top pair and single-top background in the electron and muon channel. The distributions are normalised to area one. The red line indicates the selection cut at $E_T^{\text{miss}} < 70\,\text{GeV}$.

Table 6.1: Number of top pair events after the specified analysis selection steps for the electron and the muon channel. The errors quoted only include the statistical uncertainties. For each channel the last two columns show the $t\bar{t}$ rejection efficiency and the relative loss of signal events for the corresponding selection with respect to selection step before.

	Electron channel			Muon channel		
Selection step	Events	Rej. eff.	Sig. loss	Events	Rej. eff.	Sig. loss
Trigger	7894 ± 88			19332 ± 139		
Exactly two leptons	4057 ± 63	48.6%	38.9%	5148 ± 71	73.4%	36.2%
Trigger matching	4054 ± 63	0.1%	0.0%	5140 ± 71	0.2%	0.0%
Invariant Z mass	866 ± 29	78.6%	8.1%	1131 ± 33	78.0%	7.9%
$E_T^{\text{miss}} < 70\,\text{GeV}$	475 ± 21	45.1%	0.6%	612 ± 24	45.9%	0.6%
≥ 1 jet	466 ± 21	1.9%	47.0%	601 ± 24	1.8%	47.7%
≥ 1 b-tagged jets	395 ± 19	15.3%	48.3%	516 ± 22	14.1%	48.7%
≥ 2 jets	344 ± 18	12.9%	48.3%	447 ± 21	13.3%	49.0%
≥ 2 b-tagged jets	172 ± 13	50.1%	78.6%	224 ± 14	49.8%	78.8%

Single top events

Smaller contributions are expected from single top production (less than 0.5 %) and here predominantly in the Wt channel where both W bosons decay leptonically. The E_T^{miss} distribution for this process is also plotted in Figure 6.1. A summary of the event selection for the three single-top channels is given in Table 6.2. As can be sen from the table, The s- and the t-channel contributions with a leptonically decaying W boson are negligible in this analysis.

Diboson events

The dibosonic background is summarised in Table 6.3. It contributes to about 2.5 % of all selected events. The dominant contribution is the ZZ production with one Z decaying leptonically and the other Z decaying hadronically into b-quark pairs or other mistagged quark pairs. The WZ background with a leptonically decaying Z boson and the W boson decaying into a quark pair has the same signature except that the decay to a b-quark is strongly suppressed by the CKM matrix (see e.g. [95] or [96]). This background is inspected separately for W^- and W^+ decays since the latter has a larger cross section at proton-proton colliders due to an enhanced PDF contribution of up-quarks.

Background from other electroweak processes like W boson production and $Z \to \tau\tau$ decays both with additional (heavy flavour) jets were found to give negligible contribution in the signal phase space.

Table 6.2: Number of single-top events after the specified analysis selection steps for the electron and the muon channel. The given errors only include the statistical uncertainties.

	Electron channel			Muon channel		
Selection step	Wt	s-chan.	t-chan.	Wt	s-chan.	t-chan.
Trigger	707 ± 26	6.5 ± 2.5	14 ± 3	1448 ± 38	87 ± 9	956 ± 30
Exactly two leptons	379 ± 19	0.9 ± 1.0	2.3 ± 1.5	469 ± 21	0.7 ± 0.8	10 ± 3
Invariant Z mass	81 ± 9	0.1 ± 0.4	0.4 ± 0.6	100 ± 10	0.1 ± 0.3	2.3 ± 1.5
$E_T^{\text{miss}} < 70\,\text{GeV}$	48 ± 6	0.1 ± 0.4	0.3 ± 0.5	60 ± 7	0.1 ± 0.3	2.1 ± 1.4
≥ 1 jet	44 ± 6	0.1 ± 0.3	0.2 ± 0.5	55 ± 7	0.1 ± 0.3	1.2 ± 1.1
≥ 1 b-tagged jets	30 ± 5	0.0 ± 0.1	0.0 ± 0.1	38 ± 6	0.0 ± 0.2	0.7 ± 0.8
≥ 2 jets	14 ± 3	0.0 ± 0.1	−0.0 ± 0.2	18 ± 4	0.0 ± 0.1	0.5 ± 0.7
≥ 2 b-tagged jets	3.8 ± 1.9	0.0 ± 0.0	−0.0 ± 0.2	4.6 ± 2.1	0.0 ± 0.1	0.1 ± 0.4

Table 6.3: Number of dibosonic events after the specified analysis selection steps for the electron and the muon channel. The given errors only include the statistical uncertainties.

	Electron channel			Muon channel		
Selection step	ZZ	W^+Z	W^-Z	ZZ	W^+Z	W^-Z
Trigger	700 ± 26	694 ± 26	366 ± 19	956 ± 30	891 ± 29	492 ± 22
Exactly two leptons	437 ± 20	448 ± 21	230 ± 15	615 ± 24	570 ± 23	312 ± 17
Invariant Z mass	425 ± 20	437 ± 20	224 ± 14	602 ± 24	558 ± 23	306 ± 17
$E_T^{\text{miss}} < 70\,\text{GeV}$	419 ± 20	431 ± 20	222 ± 14	597 ± 24	552 ± 23	303 ± 17
≥ 1 jet	385 ± 19	373 ± 19	201 ± 14	545 ± 23	478 ± 21	274 ± 16
≥ 1 b-tagged jets	100 ± 10	52 ± 7	28 ± 5	152 ± 12	58 ± 7	38 ± 6
≥ 2 jets	70 ± 8	42 ± 6	23 ± 4	103 ± 10	45 ± 6	31 ± 5
≥ 2 b-tagged jets	22 ± 4	1.4 ± 1.2	1.2 ± 1.1	32 ± 5	1.9 ± 1.4	1.7 ± 1.3

6.1.2 Multijet background estimation from data

Even though the probability of jets faking two isolated quality leptons (or producing them in semileptonic decays) and two additional falsely b-tagged jets is very low the multijet cross section is about seven orders of magnitude larger than the signal [97] and hence the contribution from multijet events has to be estimated. This has been performed using two different methods which are described in the following section. They are necessarily applied on data because the low statistics in multijet Monte Carlo simulations would result in unacceptably large uncertain-

ties. Another reason is a possible mismodelling of the misidentification rate of leptons caused by jets. Both methods are based on the assumption that the invariant dilepton mass shape is invariant throughout the event selection.

Method 1: fitting the multijet contribution in a control region

With this method [63] the lineshape of the invariant dileptonic mass is used to estimate the multijet contribution. This method was initially used for the measurement of the $Z + 1b$ cross section and has been adapted to $Z + b\bar{b}$ measurement. The shape is defined by the following formula containing a multijet and a non-multijet contribution with the normalisations N_{multijet} and $N_{\overline{\text{multijet}}}$:

$$M(m_{ll}, N_{\overline{\text{multijet}}}, N_{\text{multijet}}, \alpha) = N_{\overline{\text{multijet}}} \cdot f(m_{ll}) + N_{\text{multijet}} \cdot g(m_{ll}, \alpha) \tag{6.2}$$

The shape of the signal and non-multijet contribution $f(m_{ll})$ is estimated from simulation. The shape of the multijet contribution $g(m_{ll}, \alpha)$ is parametrised by an exponential decay function with the decay parameter α. This hypothesis is verified in several control regions. The fit parameter α is obtained by fitting the Z lineshape in a control region with enriched multijet content which is disjoint to the baseline signal event selection. It is defined by inverting a specific lepton selection criterion to select leptons that are likely to be faked by jets. In the muon channel both muons are required to be anti-isolated i.e. $\sum p_{\text{T}}(\text{track})/p_{\text{T}}(\text{muon}) > 0.1$ and the impact parameter cut on the muons is not needed to be fulfilled. In the electron channel one of the two selected electrons does not meet the conditions of the medium quality flag. As a consequence the di-electron trigger is changed to the single-electron trigger EF_e20_medium. However, this trigger has become prescaled in period K and hence only a reduced dataset of $1.7\,\text{fb}^{-1}$ is available in this control region. In addition in both channels the invariant dilepton mass range is extended to $70\,\text{GeV} < m_{ll} < 120\,\text{GeV}$. It has been tested that α is stable in control regions with varied triggers, lepton selections and invariant mass ranges. Figure 6.2 shows the control region results of the fitted slope parameter α after Z, Z+1 jet and $Z + 1b$ selection for the electron and the muon channel. The slope parameter α is found to be -0.020 ± 0.001 in the electron channel and -0.036 ± 0.001 in the muon channel control region.

Finally, a fraction fit is performed according to Formula 6.2 in the $Z + b\bar{b}$ signal region with a wider invariant mass region ranging from $50\,\text{GeV} < m_{ll} < 200\,\text{GeV}$ (see Figure 6.3) which is being projected into the standard invariant mass range afterwards. The number of multijet events is found to be compatible with zero as summarised in Table 6.4. The multijet contribution is therefore treated as negligible in the following analysis and the uncertainty from this hypothesis will be treated in Section 7.4.1.

Method 2: "ABCD-method"

As a cross-check a second multijet estimation has been performed which is described in more detail in Ref. [98]. It should be noted that this estimation has been performed at a different missing transverse energy selection requiring $E_T^{\text{miss}} < 30\,\text{GeV}$. However, it is assumed that the multijet contribution is independent of E_T^{miss} and therefore the conclusions are applicable here as well.

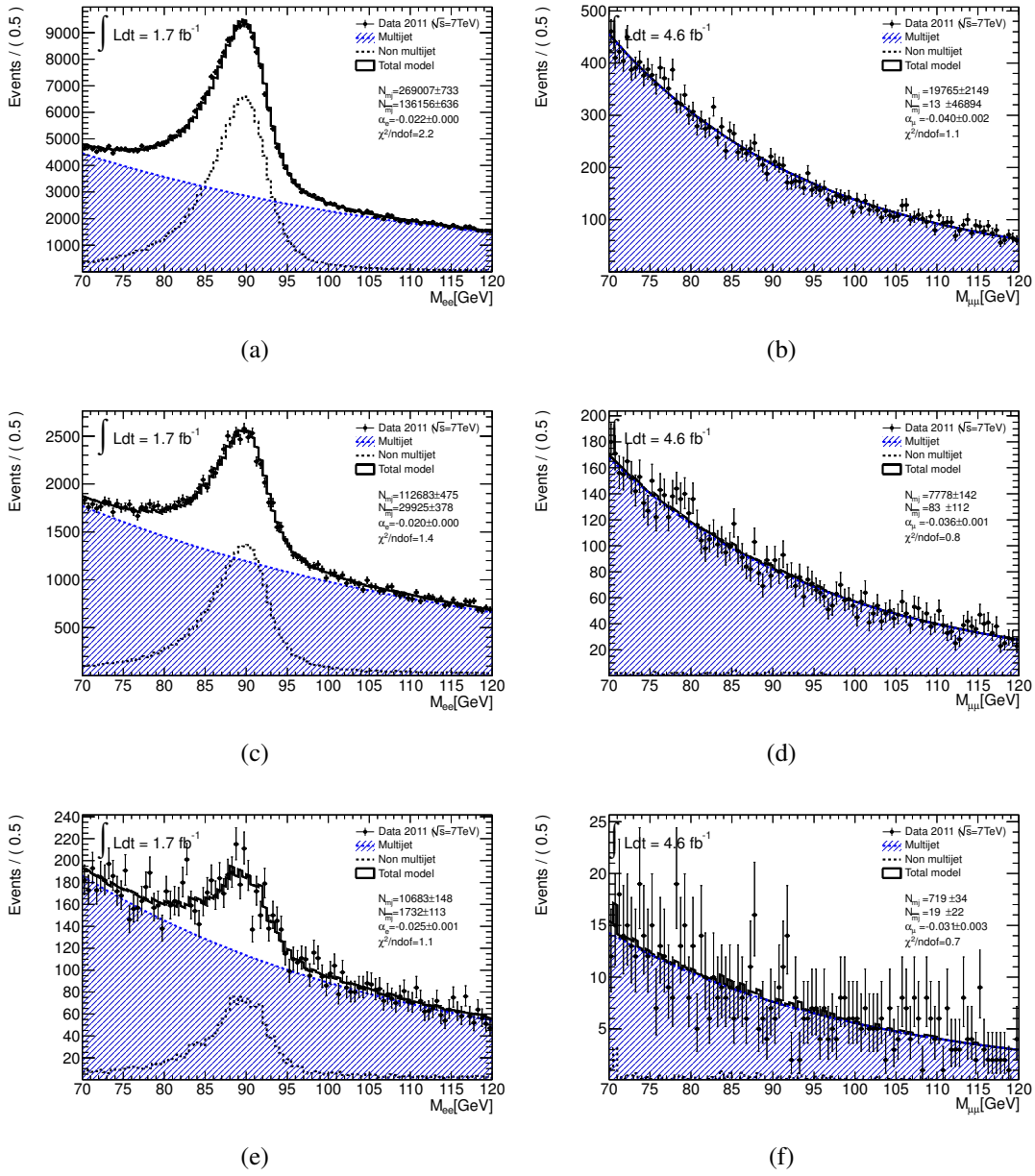

Figure 6.2: Invariant dilepton mass distribution for the non-multijet background and the fitted multijet background shape for the muon channel (left) and the electron channel (right). The control plots are shown after Z selection (a,b), after Z+1 jet selection (c,d) and after $Z + 1b$ selection (e,f). [63]

First of all the two uncorrelated selection cuts J and L are defined that split the selected dilepton events into four disjoint regions[1]:

$$\mathrm{JL}, \bar{\mathrm{J}}\mathrm{L}, \mathrm{J}\bar{\mathrm{L}}, \bar{\mathrm{J}}\bar{\mathrm{L}}$$

[1] The four regions are often labelled as A, B, C and D. Therefore this method is also known as ABCD-method

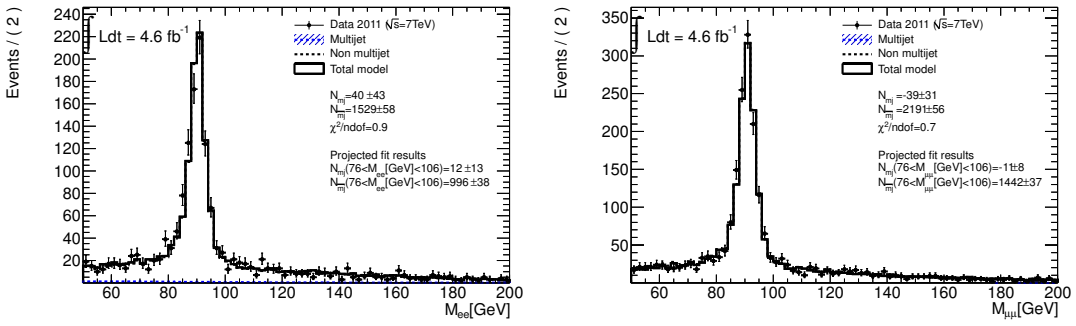

(a) (b)

Figure 6.3: Fit results of the multijet and non-multijet components in the extended invariant mass range between 50 and 200 GeV. [63]

Table 6.4: Multijet estimation results for the electron and the muon channel. The multijet slope parameter α is obtained by fitting the invariant mass distribution in a control region with enhanced multijet content. The resulting multijet contributions N_{multijet} are compatible with zero.

		Electron channel	Muon channel
	α	-0.036 ± 0.001	-0.020 ± 0.001
wide mass range	N_{multijet}	40.0 ± 43.0	-39.2 ± 31.0
	$N_{\overline{\text{multijet}}}$	1529 ± 57.8	2191.2 ± 56.5
signal mass range	N_{multijet}	11.8 ± 12.7	-10.7 ± 8.4
	$N_{\overline{\text{multijet}}}$	995.6 ± 37.6	1442.5 ± 37.2

The selection cut J is passed when at least two b-tagged jets are selected in addition to the Z boson. Otherwise is is labelled as $\bar{\text{J}}$. The second selection is different for the electron channel and for the muon channel and similar to the ones used in multijet Method A in the previous section. In the electron channel L is fulfilled when both leptons have opposite charge and otherwise it is labelled $\overline{\text{L}}$. In the muon channel the requirement is defined by the muon isolation. Thus JL corresponds to the signal-like region.

Furthermore two invariant mass sideband regions L and R surrounding the default Z peak region are defined by 51 GeV $< m_{ll} <$ 76 GeV and 76 GeV $< m_{ll} <$ 106 GeV. They are used to calculate the normalisation in the two regions before jet selection $\bar{\text{J}}\text{L}$ and $\overline{\text{JL}}$. The Monte Carlo distribution is normalised to fit the data within the Z peak region. The difference between data and simulation in the sideband region is then considered to be multijet background and is projected into the Z peak region. The sidebands in region $\text{J}\overline{\text{L}}$ are scaled by the corresponding scale factors obtained from region $\overline{\text{JL}}$ and the multijet contribution is obtained in the same way as for the other regions.

Finally, the number of multijet events in the signal region N_{JL} can be estimated from the

number of multijet events of the other three regions ($N_{\bar{\text{J}}\text{L}}$, $N_{\text{J}\bar{\text{L}}}$, $N_{\bar{\text{J}}\bar{\text{L}}}$) by the following relation:

$$\frac{N_{\text{JL}}}{N_{\bar{\text{J}}\text{L}}} = \frac{N_{\text{J}\bar{\text{L}}}}{N_{\bar{\text{J}}\bar{\text{L}}}} \tag{6.3}$$

This relation is valid because the selection cuts J and L are uncorrelated.

Table 6.5: Estimated number of multijet events in the four disjoint event selection regions in the complete invariant mass range (i.e. Z mass range and both sidebands) and in the projected Z mass range.

	51 GeV $< m_{ll} <$ 131 GeV		76 GeV $< m_{ll} <$ 106 GeV	
	Electron ch.	Muon ch.	Electron ch.	Muon ch.
signal region N_{JL}	29.8 ± 16.0	16.2 ± 4.5	17.9 ± 9.6	9.7 ± 2.7
control region $N_{\bar{\text{J}}\text{L}}$	5097 ± 348	5977 ± 433	3058 ± 209	3586 ± 260
control region $N_{\text{J}\bar{\text{L}}}$	5.0 ± 2.6	14.6 ± 3.8	3.0 ± 1.6	8.8 ± 2.3
control region $N_{\bar{\text{J}}\bar{\text{L}}}$	857.4 ± 45.2	5399 ± 74	514.4 ± 27.1	3239 ± 44

With this method the exponentially decreasing shape of the multijet background has not been taken into account. Therefore a systematic has been assigned to the result where only the left (right) sideband has been used provide an up (down) variation. The final result for the electron channel is

$$N^{ee}_{multi\,jet} = 17.9 \pm 9.6\ \text{(stat.)} \pm 11.1\ \text{(syst.)}\ \text{events},$$

and for the muon channel

$$N^{\mu\mu}_{multi\,jet} = 9.7 \pm 2.7\ \text{(stat.)} \pm 7.5\ \text{(syst.)}\ \text{events}.$$

In both channels the multijet contribution is compatible with zero and hence these results are confirming the results from Method A.

6.2 Determination of the heavy flavour content

With the knowledge of the level of the contributing background processes in the selected phase space the number of signal events can be easily calculated. However, the selected events are still a mixture of true $Z + b\bar{b}$ events and those where at least one of the jets is misidentified as a b-jet. The contribution from this irreducible background is determined on a statistical basis by performing a maximum likelihood template fit to data based on a flavour discriminating distribution.

6.2.1 Description of the fit procedure

Maximum likelihood fit

A *Maximum Likelihood Fit* is a statistical technique to estimate one or several parameters in a data ensemble. Let p be an unknown parameter that is derived from the measurement of an arbitrary random variable x and let x be distributed by a known probability density function $F(p, x)$. Then the likelihood function $L(p)$ is defined as

$$L(p) = \prod_{i=1}^{N} F(p, x_i) \tag{6.4}$$

for a sample of N independent observations of x with values x_i. In order to find the best value for p this parameter is varied such that the likelihood L is maximised. For convenience reasons one usually considers the negative logarithm of L which is minimised:

$$-\log L(p) = -\sum_{i=1}^{N} \log F(p, x_i) \tag{6.5}$$

By construction the total normalisation is identical to the number of measurements and is thus independent of the parameter values. Equation 6.4 is modified by multiplying a Poissonian distribution with mean ν describing the probability of observing a sample of size N. ν is now also a random variable and can depend on the parameter p. The so-called *Extended Maximum Likelihood Fit* function is:

$$L(p) = \frac{\nu^n}{n!} e^{-\nu} \cdot \prod_{i=1}^{N} F(p, x_i) \tag{6.6}$$

By redefinition of $L(p)$ due to omitting constant terms that are irrelevant for the minimisation, Equation 6.5 becomes:

$$-\log L(p) = -n \ \log(\nu(p)) + \nu(p) - \sum_{i=1}^{N} \log F(p, x_i) \tag{6.7}$$

Analysis fit model

In this analysis at least two additional b-tagged jets are selected. In order to discriminate the final state with two true b-jets from those where at least one of the jets is a mistagged light or charm jet a fit is performed on a flavour sensitive variable that is described in the next section. In the MC model, each of the two jets is classified as a true b-, c- or light-jet according to the algorithm that is described on page 47 in Section 5.2.3 for the classification of truth jets. As a consequence there are six different classifications for the flavour composition two b-tagged jets:

- **bb:** both b-tagged jets are matched to b-hadrons. This is the signal case.

- **bc:** only one of the two leading tagged jets is matched to a b-hadron, the other is matched to a charm quark.
- **bl:** only one of the two leading tagged jets is matched to a b-hadron, the other jet is not matched.
- **cc:** both jets are matched to charm quark.
- **cl:** one jet is matched to a charm quark, the other jet is not matched.
- **ll:** Both jets are neither matched to a b-hadron nor to a charm quark.

In this classification it is not distinguished whether a jet is the leading or the subleading jet and hence e.g. $bc = cb$. In approximately 2 - 3 % of the cases more than two b-tagged jets occur and here only the two leading tagged jets are used for the classification. Jets can also be produced from τ leptons. However, the contribution from such jets faking a b-tagged jet is found to be negligible and is therefore not treated separately in the fit.

The combined equation for the fit variable p and the data distribution D is given by

$$\begin{aligned} D(p) &= N_Z \cdot \Big[f_{bb}\,\mathcal{T}_{bb}(p) + f_{bc}\,\mathcal{T}_{bc}(p) + f_{bl}\,\mathcal{T}_{bl}(p) \\ &\quad + f_{cc}\,\mathcal{T}_{cc}(p) + f_{cl}\,\mathcal{T}_{cl}(p) + f_{ll}\,\mathcal{T}_{ll}(p)\Big] \\ &\quad + N_{t\bar{t}}\,\mathcal{T}_{t\bar{t}}(p) + N_{1\mathrm{t}}\,\mathcal{T}_{1\mathrm{t}}(p) + N_{\mathrm{dib}}\,\mathcal{T}_{\mathrm{dib}}(p) \end{aligned} \tag{6.8}$$

with the constraint

$$f_{bb} + f_{bc} + f_{bl} + f_{cc} + f_{cl} + f_{ll} = 1 \tag{6.9}$$

Here f_{xy} are the relative fractions of obtaining one of the six different flavour compositions, N_Z is the total number of Z events. $\mathcal{T}_{xy}(p)$ are the corresponding template distributions. Equivalently, $N_{t\bar{t}}$, $N_{1\mathrm{t}}$ and N_{dib} are the normalisations of the $t\bar{t}$, the single-top and the diboson backgrounds which are taken directly from the theoretically predicted cross sections. $\mathcal{T}_{t\bar{t}}(p)$, $\mathcal{T}_{1\mathrm{t}}(p)$ and $\mathcal{T}_{\mathrm{dib}}(p)$ are the corresponding template distributions and obtained from MC simulation. All given template distributions are by definition normalised to unity.

By modifying Equation 6.8 accordingly one obtains the logarithmic likelihood function:

$$\begin{aligned} -\log L(p) &= -N_Z\ \log(\nu_Z) + \nu_Z(p) - \sum_{i=1}^{N_Z} \log \mathcal{T}_Z(p_i) \\ &\quad - \sum_{i=1}^{N_{\mathrm{fixed}}} \log \mathcal{T}_{\mathrm{fixed}}(p_i) \end{aligned} \tag{6.10}$$

$$\text{with} \qquad N_Z = N - N_{\mathrm{fixed}} \tag{6.11}$$

$$\text{and} \qquad N_{\mathrm{fixed}} = N_{t\bar{t}} + N_{1\mathrm{t}} + N_{\mathrm{dib}} \tag{6.12}$$

and the composite probability density function for the part that is floating in the fit:

$$\begin{aligned} \mathcal{T}_Z(p) &= f_{bb}\,\mathcal{T}_{bb}(p) + f_{bc}\,\mathcal{T}_{bc}(p) + f_{bl}\,\mathcal{T}_{bl}(p) \\ &\quad + f_{cc}\,\mathcal{T}_{cc}(p) + f_{cl}\,\mathcal{T}_{cl}(p) + f_{ll}\,\mathcal{T}_{ll}(p) \end{aligned} \tag{6.13}$$

and for the part that is fixed in the fit:

$$\mathcal{T}_{\text{fixed}}(p) = \frac{N_{t\bar{t}}\,\mathcal{T}_{t\bar{t}}(p) + N_{1\text{t}}\,\mathcal{T}_{1\text{t}}(p) + N_{\text{dib}}\,\mathcal{T}_{\text{dib}}(p)}{N_{t\bar{t}} + N_{1\text{t}} + N_{\text{dib}}} \tag{6.14}$$

The software package RooFit [99] which is included in Root [62] has been used to construct the model and to perform the binned maximum likelihood fit. For the minimisation the MINUIT package [100] with the MIGRAD algorithm is used. The starting values for all parameters are set to the predicted values obtained by MC.

There are usually two ways implemented in MIGRAD to calculate statistical uncertainties on the fit parameter:

- The HESSE algorithm performs an inversion of the second derivative matrix evaluated at the minimum of the fitting function. This approach is only valid when the fitting function is in good approximation described by a parabola which corresponds to the logarithm of a Gaussian function.

- If this is not fulfilled the MINOS algorithm which evaluates real shape of the fitting function near the minimum can be used. This is achieved by a stepwise variation of each parameter during the minimisation of all other parameters. The resulting uncertainties are usually asymmetric while the spread between the two variations is a measure for the non-linearity of the fitting function.

It has been found that the difference between the two uncertainty estimations is of the order of 1 %. It has also been validated that the HESSE result is identical to the average of both variations from the MINOS result. Therefore the parabolic approximation around the minimum point is assumed to be valid and in the following only symmetrical uncertainties on the fit parameters will be given.

The Monte Carlo prediction for the six templates are summarised in Table 6.6 for the electron channel and the muon channel. It can be seen that the predicted number of events in the signal template is dominating and even larger than the sum of events in all non-signal templates.

Table 6.6: Predicted number of events per template in the electron channel and the muon channel for the Alpgen $Z + b\bar{b}$ and Z + jets samples.

Electron ch.	$\mathcal{T}_{bb}$	$\mathcal{T}_{bc}$	$\mathcal{T}_{bl}$	$\mathcal{T}_{cc}$	$\mathcal{T}_{cl}$	$\mathcal{T}_{ll}$
Z+jets	17.1 ± 2.5	8.3 ± 1.3	15.7 ± 2.1	81.7 ± 3.8	56.9 ± 3.7	91.0 ± 7.3
Z+bb	396.2 ± 6.0	26.2 ± 1.6	47.3 ± 2.2	1.5 ± 0.4	1.2 ± 0.3	3.1 ± 0.7
Sum	413.3 ± 6.4	34.5 ± 2.0	62.9 ± 3.1	83.2 ± 3.8	58.1 ± 3.7	94.2 ± 7.3
Muon ch.	$\mathcal{T}_{bb}$	$\mathcal{T}_{bc}$	$\mathcal{T}_{bl}$	$\mathcal{T}_{cc}$	$\mathcal{T}_{cl}$	$\mathcal{T}_{ll}$
Z+jets	15.5 ± 2.4	11.0 ± 1.6	16.2 ± 1.7	105.1 ± 4.0	78.5 ± 4.3	137.7 ± 9.4
Z+bb	526.0 ± 6.8	30.7 ± 1.6	68.0 ± 2.7	3.2 ± 0.6	1.0 ± 0.3	2.5 ± 0.6
Sum	541.6 ± 7.3	41.7 ± 2.3	84.2 ± 3.2	108.3 ± 4.1	79.5 ± 4.3	140.3 ± 9.4

Given the low number of events and the resulting fluctuations due to lower statistics in the non-bb templates a merging of several templates is inevitable. Different combinations will be studied in the following section.

6.2.2 Template construction

A crucial requirement for the construction of the fit templates is a good separation power between the templates, in particular between the signal template and the ones representing the non-bb contributions. Ideally, one would perform a two-dimensional fit with a flavour discriminating variable for each jet in each dimension. However, the signal yield does not allow a two-dimensional treatment of the problem and therefore one single quantity that combines the flavour information of both jets has to be used. The simplest approach is to use the sum of both individual variables. The disadvantage of this approach is that the relation between the two jets is not taken into account, e.g. two jets with a medium flavour weight have a similar value as one b-jet plus one light jet.

The most obvious flavour discriminating variable would be the MV1 weight. However, this variable is not suitable for two reasons: first, this variable is used already to tag the b-jets which has the consequence that the light flavour part is not represented, and secondly, the distribution for signal events has a narrow peak towards one which would require a retransformation beforehand.

Instead, several similar variables which have been described in detail in Section 4.5 are probed:

- The combination $\ln(P_b/P_l)$ of the probabilities P_b and P_l that correspond to the probability of a given jet being a b-jet and bein a light jet respectively.
- A similar combination using P_b and P_c is $\ln(P_b/P_c)$ where P_c represents the probability of a given jet to be a c-jet.
- The **SV0 mass** is the invariant mass of charged particles associated to the secondary vertex reconstructed by the SV0 b-tagging algorithm. In case there is no secondary vertex found this variable receives a value of -1.
- A similar variable is the **JetFitter mass**: the invariant mass of all charged-particle tracks attached to the JetFitter decay chain.

Since all these variables are either input or output variables of b-tagging algorithms there is a strong correlation among them and in particular with the MV1 weight used for the identification of b-jets. The template distributions are shown in Figure 6.4 for the electron channel and in Figure 6.5 for the muon channel. The plots on the left side show the template shapes of the six truth flavour cases that can occur. As expected, it can be observed that the separation is better between signal and the light-light template using $\ln(P_b/P_l)$ and between signal and the charm-charm template when $\ln(P_b/P_c)$ is used. Both the invariant masses obtained from the JetFitter and the SV0 tagger show larger overlap between the templates and therefore worse discrimination power. Moreover, the SV0 mass peaks at -2 which corresponds to the constellation where no secondary vertex was reconstructed to either of the two tagged jets. It has

been observed that this implies a strong and unrealisable constraint on the fit and hence large uncertainties on the fit are the consequence. Furthermore, the secondary vertex reconstruction efficiency is not a priori modelled correctly in simulation. It has been observed that by using the SV0 mass as well as the JetFitter mass as a fit variable a larger uncertainty on N_{bb} was the result. Due to the given reasons these variables are not considered optimal and therefore only $\ln(P_b/P_c)$ and $\ln(P_b/P_l)$ are used. A similar ATLAS analysis performing a measurement on the $Z + 1b$ cross section observed more stable fit behaviour when using $\ln(P_b/P_c)$. For consistency reasons $\ln(P_b/P_c)$ has been chosen as a baseline for the measurement in this thesis though all results were also cross-checked by using $\ln(P_b/P_l)$ as fit variable.

The plots on the right hand side show in addition to the signal templates the templates for the top and the dibosonic background. The template shapes are almost indistinguishable from the signal template shape and hence the contribution from these backgrounds is estimated from simulation. The normalisation factors $N_{t\bar{t}}$, N_{1t} and $N_{diboson}$ are fixed in the fit.

Fitting the data distribution with any of these four variables results in a very unstable and error-prone behaviour. As mentioned before, the fit is dominated by large statistical uncertainties in the non-bb templates and hence large uncertainties on the fit result are the consequence. Under the assumption that the ratio between the flavour fractions is modelled correctly in the simulation, non-signal elementary templates are combined to form composite templates. Table 6.7 summarises several combinations of templates that have been studied.

Table 6.7: Investigated combinations of template composition.

Name	Floating template groupings		
Combination A	$\mathcal{T}_{bb}$	=	$(\mathcal{T}_{bb})$
	$\mathcal{T}_{\overline{bb}}$	=	$(\mathcal{T}_{bc}, \mathcal{T}_{bl}, \mathcal{T}_{cc}, \mathcal{T}_{cl}, \mathcal{T}_{ll})$
Combination B	$\mathcal{T}_{bb}$	=	$(\mathcal{T}_{bb})$
	$\mathcal{T}_{1b}$	=	$(\mathcal{T}_{bc}, \mathcal{T}_{bl})$
	$\mathcal{T}_{0b}$	=	$(\mathcal{T}_{cc}, \mathcal{T}_{cl}, \mathcal{T}_{ll})$
Combination C	$\mathcal{T}_{bb}$	=	$(\mathcal{T}_{bb})$
	$\mathcal{T}_{cx}$	=	$(\mathcal{T}_{bc}, \mathcal{T}_{cc}, \mathcal{T}_{cl})$
	$\mathcal{T}_{lx}$	=	$(\mathcal{T}_{bl}, \mathcal{T}_{ll})$
Combination D	$\mathcal{T}_{bb}$	=	$(\mathcal{T}_{bb})$
	$\mathcal{T}_{cc}$	=	$(\mathcal{T}_{cc})$
	$\mathcal{T}_{\overline{bb},\overline{cc}}$	=	$(\mathcal{T}_{bc}, \mathcal{T}_{bl}, \mathcal{T}_{cl}, \mathcal{T}_{ll})$
Combination E	$\mathcal{T}_{bb}$	=	$(\mathcal{T}_{bb})$
	$\mathcal{T}_{\overline{ll}}$	=	$(\mathcal{T}_{bc}, \mathcal{T}_{bl}, \mathcal{T}_{cc}, \mathcal{T}_{cl})$
	$\mathcal{T}_{ll}$	=	$(\mathcal{T}_{ll})$

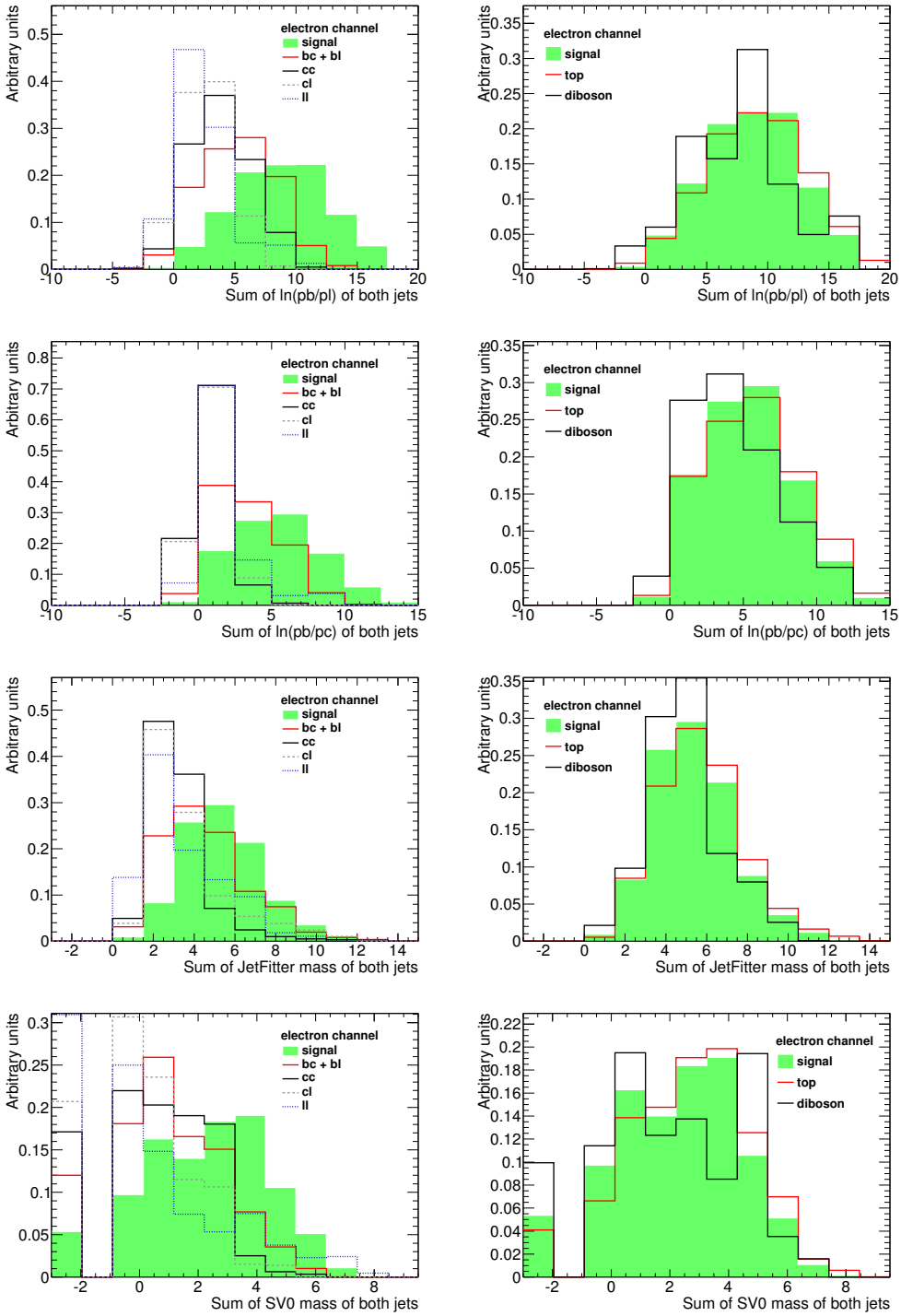

Figure 6.4: Electron channel fit templates constructed by (from top to bottom) the sum of $\ln(P_b/P_l)$, $\ln(P_b/P_c)$, the JetFitter mass and the SV0 mass of the two leading b-tagged jets. Left side: signal compared to other Z+jets background (for the sake of clarity, the templates containing a single true b-jet bc and bl were combined). Right side: signal shape compared to top and diboson backgrounds.

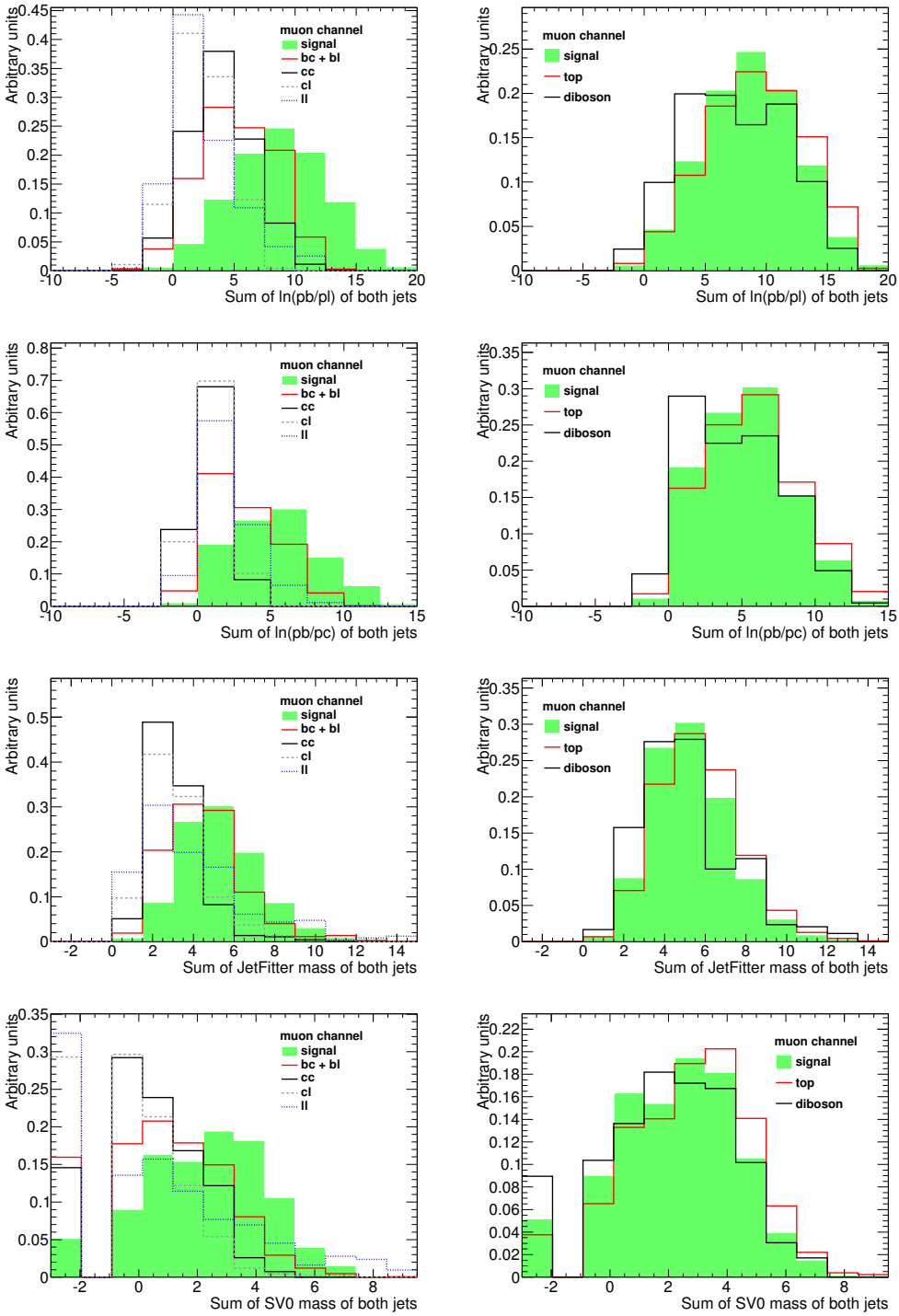

Figure 6.5: Muon channel fit templates constructed by (from top to bottom) the sum of $\ln(P_b/P_l)$, $\ln(P_b/P_c)$, the JetFitter mass and the SV0 mass of the two leading b-tagged jets. Left side: signal compared to other Z+jets background (for the sake of clarity, the templates containing a single true b-jet bc and bl were combined). Right side: signal shape compared to top and diboson backgrounds.

6.2.3 Decay reweighting for b-hadrons

The identification of b-jets is a fundamental ingredient in this analysis and hence the compatibility between the modelling of discriminating quantities in data and MC is crucial. A mismodelling in the b-tagging discriminating variables $\ln(P_b/P_l)$ and $\ln(P_b/P_c)$ (see Section 4.5) was observed in a $t\bar{t}$ control region with enriched b-jet content as depicted in Figure 6.6 for the leading and the sub-leading b-tagged jet. It is defined using the MC@NLO $t\bar{t}$ sample and requires one lepton and four or more jets of which exactly two are tagged with the MV1 tagger at the 75 % efficiency working point. The MC@NLO sample uses the same HERWIG version as the nominal ALPGEN signal sample and is therefore identical in terms of parton showering, hadronisation and b-hadron decay tables.

Both the $\ln(P_b/P_l)$ and the $\ln(P_b/P_c)$ variables are outputs of multivariate discriminators and rely on seven input variables. A detailed investigation of these variables came to the conclusion that the mismodelling is mainly caused by the total reconstructed number of tracks in the secondary vertex (nTrkAtVtx) used by the JetFitter algorithm. A comparison with a sample that uses the EvtGen package for decay of the hadronisation products was performed. As expected the EvtGen package with its up-to-date decay tables results in a better description of the distribution compared to data. As a consequence of this observation the HERWIG b-hadron decays are reweighted to match those obtained from EvtGen with the corresponding weights being constructed as a function of stable charged particles from the b-hadron decay that have $p_{\mathrm{T}} < 200\,\mathrm{MeV}$ and $|\eta| < 5.0$ (see Figure 6.7). The overall event weight is the product of the individual b-hadron decay weights. A detailed description of the reweighting and the underlying studies can be found in [63].

6.2.4 Template component reweighting

By combining the fit templates one increases the stability of the fit but one relies on the correct prediction of the flavour composition from simulation for the templates that are combined. However, a previous measurement of the cross section for the production of a Z boson in association with a single b-jet based on data recorded in 2010 indicates that one cannot make this assumption [101]. It has been observed that the fraction of b-jets is significantly underestimated by SHERPA and ALPGEN. This effect has been confirmed in the $Z + 1b$ measurement [63] that was performed in parallel to the analysis described in this thesis. The ratio between the measured and the predicted number of $Z + 1b$ events provides scale factor that could be applied to change the normalisations of the $\mathcal{T}_{bc}$ and the $\mathcal{T}_{bl}$ templates. However, it is not a priori certain that this scale factor is independent of the requirement of a second jet as it is the case here. Thus the single-b fraction fit has been repeated in an alternative event selection containing a reconstructed Z-boson with at least two jets of which at least one is tagged.

The fit equation is similar to Equation 6.10 while the floating part is given by:

$$\mathcal{T}_{\mathrm{Z}}(p) = f_b\,\mathcal{T}_b(p) \;+\; f_c\,\mathcal{T}_c(p) \;+\; f_l\,\mathcal{T}_l(p) \tag{6.15}$$

The templates were constructed using the $\ln(P_b/P_l)$ and the $\ln(P_b/P_c)$ outputs of the leading tagged jet. They are shown in Figure 6.8. Similar to the $Z + b\bar{b}$ case the shape of the $t\bar{t}$ and

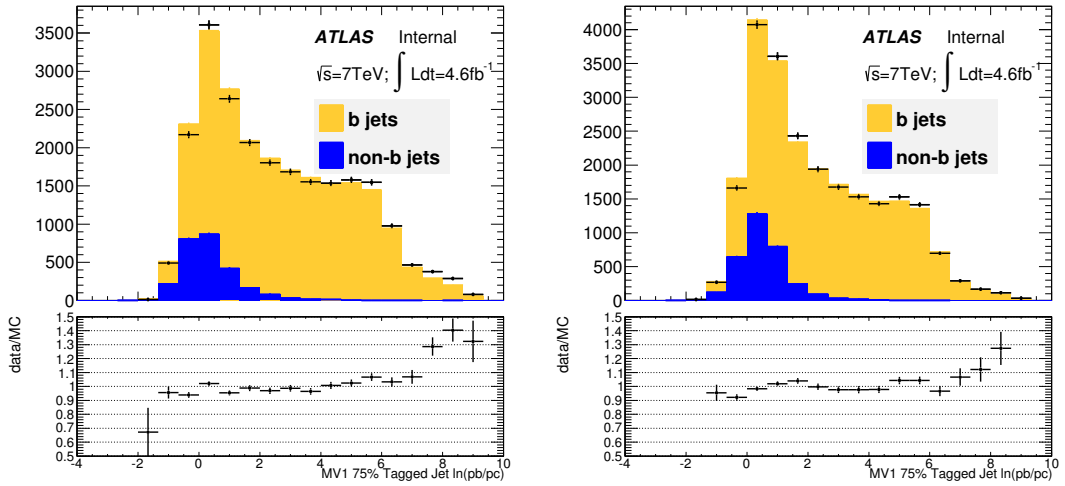

(a) leading jet

(b) subleading jet

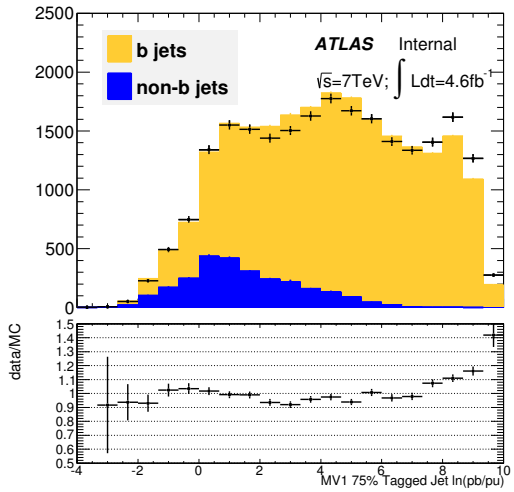

(c) leading jet

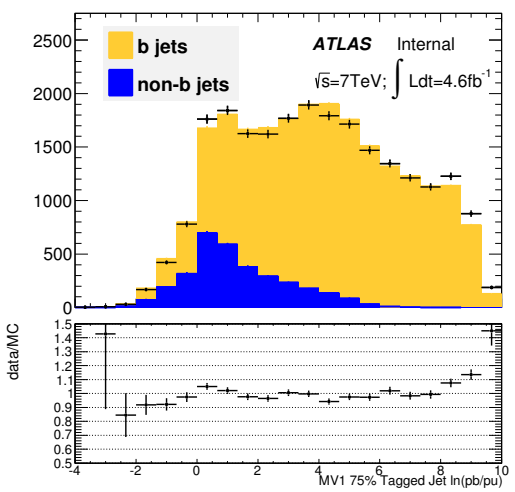

(d) sub-leading jet

Figure 6.6: The distributions of the $\ln(P_b/P_l)$ and $\ln(P_b/P_c)$ variables in a $t\bar{t}$ control region for the leading and sub-leading b-jets [63]. The MC distributions are normalised to data to highlight differences in the shape.

diboson backgrounds are degenerate and hence these normalisations are fixed in the fit. For the $\ln(P_b/P_c)$ distribution the charm jet and the light jet templates are almost identical and hence no separation is expected here. This is caused by the underlying b-jet selection using the MV1 weight which is optimised to separate b-jets from light jets and not to separate b-jets from c-jets as done for $\ln(P_b/P_c)$. $\ln(P_b/P_l)$ is therefore used as a baseline variable and $\ln(P_b/P_c)$ will be used to validate the scale-factor for the b-jet case. Furthermore, the shape of the templates in the electron and in the muon channel is very similar.

The results of the template fit are shown in Figure 6.9 and summarised in Table 6.8. The scale factors α_b, α_c and α_l are the ratio of the corresponding fit result and the MC prediction.

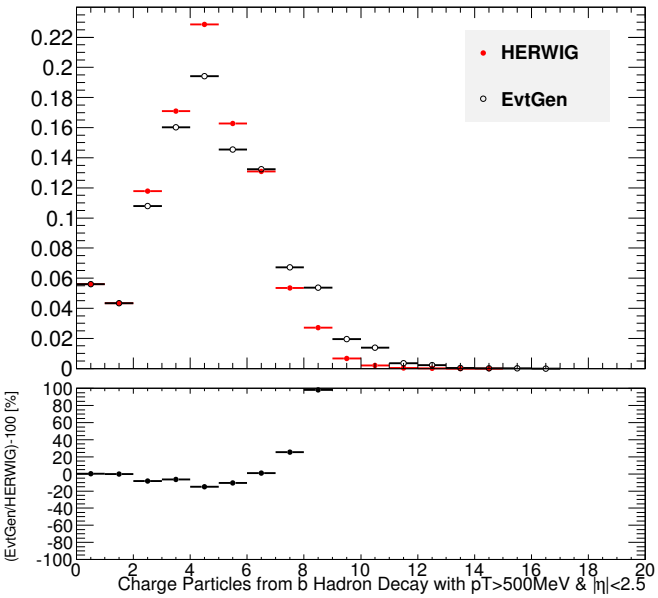

Figure 6.7: Number of stable charged particles from b-hadron decays using EvtGen (red) and HERWIG (black) for the hadron decay modelling [63]. Both distributions are normalised to unity.

The results in both channels are compatible with each other and therefore the result is combined by merging the templates from both channels before the fit.

As expected $\alpha_b = 1.37 \pm 0.05$ is deviating significantly from one. This value will be used in the $Z + b\bar{b}$ fit to correct the bc and bl templates normalisations. This value is compatible with the one obtained by using $\ln(P_b/P_c)$ as a fit variable. Both α_c and α_l are statistically compatible with unity. The corresponding templates in the $Z + b\bar{b}$ fit will not be rescaled though an uncertainty will be derived in Section 7.3.3 that covers the difference. As explained before, due to almost fully degenerate templates a fit on $\ln(P_b/P_c)$ is not able to distinguish between charm and light contributions.

6.2.5 Comparison between different fit methods and fit results

To find the optimal template composition the fit has been performed with all template combinations that are summarised in Table 6.7. The fit results and their correlation coefficients ρ are summarised for the electron channel in Table 6.9 and for the muon channel in Table 6.10. Both tables contain numbers obtained by using $\ln(P_b/P_l)$ as well as $\ln(P_b/P_c)$ as fit variables.

It can be seen that the statistical uncertainty on the fit result does not improve at all by using three-templates. Besides, in each of the three template combinations there is at least one pair of fit variables that are almost fully correlated or anti-correlated. It should also be mentioned that the results for N_{bb} are compatible with each other in all combinations. Given the fact that there are no improvements by using a three-template fit over a two-template fit the simplest approach represented by Combination A will be pursued as default template formation in both channels. The templates and fit results for Combination A are also depicted in Figures 6.10 and 6.11. For Combinations B to E the corresponding plots can be found in Appendix B.

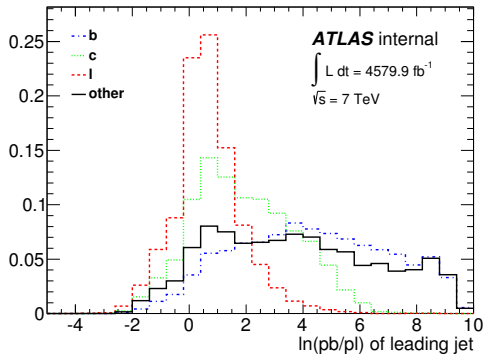

(a) $Z \to ee$ channel, $\ln(P_b/P_l)$

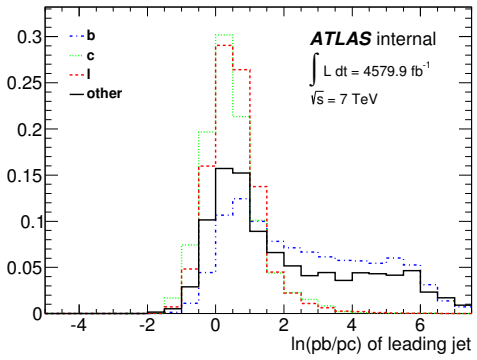

(b) $Z \to ee$ channel, $\ln(P_b/P_c)$

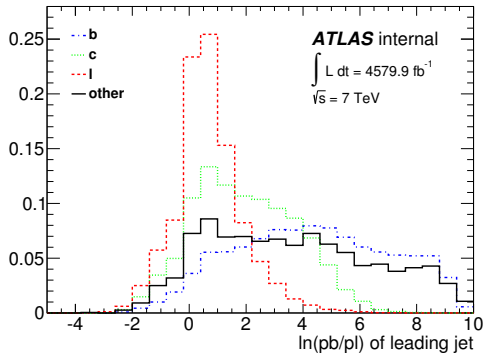

(c) $Z \to \mu\mu$ channel, $\ln(P_b/P_l)$

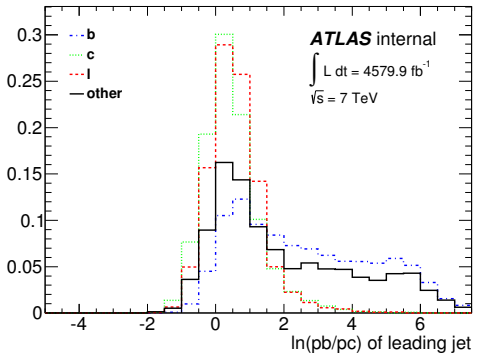

(d) $Z \to \mu\mu$ channel, $\ln(P_b/P_c)$

Figure 6.8: Fit templates for the single-b fit after Z+2jets selection with exactly one b-tag for the electron channel and the muon channel. Left side: $\ln(P_b/P_l)$, right side: $\ln(P_b/P_c)$

6.2.6 Validation of fit procedure

Statistical stability

In order to test the statistical stability of the fitting procedures described in Sections 6.2.4 and 6.2.1 pseudo-experiments have been performed. Each pseudo-experiment is built according to the following algorithm:

1. create toy distribution $D(p)$ for the set of n templates $\mathcal{T}_i$ with predefined normalisations N_i^{pre}

$$D^{\text{toy}}(p) = \sum_{i=1}^{n} N_i^{\text{pre}} \, \mathcal{T}_i(p) \tag{6.16}$$

2. specify the total normalisation N^{toy} of $D^{\text{toy}}(p)$ by randomly drawing from a Poissonian distribution with mean value N_{data}

3. create a pseudo-data histogram by drawing N^{toy} times events from $D^{\text{toy}}(p)$

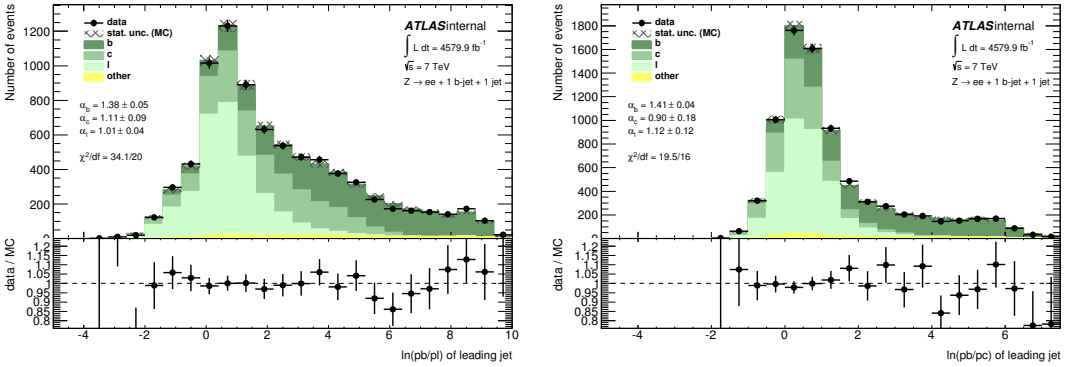

(a) $Z \to ee$ channel, $\ln(P_b/P_l)$

(b) $Z \to ee$ channel, $\ln(P_b/P_c)$

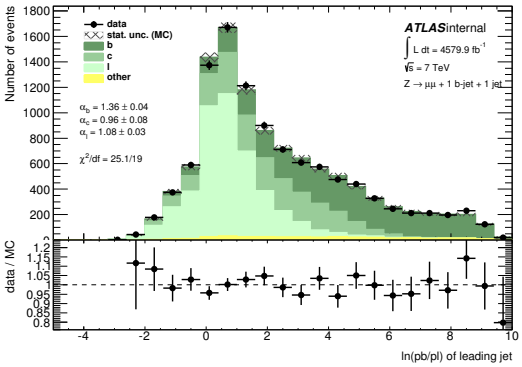

(c) $Z \to \mu\mu$ channel, $\ln(P_b/P_l)$

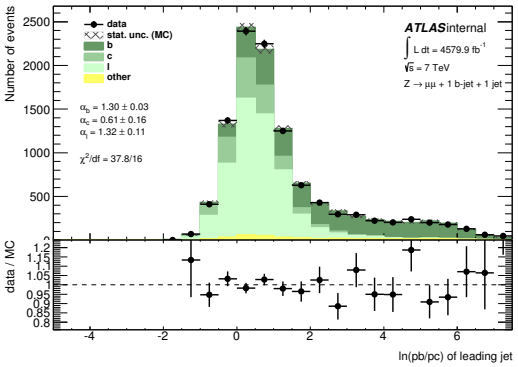

(d) $Z \to \mu\mu$ channel, $\ln(P_b/P_c)$

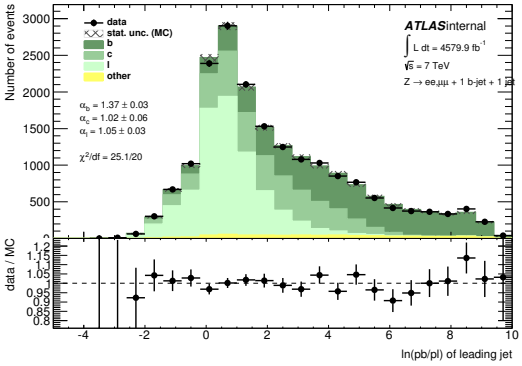

(e) Combined channel, $\ln(P_b/P_l)$

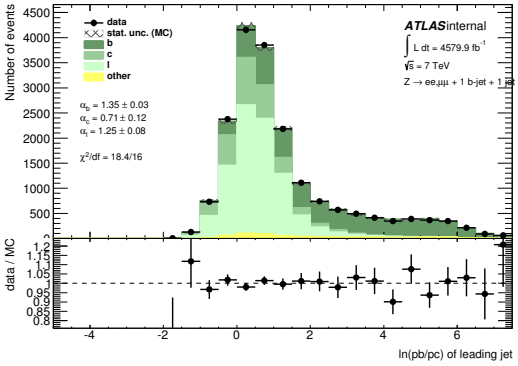

(f) Combined channel, $\ln(P_b/P_c)$

Figure 6.9: Fit results of the single-b fit after Z+2jets selection with exactly one b-tag for electron channel, muon channel and the combination of both. Left side: $\ln(P_b/P_l)$, right side: $\ln(P_b/P_c)$

4. perform the fit with the standard templates and store the fit result and the errors

A validator for the consistency of the likelihood fit procedure is the bias estimator. It is defined for each parameter in the fit as the difference between the predefined normalisation

Table 6.8: Results of the single flavour fraction fit for the single-b templates scale factors. The result $\alpha_b = 1.37 \pm 0.05$ obtained from fitting $\ln(P_b/P_l)$ is used. α_c and α_l are compatible with one and hence no scale factor is applied for the other templates in the $Z + b\bar{b}$ fit. By using $\ln(P_b/P_c)$ as a fit variable no discrimination between charm and light jets is possible. So these results are used only as a cross-check to α_b.

		$Z \to ee$ channel	$Z \to \mu\mu$ channel	combined channel
$\ln(P_b/P_l)$	α_b	1.38 ± 0.09	1.36 ± 0.07	1.37 ± 0.05
	α_c	1.11 ± 0.13	0.96 ± 0.10	1.02 ± 0.08
	α_l	1.01 ± 0.06	1.08 ± 0.05	1.05 ± 0.04
	$N_Z \cdot f_b$	2623 ± 94	3533 ± 109	6157 ± 145
	$N_Z \cdot f_l$	2077 ± 167	2413 ± 190	4486 ± 254
	$N_Z \cdot f_l$	2983 ± 121	4394 ± 140	7382 ± 186
$\ln(P_b/P_c)$	α_b	1.41 ± 0.07	1.30 ± 0.06	1.35 ± 0.04
	$N_Z \cdot f_b$	2638 ± 78	3348 ± 88	5976 ± 118

N_i^{pre} and the fitted value N_i:

$$\text{bias}_i = N_i - N_i^{\text{pre}} \tag{6.17}$$

An extension of the bias is the pull variable. It is defined as the ratio of the bias and the error $\sigma(N_i)$ of the parameter N_i obtained from the fit:

$$\text{pull}_i = \frac{N_i - N_i^{\text{pre}}}{\sigma(N_i)} \tag{6.18}$$

Ideally the pull distribution over all pseudo experiments should be a normal distribution, i.e. a Gaussian function with a mean value of zero and a standard deviation of one. A significantly shifted mean value would indicate a bias in the measurement of the corresponding parameter. A standard deviation larger than one would hint at an underestimation of the error while a standard deviation smaller than one would indicate an overestimation of the error.

The pull distributions for N_{bb} and $N_{\overline{bb}}$ for 50000 pseudo-experiments are shown in Figure C.3. A Gaussian distribution has been fitted to the pull distribution. No significant deviations from a standard distribution can be observed.

A consistent estimator is supposed to yield the true parameter on average. To verify this requirement, the pseudo-data distribution has been generated with different heavy flavour fractions and hence different N_i. They vary between 50 % and 150 % in steps of 10 % around the nominal value for N_{bb} and $N_{\overline{bb}}$. For each initial assumption 10000 pseudo-experiments have been generated. The resulting so-called linearity plot is shown in Figure C.4 where the average fitted result is plotted on the y-axis whereas the true generated value is plotted on the x-axis. Both are normalised to the nominal N_i and a fit to a linear function of the form $y(x) = ax + b$ has been performed where a and b are in good agreement with one and zero respectively. It

Table 6.9: Correlation coefficients and fit results for different compositions of fit templates in the electron channel.

	$\ln(P_b/P_c)$		$\ln(P_b/P_l)$	
Name	Corr. coeff.	Fit result	Corr. coeff.	Fit result
Comb. A	$\rho(N_{bb}, N_{\overline{bb}}) = -0.53$	$N_{bb} = 469 \pm 35$	$\rho(N_{bb}, N_{\overline{bb}}) = -0.49$	$N_{bb} = 468 \pm 34$
		$N_{\overline{bb}} = 366 \pm 31$		$N_{\overline{bb}} = 365 \pm 29$
Comb. B	$\rho(N_{bb}, N_{1b}) = -0.84$	$N_{bb} = 429 \pm 59$	$\rho(N_{bb}, N_{1b}) = -0.76$	$N_{bb} = 463 \pm 49$
	$\rho(N_{bb}, N_{0b}) = +0.53$	$N_{1b} = 197 \pm 81$	$\rho(N_{bb}, N_{0b}) = +0.50$	$N_{1b} = 141 \pm 75$
	$\rho(N_{1b}, N_{0b}) = -0.78$	$N_{0b} = 209 \pm 38$	$\rho(N_{1b}, N_{0b}) = -0.84$	$N_{0b} = 228 \pm 44$
Comb. C	$\rho(N_{bb}, N_{cx}) = +0.42$	$N_{bb} = 461 \pm 40$	$\rho(N_{bb}, N_{cx}) = -0.62$	$N_{bb} = 494 \pm 42$
	$\rho(N_{bb}, N_{lx}) = -0.54$	$N_{cx} = 92 \pm 94$	$\rho(N_{bb}, N_{lx}) = +0.43$	$N_{cx} = 37 \pm 87$
	$\rho(N_{cx}, N_{lx}) = -0.96$	$N_{lx} = 282 \pm 114$	$\rho(N_{cx}, N_{lx}) = -0.91$	$N_{lx} = 302 \pm 66$
Comb. D	$\rho(N_{bb}, N_{cc}) = +0.63$	$N_{bb} = 446 \pm 48$	$\rho(N_{bb}, N_{cc}) = -0.00$	$N_{bb} = 470 \pm 34$
	$\rho(N_{bb}, N_{\overline{bb,cc}}) = -0.76$	$N_{cc} = 47 \pm 51$	$\rho(N_{bb}, N_{\overline{bb,cc}}) = -0.50$	$N_{cc} = 0 \pm 81$
	$\rho(N_{cc}, N_{\overline{bb,cc}}) = -0.92$	$N_{\overline{bb,cc}} = 341 \pm 87$	$\rho(N_{cc}, N_{\overline{bb,cc}}) = -0.03$	$N_{\overline{bb,cc}} = 363 \pm 30$
Comb. E	$\rho(N_{bb}, N_{\overline{bb,ll}}) = -0.34$	$N_{bb} = 469 \pm 36$	$\rho(N_{bb}, N_{\overline{bb,ll}}) = -0.66$	$N_{bb} = 475 \pm 41$
	$\rho(N_{bb}, N_{ll}) = +0.15$	$N_{\overline{bb,ll}} = 272 \pm 83$	$\rho(N_{bb}, N_{ll}) = +0.48$	$N_{\overline{bb,ll}} = 251 \pm 70$
	$\rho(N_{\overline{bb,ll}}, N_{ll}) = -0.93$	$N_{ll} = 94 \pm 72$	$\rho(N_{\overline{bb,ll}}, N_{ll}) = -0.88$	$N_{ll} = 107 \pm 45$

should be mentioned here that the error bars represent the RMS of the fitted values and not the statistical uncertainty.

The pull and linearity distributions have also been generated with the templates constructed by using $\ln(P_b/P_l)$ instead of $\ln(P_b/P_c)$. They can be found in Appendix C.1. Furthermore the fit procedure that was used to obtain the single-b template scale factor (see Section 6.2.4) has been subjected to the same validation procedure for which no irregularities have been found. See Appendix D.

Stability under variations of bin size

When using a binned maximum likelihood fit it should be checked that the fitted result is not significantly depending on the binning. The fit has been performed by using 10 bins in the parameter range between −10 and 15. Since this is a somewhat arbitrary choice that was agreed on before it has to be validated that different binnings yield compatible results. The number of bins has been varied between 4 and 80 yielding an agreement within the statistical uncertainty obtained from the fit. The results for N_{bb} and $N_{\overline{bb}}$ is shown in Figure 6.14.

Table 6.10: Correlation coefficients and fit results for different composition of fit templates in the muon channel.

	$\ln(P_b/P_c)$		$\ln(P_b/P_l)$	
Name	Corr. coeff.	Fit result	Corr. coeff.	Fit result
Comb. A	$\rho(N_{bb}, N_{\overline{bb}}) = -0.57$	$N_{bb} = 720 \pm 44$	$\rho(N_{bb}, N_{\overline{bb}}) = -0.52$	$N_{bb} = 700 \pm 42$
		$N_{\overline{bb}} = 478 \pm 37$		$N_{\overline{bb}} = 497 \pm 35$
Comb. B	$\rho(N_{bb}, N_{1b}) = -0.87$	$N_{bb} = 683 \pm 80$	$\rho(N_{bb}, N_{1b}) = -0.76$	$N_{bb} = 665 \pm 59$
	$\rho(N_{bb}, N_{0b}) = +0.66$	$N_{1b} = 232 \pm 125$	$\rho(N_{bb}, N_{0b}) = +0.49$	$N_{1b} = 245 \pm 90$
	$\rho(N_{1b}, N_{0b}) = -0.88$	$N_{0b} = 283 \pm 62$	$\rho(N_{1b}, N_{0b}) = -0.83$	$N_{bb} = 682 \pm 49$
Comb. C	$\rho(N_{bb}, N_{cx}) = +0.22$	$N_{bb} = 677 \pm 46$	$\rho(N_{bb}, N_{cx}) = -0.58$	$N_{cx} = 227 \pm 87$
	$\rho(N_{bb}, N_{lx}) = -0.50$	$N_{cx} = 0 \pm 32$	$\rho(N_{bb}, N_{lx}) = +0.34$	$N_{lx} = 288 \pm 65$
	$\rho(N_{cx}, N_{lx}) = -0.85$	$N_{lx} = 520 \pm 75$	$\rho(N_{cx}, N_{lx}) = -0.88$	$N_{0b} = 288 \pm 52$
Comb. D	$\rho(N_{bb}, N_{cc}) = +0.67$	$N_{bb} = 666 \pm 62$	$\rho(N_{bb}, N_{cc}) = -0.20$	$N_{bb} = 696 \pm 42$
	$\rho(N_{bb}, N_{\overline{bb,cc}}) = -0.79$	$N_{cc} = 23 \pm 68$	$\rho(N_{bb}, N_{\overline{bb,cc}}) = +0.01$	$N_{cc} = 175 \pm 95$
	$\rho(N_{cc}, N_{\overline{bb,cc}}) = -0.93$	$N_{\overline{bb,cc}} = 508 \pm 116$	$\rho(N_{cc}, N_{\overline{bb,cc}}) = -0.93$	$N_{\overline{bb,cc}} = 327 \pm 92$
Comb. E	$\rho(N_{bb}, N_{\overline{bb,ll}}) = +0.10$	$N_{bb} = 707 \pm 44$	$\rho(N_{bb}, N_{\overline{bb,ll}}) = -0.63$	$N_{bb} = 686 \pm 48$
	$\rho(N_{bb}, N_{ll}) = -0.23$	$N_{\overline{bb,ll}} = 112 \pm 155$	$\rho(N_{bb}, N_{ll}) = +0.43$	$N_{\overline{bb,ll}} = 401 \pm 79$
	$\rho(N_{\overline{bb,ll}}, N_{ll}) = -0.97$	$N_{ll} = 378 \pm 162$	$\rho(N_{\overline{bb,ll}}, N_{ll}) = -0.87$	$N_{ll} = 110 \pm 51$

6.3 Unfolding to particle level

In order to allow comparisons of the measured cross sections with other experiments and with theoretical predictions the result needs to be transformed to truth-particle level. To achieve this one has to correct for detector and reconstruction inefficiencies as well as resolution effects. This transformation is achieved by introducing a correction factor $\mathcal{U}$ (see Equation 6.1), defined as the ratio of the number of reconstructed signal events N_{bb}^{reco} over the number of signal events on particle level N_{bb}^{truth}:

$$\mathcal{U} = \frac{N_{Z+bb}^{\text{reco}}}{N_{Z+bb}^{\text{truth}}} \tag{6.19}$$

The particle level event selection is described in Section 5.2.3. In order not to be affected by misidentification, but to ensure that in this step only actual signal events are considered, the b-tagged jets on reconstruction level are additionally required to be matched to b-hadrons as it is done for the truthjets on particle level. The particle level event selection is defined so as to not extrapolate to a significantly larger phase space, but to maintain as closely as possible the phase space related selection used for the fit. Therefore the only extrapolation results from an extension of the acceptance region of the signal electrons from $|\eta| < 2.47$ to $|\eta| < 2.5$ to ensure

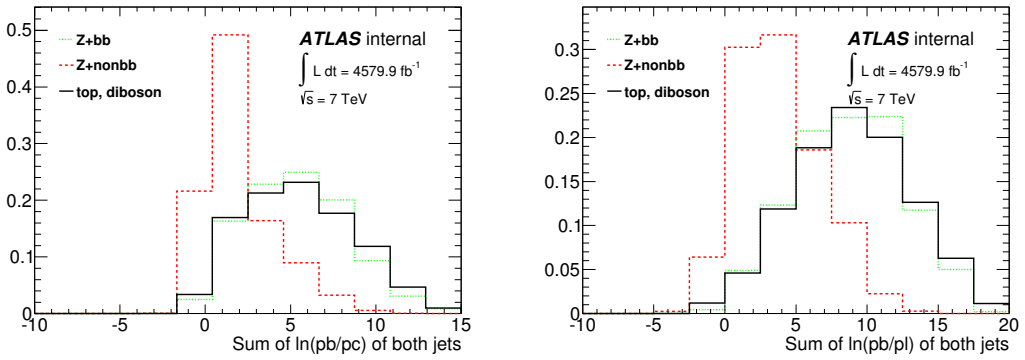

(a) $Z \to ee$ channel, $\ln(P_b/P_c)$

(b) $Z \to ee$ channel, $\ln(P_b/P_l)$

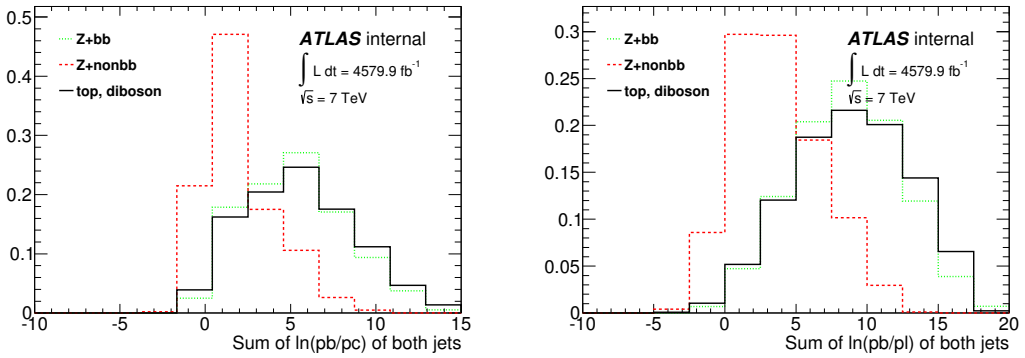

(c) $Z \to \mu\mu$ channel, $\ln(P_b/P_c)$

(d) $Z \to \mu\mu$ channel, $\ln(P_b/P_l)$

Figure 6.10: Fit templates for Combination A using two floating templates: a signal template T_{bb} and one non-bb template $T_{\overline{bb}}$ Left side: $\ln(P_b/P_l)$, right side: $\ln(P_b/P_c)$

a consistent phase space definition for the electron and the muon channel.

The analysis is performed at a b-tagging operation point with an efficiency of 75 %. Hence the efficiency for tagging both b-jets ϵ_{2b} is of the order of 50 % which is the largest contribution to the unfolding. To monitor the sensitivity of the b-tagging efficiency to systematic variations and to ensure the independence of this quantity from the analysis channel it is extracted from the unfolding factor $\mathcal{U}$ which becomes:

$$\begin{aligned} \mathcal{U} &= \epsilon_{2b} \cdot C \\ &= \frac{N^{\text{reco}}_{Z+bb}}{N^{\text{reco}}_{Z+jj}} \cdot \frac{N^{\text{reco}}_{Z+jj}}{N^{\text{truth}}_{Z+bb}} \end{aligned} \tag{6.20}$$

Here N^{reco}_{Z+jj} corresponds to the number of reconstructed Z events with at least two additional jets that are matched to a b-hadron in a similar way as it was required for N^{reco}_{bb}. All the other efficiencies are included in the correction factor C. A further split-up of the efficiencies is not applied: the jet reconstruction efficiency is above 80 % and the efficiency of the MET cut is almost 100 % and an extraction of the Z reconstruction efficiency or anything at an earlier stage

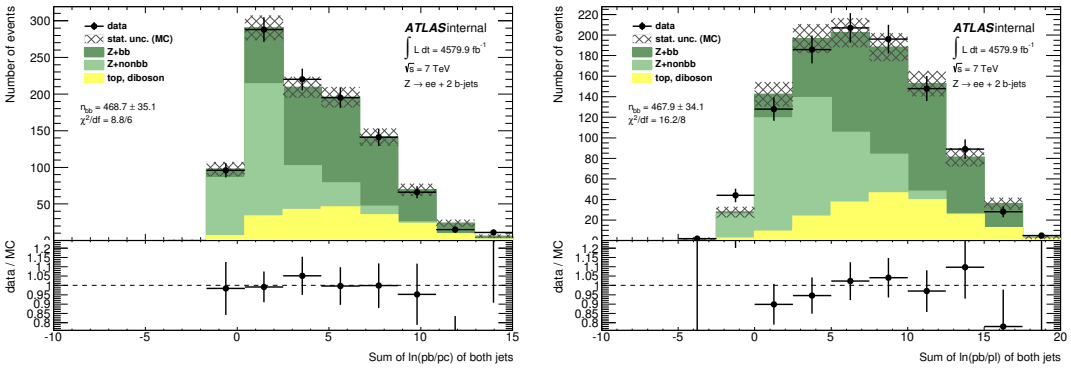

(a) $Z \to ee$ channel, $\ln(P_b/P_c)$

(b) $Z \to ee$ channel, $\ln(P_b/P_l)$

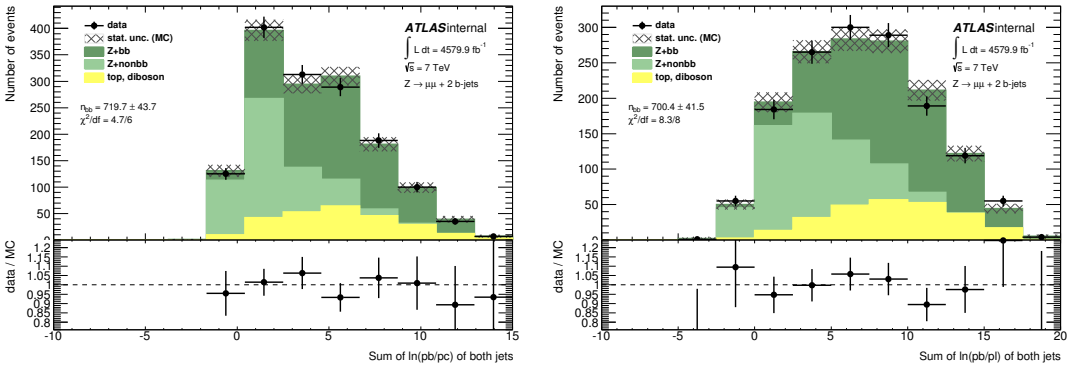

(c) $Z \to \mu\mu$ channel, $\ln(P_b/P_c)$

(d) $Z \to \mu\mu$ channel, $\ln(P_b/P_l)$

Figure 6.11: Fit results for Combination A using two floating templates: a signal template $\mathcal{T}_{bb}$ and one non-bb template $\mathcal{T}_{\overline{bb}}$

of the selection was not possible for technical reasons.

As a consequence of lepton universality identical cross sections for the electron and the muon channel are expected. However, it is observed that the presented measurements are not in perfect agreement and show a difference of $1.65\,\sigma$ between the electron channel and the muon channel by considering only uncorrelated, statistical uncertainties. Studies into possible reasons conclude that this difference is a statistical fluctuation: a number of checks have been performed when running the analysis with a modified phase space or different event selection:

- To exclude the impact of soft jets as a possible cause for the difference the analysis has been performed with low energetic jets with p_{T} between 20 and 30 GeV and separately with jets above 30 GeV.

- Only central jets with $|y| > 1.2$ were selected.

- Only central leptons with $|\eta| > 1.32$ that are not in the transition region between the calorimeter systems were selected.

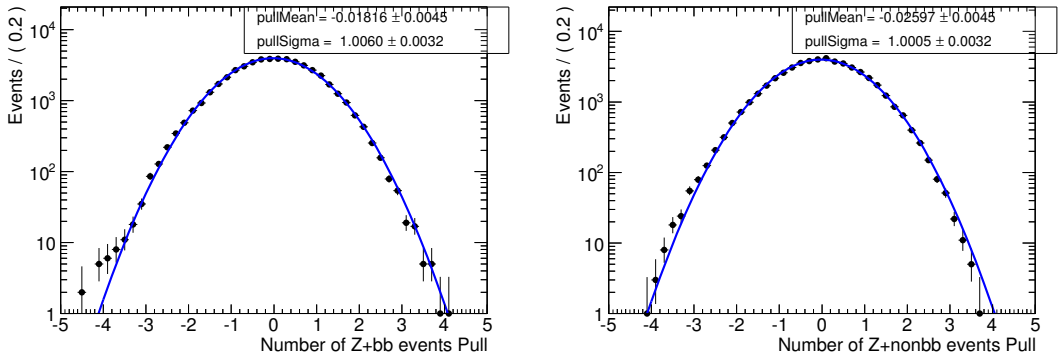

(a) $Z \to ee$ channel, N_{bb} (b) $Z \to ee$ channel, $N_{\overline{bb}}$

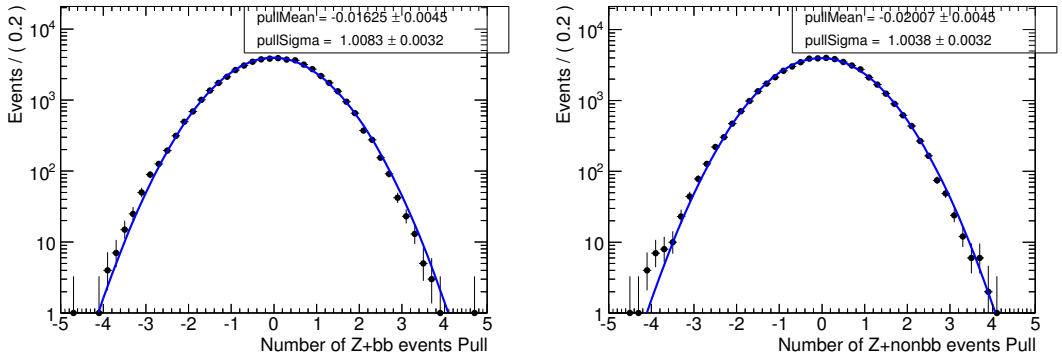

(c) $Z \to \mu\mu$ channel, N_{bb} (d) $Z \to \mu\mu$ channel, $N_{\overline{bb}}$

Figure 6.12: Pull distributions for fitting with $\ln(P_b/P_c)$. Left side: N_{bb}, right side: $N_{\overline{bb}}$

Table 6.11: Summary of fit and unfolding in the electron and muon channel.

term	electron channel	muon channel
N^{reco}_{Z+bb}	380.6 ± 6.3	500.4 ± 7.1
N^{reco}_{Z+jj}	767.5 ± 9.2	1027.8 ± 11.0
N^{truth}_{Z+bb}	1796.2 ± 14.5	1802.9 ± 14.8
Efficiency ϵ_{2b}	0.496 ± 0.010	0.487 ± 0.009
Correction factor C	0.427 ± 0.006	0.570 ± 0.008
Fitted signal $n_{\text{2b,fit},\ell}$	469.0 ± 35.4	719.6 ± 44.0
Luminosity $\mathcal{L}$ [fb^{-1}]	4579.9 ± 82.4	
$\sigma(Z + b\bar{b}) \cdot BR$ [pb]	0.483 ± 0.036	0.566 ± 0.035

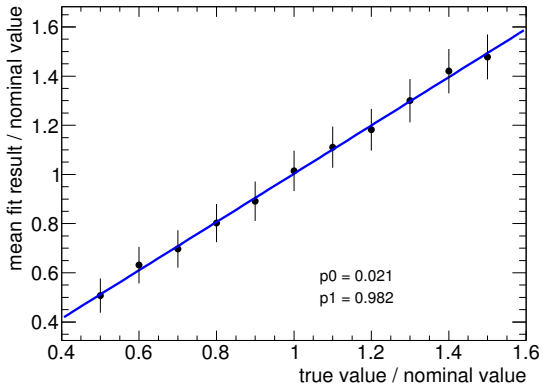

(a) $Z \to ee$ channel, N_{bb}

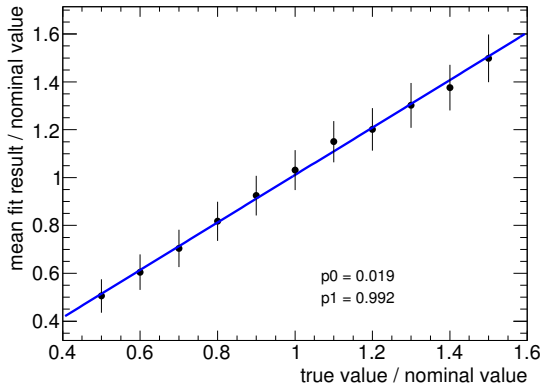

(b) $Z \to ee$ channel, $N_{\overline{bb}}$

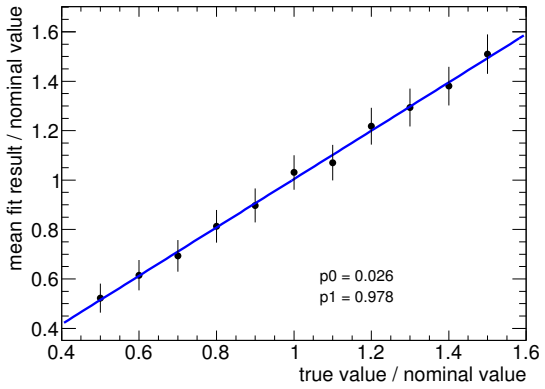

(c) $Z \to \mu\mu$ channel, N_{bb}

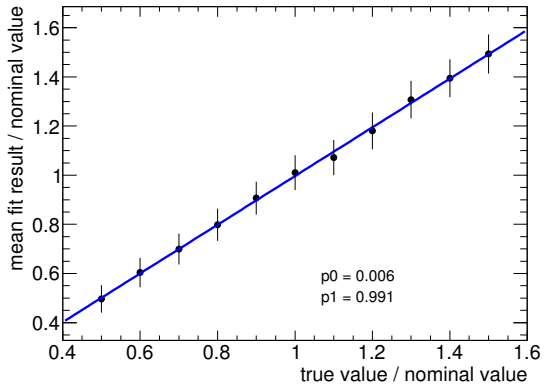

(d) $Z \to \mu\mu$ channel, $N_{\overline{bb}}$

Figure 6.13: Linearity distributions for fitting with $\ln(P_b/P_c)$. The error bars in these plots do not represent the statistical uncertainty, but the RMS of the fitted values. Left side: N_{bb}, right side: $N_{\overline{bb}}$

- The analysis has been performed with different E_T^{miss} cuts and also without any E_T^{miss} cut at all since the contribution from electrons to the E_T^{miss} is much larger compared to the contribution from muons (see Figure 4.4 on page 38).
- The analysis has been repeated for periods with identical trigger conditions and periods with identical pileup conditions.
- Both overlap removals, the one between jets and leptons and the one between electrons and muons, have been varied.
- The lepton isolation requirement has been varied.
- The fit has been repeated with exchanged templates, i.e. the fit in the electron channel has been performed with templates from the muon channel and vice versa.

However, none of these investigations indicates a specific problem in the comparison. Hence, we conclude that the difference is caused by a statistical fluctuation.

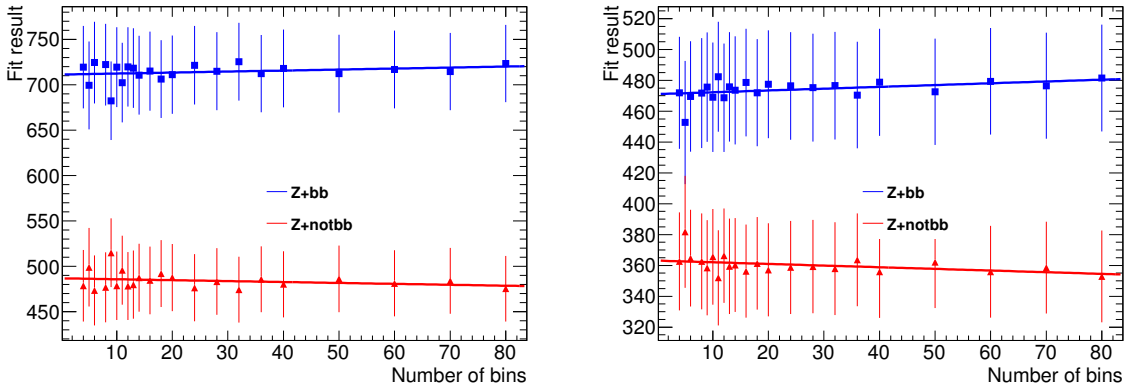

(a) $Z \to \mu\mu$ channel

(b) $Z \to \mu\mu$ channel

Figure 6.14: Fitted result for N_{bb} and $N_{\overline{bb}}$ as a function of the number of bins that are used in the fit. Left side: muon channel, right side: electron channel

6.4 Combination of electron and muon channel

The measurement has a statistical uncertainty of about 7 % in each channel. The statistical precision is increased by combining the electron and the muon channel. The combination in the fit is performed by merging the templates from both channels into a single set of templates and perform the fit afterwards. The templates for the combined fit are shown in Figures 6.15a and (b). The results of the combined fit are displayed in Figures 6.15c and (d). The same procedure for the fit validation as described in Section 6.2.6 has been applied to the combined fit and the checks are summarised in Appendix C.2.

For the unfolding the combination has been performed simply by summing the events of both channels. The fit result and the unfolding factors are summarised in Table 6.12. The combined statistical uncertainty is about 5 %.

The combined cross section is

$$\sigma(Z + b\bar{b}) = 0.522 \pm 0.025 \tag{6.21}$$

where the uncertainty includes only the statistical component. In the next chapter the systematic uncertainties that were studied are presented and summarised.

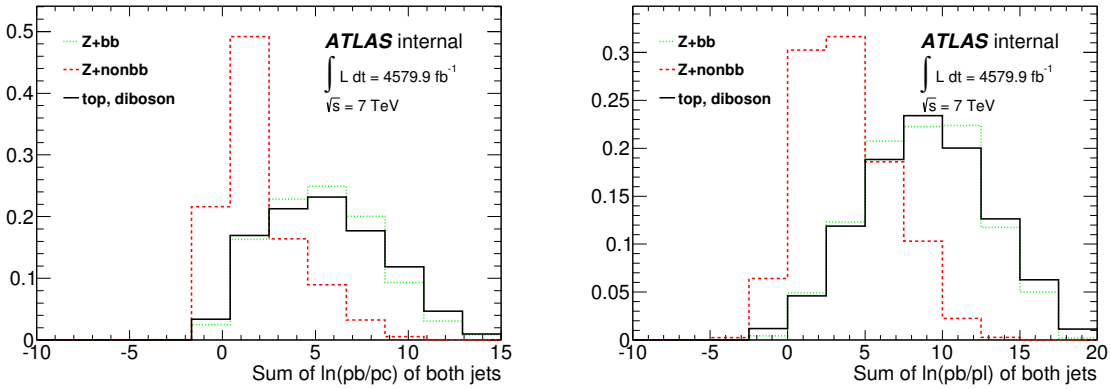

(a) $\ln(P_b/P_c)$ (b) $\ln(P_b/P_l)$

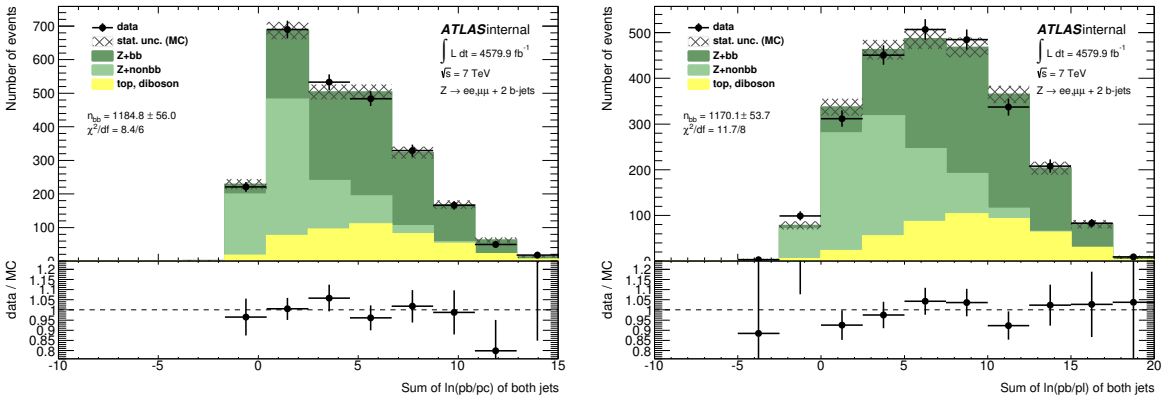

(c) $\ln(P_b/P_c)$ (d) $\ln(P_b/P_l)$

Figure 6.15: Combination of the fit in the electron and in the muon channel. (a) and (b) show the templates for $\ln(P_b/P_c)$ and $\ln(P_b/P_l)$, (c) and (d) show the fitted results.

Table 6.12: Summary of fit and unfolding in the combined channel.

term	combined channel
N^{reco}_{Z+bb}	880.5 ± 6.8
N^{reco}_{Z+jj}	1794.5 ± 10.2
N^{truth}_{Z+bb}	3599.3 ± 14.6
Efficiency ϵ_{2b}	0.491 ± 0.005
Correction factor C	0.499 ± 0.003
Fitted signal $n_{2\text{b,fit},\ell}$	1184.8 ± 56.4
Luminosity $\mathcal{L}$ [fb^{-1}]	4579.9 ± 82.4
$\sigma(Z + b\bar{b}) \cdot BR$ [pb]	0.522 ± 0.025

CHAPTER 7

Systematic Uncertainties

This chapter describes the influence of a wide range of systematic uncertainties on the measurement. Technically they can enter the analysis through the fit by changing the template shapes or the background normalisations and in the unfolding. For each uncertainty the entire analysis chain is repeated with modified assumptions as described below. Unless otherwise stated, all systematic shifts are applied to the MC simulation and the difference compared to the nominal result is assigned as systematic uncertainty.

The combination of all individual systematic uncertainties is described in Section 7.11. Different sources of systematic uncertainties are combined by adding them in quadrature.

7.1 Uncertainty on the b-tagging efficiency

The dominant systematic effect in this analysis is caused by the uncertainty on the b-tagging efficiency scale factors. These scale factors are applied to MC simulation in order to match the efficiency for each flavour to that in the selected data events (see Section 4.5). The efficiency scale factors as well as the uncertainties derived from different methods are shown in Figure 7.1 for an operating point similar to the one that is used in this analysis.

The corresponding uncertainty is derived as a function of jet p_{T} and η. The scale factors for the efficiency of tagging b-, c- and light flavoured jets are varied up and down independently by one standard deviation of the respective measurement error. Simultaneously the corresponding inefficiency scale factors are varied in the opposite direction. Each of the resulting six variations is propagated through the fit (with regenerated templates) and the unfolding procedure. The corresponding systematic variations have been obtained by summing components in quadrature. The results are summarised in Table 7.1. By far the largest uncertainty, more than 10 %, is obtained from the b-jet scale factor variation whereas the c-jet scale factor variation results in about 2 %. The light-jet variations have no impact at all.

The method as described above varies all scale factors in all nine jet p_{T} bins simultaneously and is hence based on the assumption that the uncertainties among the bins are fully correlated. To account for the correlations the so-called eigenvector method is introduced. It is based on

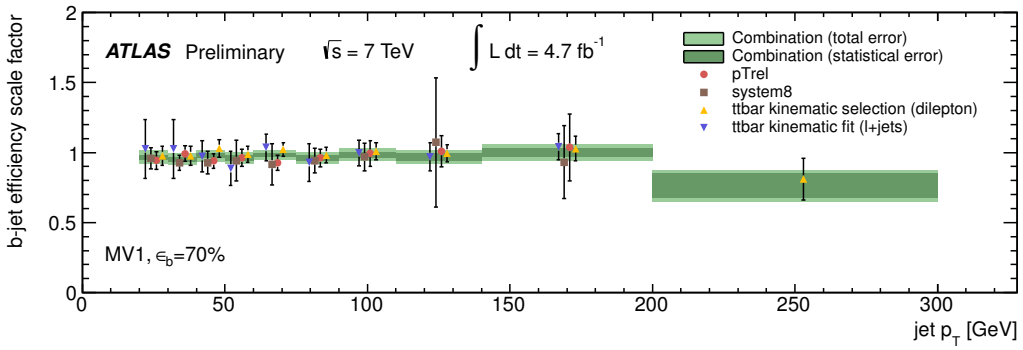

Figure 7.1: The b-jet tagging efficiency data-to-simulation scale factors and uncertainties for the MV1 algorithm at 70 % efficiency. The scale factors are obtained with dijet-based p_T^{rel} and System8 methods and with $t\bar{t}$ based methods [102].

Table 7.1: Relative uncertainty (in %) on b-tagging scale factors propagated to the fit stage, the unfolding stage and to the final cross section for the electron and the muon channel. The up and down variations are represented by the arrows ↑ and ↓.

	electron channel				muon channel			
Systematic	$n_{2b,fit,e}$	$\epsilon_{2b,e}$	C_e	σ_e	$n_{2b,fit,\mu}$	$\epsilon_{2b,\mu}$	C_μ	σ_μ
b jet eff. ↑	-3.65	+7.72	+0.69	-11.18	-3.24	+7.83	+0.58	-10.78
b jet eff. ↓	+3.53	-7.49	-0.69	+12.69	+3.18	-7.59	-0.56	+12.29
c jet eff. ↑	+2.21	-0.05	+0.01	+2.25	+2.20	+0.01	+0.03	+2.15
c jet eff. ↓	-2.47	+0.05	-0.01	-2.51	-2.42	-0.01	-0.03	-2.38
l jet eff. ↑	-	-	-	-	-	-	-	-
l jet eff. ↓	-	-	-	-	-	-	-	-

the scale factor covariance matrix which is constructed as

$$COV_{ij} = \sum_{i=1}^{N_{\text{bins}}} \sum_{j=1}^{N_{\text{bins}}} \sum_{k=1}^{N_{\text{unc}}} (\mathbf{SF}_{i,\text{syst}(k)} - \mathbf{SF}_{i,\text{nominal}})\,(\mathbf{SF}_{j,\text{syst}(k)} - \mathbf{SF}_{j,\text{nominal}}) \tag{7.1}$$

with the number of p_{T} bins $N_{\text{bins}} = 9$ and N_{unc} all uncertainty components that contribute to the total b-tagging scale factor uncertainty.

By inverting and diagonalising the covariance matrix nine independent scale factor variations along the eigenvector directions are obtained. For each of these variations the scale factors in all p_{T} bins are varied by the corresponding eigenvector. The variations are summarised in Table 7.2. The combined uncertainty is obtained by summing the nine individual variations in quadrature. By considering the correlations correctly the total uncertainty on b-jets has been decreased significantly from more than 10 % to about 6 %.

Table 7.2: Relative uncertainty (in %) on b-tagging scale factors by using an eigenvector decomposition of the nine p_{T} bin variations for b-jets. The uncertainties are propagated to the fit stage, the unfolding stage and to the final cross section for the electron and the muon channel. The up and down variations are represented by the arrows ↑ and ↓.

	electron channel				muon channel			
Systematic	$n_{\mathrm{2b,fit,e}}$	$\epsilon_{\mathrm{2b,e}}$	C_{e}	σ_e	$n_{\mathrm{2b,fit},\mu}$	$\epsilon_{\mathrm{2b},\mu}$	C_μ	σ_μ
b jet EV 0 ↑	-0.11	-0.04	+0.10	-0.17	-0.09	-0.01	+0.08	-0.16
b jet EV 0 ↓	+0.11	+0.04	-0.10	+0.17	+0.09	+0.01	-0.08	+0.16
b jet EV 1 ↑	+0.08	+0.03	-0.08	+0.14	+0.03	+0.01	-0.09	+0.11
b jet EV 1 ↓	-0.08	-0.03	+0.08	-0.14	-0.03	-0.01	+0.09	-0.11
b jet EV 2 ↑	-0.03	+0.01	-0.01	-0.04	-0.01	+0.02	+0.01	-0.03
b jet EV 2 ↓	+0.03	-0.01	+0.01	+0.04	+0.01	-0.02	-0.01	+0.03
b jet EV 3 ↑	+0.07	-0.03	+0.10	-	+0.06	-0.01	+0.09	-0.02
b jet EV 3 ↓	-0.07	+0.03	-0.10	-	-0.06	+0.01	-0.09	+0.02
b jet EV 4 ↑	-0.05	+0.06	-0.23	+0.12	-0.06	+0.07	-0.26	+0.13
b jet EV 4 ↓	+0.05	-0.06	+0.23	-0.12	+0.06	-0.07	+0.26	-0.13
b jet EV 5 ↑	-0.06	-0.07	+0.40	-0.38	-0.11	-0.08	+0.40	-0.42
b jet EV 5 ↓	+0.06	+0.07	-0.39	+0.38	+0.11	+0.08	-0.40	+0.42
b jet EV 6 ↑	-0.24	-0.02	+0.14	-0.36	-0.26	-0.02	+0.15	-0.39
b jet EV 6 ↓	+0.24	+0.02	-0.14	+0.36	+0.26	+0.02	-0.15	+0.39
b jet EV 7 ↑	-0.14	-0.61	+2.49	-1.96	-0.11	-0.61	+2.49	-1.94
b jet EV 7 ↓	+0.13	+0.63	-2.45	+2.01	+0.11	+0.63	-2.46	+1.99
b jet EV 8 ↑	+1.85	+1.13	-5.05	+6.07	+1.70	+1.25	-5.16	+5.91
b jet EV 8 ↓	-1.88	-1.07	+5.19	-5.71	-1.74	-1.18	+5.30	-5.57
Combined b jet eff. ↑	+1.88	+1.29	+5.65	+6.41	+1.73	+1.40	+5.75	+6.25
Combined b jet eff. ↓	-1.91	-1.25	-5.76	-6.08	-1.77	-1.34	-5.87	-5.95

7.2 Uncertainties on jet reconstruction

The reconstruction of the jet energy is affected in a twofold way, first by the uncertainty on the total jet energy scale (JES) and secondly, by the uncertainty on the jet energy resolution (JER). Both uncertainties change the energy of each individual jet. Beside the possible difference in the event selection a further consequence of this change of the event kinematics is the need to recalculate E_T^{miss}. Both uncertainties were derived following the recommendations from the ATLAS jet and E_T^{miss} performance group and are described in the following section.

7.2.1 Jet energy scale uncertainty

As described in Section 4.4.2 the jet energy is calibrated by comparing the total measured energy with the true energy of the particles that form the jet. This true energy can be obtained either from MC simulation or in-situ measurements based on data. The uncertainty on the jet energy scale is based on a breakdown of 16 individual nuisance parameters [103] that are each varied up and down independently. They are constituted by

- one component from closeby-jets obtained as a function of ΔR to the closest jet with $p_{\mathrm{T}} > 7\,\mathrm{GeV}$ [104],
- two components from flavour composition and flavour response accounting for the different energy response for quark and gluon jets [105],
- one component from b-jets that is applied to jets matched to a B hadron,
- six components for covering uncertainties of in-situ measurements. Similar to the b-tagging uncertainty they are obtained from diagonalising the covariance matrix of a total set of 64 uncertainty components separating out the five eigenvectors with the dominant contribution and combining the others into a sixth component. Furthermore there is
- one component for high energetic jets with $p_{\mathrm{T}} > 1\,\mathrm{TeV}$,
- two components from the pile-up offset correction, one for the number of primary vertices N_{PV} and one for the average number of interactions $< \mu >$,
- one component for the non-closure of the calibration between different Monte Carlo productions and
- two components from the dijet η-intercalibration technique.

All components depend on the jet p_{T} and η. As an example, Figure 7.2 shows the p_{T} dependence for a fixed value of $\eta = 2.0$ and the η dependence for a fixed value of $p_{\mathrm{T}} = 25\,\mathrm{GeV}$.

All the different components are propagated separately to a final cross section and summed in quadrature and symmetrised to obtain a combined JES uncertainty which is 4.2 % in the electron channel and 4.9 % in the muon channel.

7.2.2 Jet energy resolution uncertainty

The uncertainty on the jet energy resolution is estimated by over-smearing the jet energy in MC [106]. For this purpose Equation 5.1 in Section 5.2.2 is modified by including the JER uncertainty from data Δ_{res} into the smearing factor:

$$\text{smearing factor} = \sqrt{(\mathrm{res}_{\mathrm{data}} + \Delta_{\mathrm{res}})^2 - (\mathrm{res}_{\mathrm{data}})^2} \tag{7.2}$$

The resulting uncertainties are 0.99 % in the electron channel and 1.85 % in the muon channel.

Table 7.3: Summary of the relative systematic uncertainties on the JES (in %). The uncertainty is decomposed into 16 nuisance parameters that are summed in quadrature to form the combined JES uncertainty. The up and down variations are represented by the arrows ↑ and ↓.

	electron channel				muon channel			
Systematic	$n_{2b,fit,e}$	$\epsilon_{2b,e}$	C_e	σ_e	$n_{2b,fit,\mu}$	$\epsilon_{2b,\mu}$	C_μ	σ_μ
closeby jets ↑	+0.25	-0.81	+3.24	-2.10	+0.18	-1.07	+2.85	-1.54
closeby jets ↓	-0.82	+0.97	-3.51	+1.80	+0.11	+0.76	-2.71	+2.13
b-jets ↑	+0.72	-1.15	+3.89	-1.92	+0.33	-1.16	+4.46	-2.82
b-jets ↓	-1.02	+1.05	-4.56	+2.64	-0.17	+1.16	-4.17	+2.97
flav. composition ↑	-0.12	-	-0.07	-0.05	+0.23	+0.04	-	+0.20
flav. composition ↓	-0.03	+0.01	+0.03	-0.07	-0.24	-0.02	+0.04	-0.26
flav. response ↑	-0.15	-	-0.04	-0.11	+0.05	-0.01	-	+0.06
flav. response ↓	-0.23	-	+0.01	-0.25	-0.04	+0.01	+0.04	-0.09
NP 1 ↑	-0.77	+0.99	-3.73	+2.06	+0.20	+1.00	-3.41	+2.71
NP 1 ↓	-	-0.87	+3.13	-2.19	+0.19	-0.95	+3.57	-2.34
NP 2 ↑	-0.15	-0.45	+1.92	-1.59	-0.06	-0.61	+2.41	-1.81
NP 2 ↓	-0.60	+0.76	-2.66	+1.35	+0.45	+0.62	-2.07	+1.94
NP 3 ↑	-0.38	+0.39	-0.69	-0.07	+0.15	+0.23	-0.57	+0.50
NP 3 ↓	-0.04	-0.09	+0.55	-0.50	+0.13	-0.08	+0.63	-0.41
NP 4 ↑	-0.22	-0.05	+0.40	-0.57	-	-0.13	+0.41	-0.28
NP 4↓	-0.32	+0.21	-0.46	-0.07	+0.09	+0.09	-0.30	+0.30
NP 5 ↑	+0.03	+0.06	+0.24	-0.27	-0.07	-0.04	+0.15	-0.17
NP 5↓	-0.25	+0.15	-0.21	-0.19	+0.04	+0.06	-0.17	+0.15
NP 6↑	-0.01	-0.14	+0.73	-0.59	+0.22	-0.20	+0.87	-0.44
NP 6↓	-0.40	+0.37	-0.99	+0.23	+0.19	+0.28	-0.79	+0.70
high-pt↑	-0.05	+0.02	+0.13	-0.19	-0.02	-0.03	+0.21	-0.20
high-pt↓	-0.13	+0.11	-0.18	-0.05	+0.14	+0.11	-0.08	+0.10
non closure MC11↑	-0.17	+0.03	+0.13	-0.33	-0.16	-0.02	+0.22	-0.36
non closure MC11↓	-0.24	+0.10	-0.20	-0.14	+0.23	+0.12	-0.09	+0.19
NPV offset term↑	-0.17	-	-	-0.17	+0.13	-	-	+0.13
NPV offset term↓	-0.12	+0.30	-0.15	-0.27	-0.26	+0.05	+0.08	-0.39
mu offset term↑	-0.17	-	-	-0.17	-	-	-	-
mu offset term↓	+0.81	+0.58	-0.62	+0.85	+0.08	+0.06	-0.49	+0.51
eta int.cal. total↑	+0.32	-0.80	+1.81	-0.66	+0.12	-0.65	+2.03	-1.23
eta int.cal. total↓	-0.71	+0.50	-2.23	+1.05	+0.22	+0.69	-1.98	+1.55
eta int.cal. model↑	-	-	-	-	-	-	-	-
eta int.cal. model↓	-	-	-	-	-	-	-	-

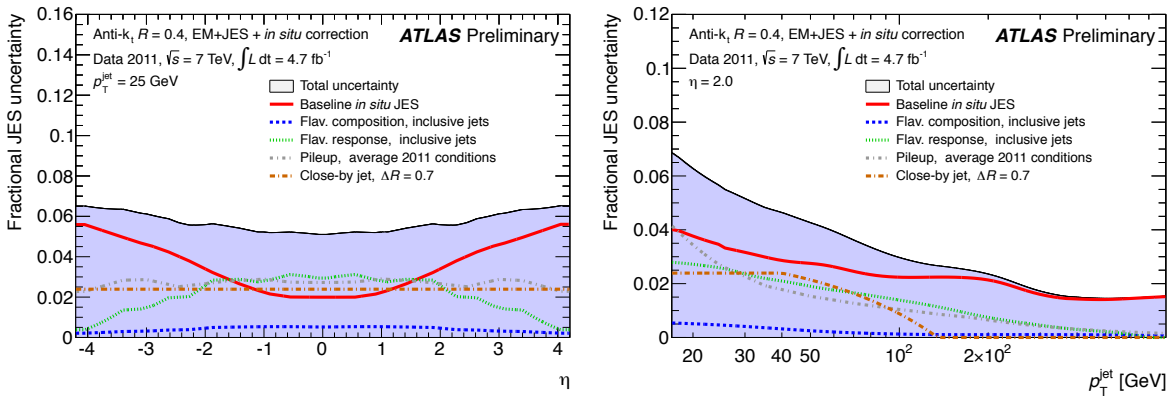

(a) η dependence

(b) p_T dependence

Figure 7.2: Fractional JES uncertainty dependence on (a) η for a fixed value of $p_T = 25\,\text{GeV}$ and on (b) p_T for a fixed value of $\eta = 2.0$. The different components as well as the combined uncertainty are shown [103].

7.3 Fit template uncertainties

The presented measurement uses a fit to estimate the signal yield in the final event selection. For this purpose the fit makes use of the flavour sensitive variable $\ln(P_b/P_c)$. The analysis therefore relies on a good description of these templates from MC. This section summarises the uncertainties that are assigned to the fit templates.

7.3.1 Shape uncertainty on b-jet template

It has been shown in Section 6.2.3 that for the ALPGEN MC signal the charged particle multiplicity from b-hadron decays is corrected to emulate the expectations from EvtGen. This correction is based on event weights that are intended to modify the fit template shape. This correction does not account for mismodelling from fragmentation and hadronisation, though. Therefore an alternative and data-driven template reweighting has been applied in the $t\bar{t}$ control region (see Section 6.2.3) that is derived from the difference between data and uncorrected MC in the $\ln(P_b/P_c)$ distribution. Figure 7.3 shows this ratio and for comparison the correction obtained by applying the EvtGen reweighting. The reweighting is applied per jet and a third order polynomial fit has been performed to the data/MC ratio to provide reweighting scale factors in the $\ln(P_b/P_c)$ range (2, 9). Jets outside this range have been assigned a weight of one. The resulting fractional uncertainty is 5.38 % in the electron channel and 4.38 % in the muon channel.

As a cross check the fit was repeated with b-jet templates derived from MC simulation obtained with SHERPA without applying the EvtGen reweighting. The observed deviations from the nominal fit result were covered by the uncertainty that is quoted here.

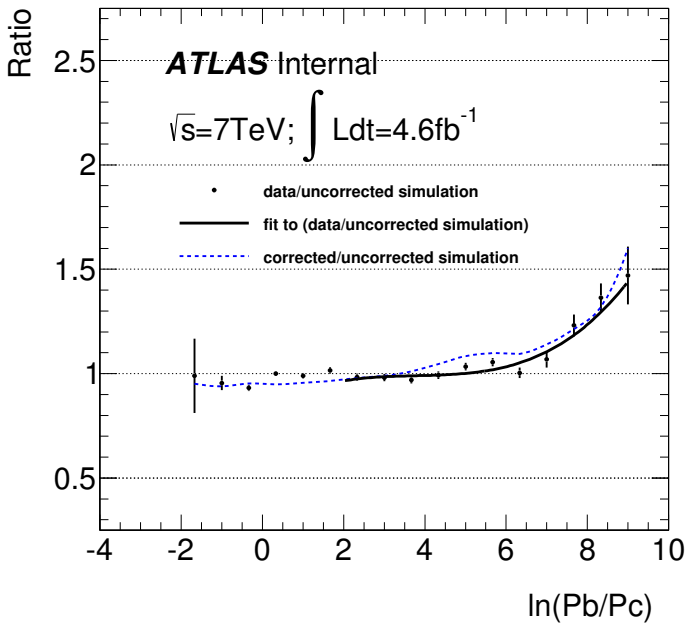

Figure 7.3: Comparison between the weighting schemes obtained from the data-driven approach in the $t\bar{t}$ control region (dots) and the EvtGen correction (dashed line). The solid line shows a fit to the dots to provide a continuous reweighting in the range (2, 9). [12]

7.3.2 Template shape uncertainty for charm and light jets

To estimate the impact of mismodelling in the non-bb templates, the $\ln(P_b/P_c)$ distribution for individual jets has been generated by using SHERPA samples. For charm jets a SHERPA simulation with massive b- and c- quarks has been generated and filtered for events which contain at least one weakly decaying heavy flavour hadron. For light jets this sample does not provide enough events to generate a usable reweighting and hence a SHERPA Z+jets sample with massless heavy flavour quarks was used.

Figure 7.4 shows the $\ln(P_b/P_c)$ ratio between ALPGEN and SHERPA for (a) charm-jets and for (b) light jets. The ratios are fitted with a second order polynomial in the range $(-1, 3)$ and an event weight is obtained by multiplying the jet weights of all charm/light jets in the event. With this procedure an uncertainty of 0.61 % (0.64 %) for charm jets and 0.66 % (0.98 %) for light jets in the electron (muon) channel has been found.

7.3.3 Template flavour composition uncertainty

Beside the systematic uncertainty on the template shape, a further systematic uncertainty is assigned that accounts for the flavour composition of the non-bb fit template. This template is merged from the templates with *bc*, *bl*, *cc*, *cl* and *ll* truth flavour of the leading two tagged jets. The relative fraction of *bc* and *bl* has been measured be to larger than the MC prediction by a factor of 1.37 ± 0.05 (see Section 6.2.4). This scale factor has been obtained after selecting the Z boson with at least two jets of which exactly one is b-tagged. For comparison, a direct

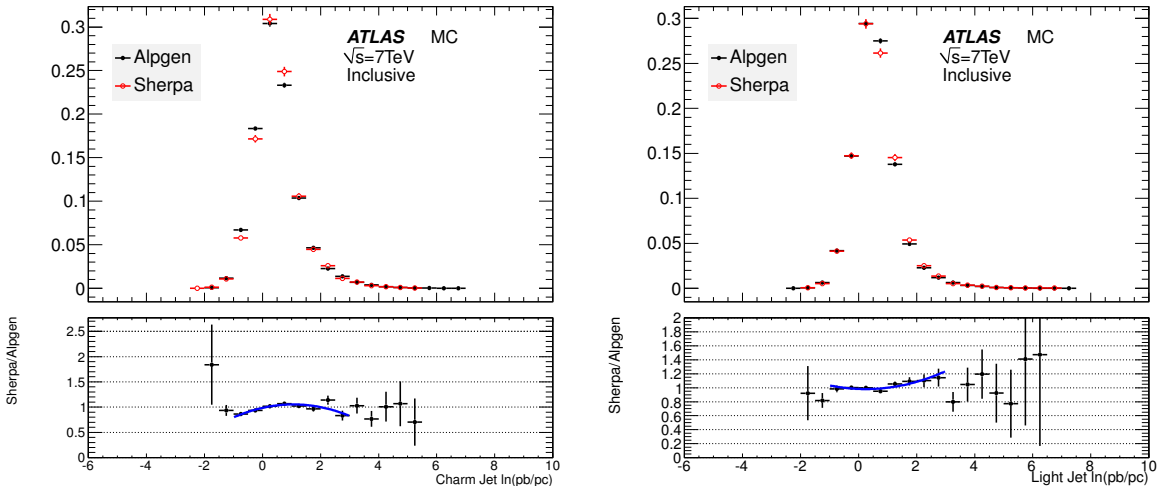

(a) Charm jets (b) Light jets

Figure 7.4: The ratio between the template predictions from SHERPA and ALPGEN for (a) charm jets and (b) light jets. The ratio has been fitted by a third order polynomial in the range $(-1, 3)$ that is used to reweight the ALPGEN templates as a systematic variation [63].

fit after the $Z + 1b$ selection gives a scale factor of 1.22. To account for this difference, an uncertainty of 15 % has been assigned to the scale factor. The uncertainty is propagated to the cross section measurement and results in an uncertainty of 2.2 % in the electron channel and 1.6 % in the muon channel.

An independent variation of 15 % on the charm and light fractions in the templates has been assigned. These variations cover the spread on the scale factor. An uncertainty on the cross section of 1.1 % (1.2 %) was found by varying the charm fraction in the electron (muon) channel. For light jets an uncertainty of 0.4 % (0.5 %) was found in the electron (muon) channel.

7.3.4 Statistical uncertainty on the template shape

So far, only the statistical uncertainty of the data distribution is included into the fit procedure. However, the available MC simulation to generate the templates is not infinite and hence statistical fluctuations in the templates need to be accounted for. To evaluate this contribution, an ensemble test has been performed where each bin in each template is shifted according to a random Gaussian function defined by the average bin content and the statistical uncertainty in the bin. A number of 5000 fits with new randomly varied templates have been performed on the data distribution.

The corresponding fit results are described by a Gaussian function with the mean value around the nominal fit result. The standard deviation of the Gaussian is assigned as systematic uncertainty. The fractional systematic uncertainty is 2.1 % (1.9 %) in the electron (muon) channel.

7.4 Background uncertainties

7.4.1 Normalisation of background samples

The fit to discriminate between signal events and events with Z+light jets as it is described in Section 6.2 has no sensitivity to distinguish further backgrounds like $t\bar{t}$, single-top and di-bosonic events. As a consequence, in addition to the shape, also the normalisations of these backgrounds are obtained from theoretical predictions. To give a conservative estimate on the theoretical uncertainties on these predictions each component is varied independently by ±10 % as recommended in Ref. [107]. The dominating uncertainty is from the $t\bar{t}$ normalisation and translates into 3.6 % in the electron channel and 3.1 % in the muon channel. As a further cross-check the template normalisation has also been predicted from another $t\bar{t}$ MC sample simulated with POWHEG +PYTHIA finding that the observed relative difference of about 4 % to the nominal $t\bar{t}$ sample is already covered by the assigned uncertainty.

For the diboson normalisation the effect is 0.4 % and for the single-top it is negligible.

For the multijet background contamination an uncertainty of 2 % has been assigned in both channels. Although estimations of this background are consistent with zero, the uncertainty obtained from these estimations is set as an upper limit.

7.4.2 Shape of the $t\bar{t}$ template

In order to assess the uncertainty on the shape of the $t\bar{t}$ template, it has been substituted by an alternative $t\bar{t}$ sample generated with POWHEG +PYTHIA. To disentangle the effect of the shape from the normalisation the template has been normalized to the default $t\bar{t}$ prediction. Figure 7.5 shows a comparison of the template shape predicted by the two MC samples. For comparison, the uncertainty on the normalisation of the $t\bar{t}$ background is depicted by the green error band. The shape difference is well within the normalisation uncertainty band.

The uncertainty on the fit result and therefore on the cross section was found to be 3.2 % in the electron channel and 2.5 % in the muon channel. The uncertainty on the shape of the diboson and on the single-top background template are assumed to be negligible.

7.5 Systematic uncertainties from multiple parton interactions

A final state signature with a Z^0 boson and two b-jets can also originate from double-parton interactions (DPI). This contribution can be estimated in hadron collisions for a composite signature $(X + Y)$ by the effective area parameter σ_{eff} which has been measured in [108] for W+2jets events as:

$$\sigma_{\text{eff}} = 15 \pm 3^{+5}_{-3}\text{mb} \tag{7.3}$$

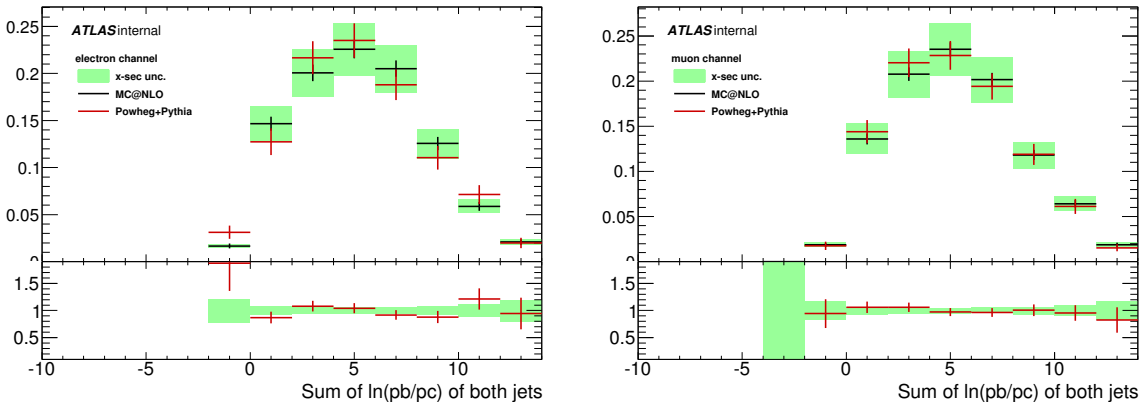

(a) Electron channel (b) Muon channel

Figure 7.5: Comparison of the ttbar template shape for the default MC@NLO sample and the POWHEG +PYTHIA sample. The left plot shows the fit template for the electron channel and the right plot for the muon channel. The green band shows the uncertainty on the normalisation.

This parameter is expected to be almost independent of the underlying process and kinematic phase space. The contribution from DPI can be obtained by (see Ref. [108]):

$$\sigma^{\mathrm{DPI}}(X+Y) = \frac{\sigma_X + \sigma_Y}{\sigma_{\mathrm{eff}}} \tag{7.4}$$

Both cross sections $\sigma_X = \sigma_Z \approx 0.5\,\mathrm{nb}$ and $\sigma_Y = \sigma_{b\bar{b}} \approx 22\,\mathrm{nb}$ have been measured at ATLAS [109, 110]. However, the phase space definitions are slightly different: the invariant dilepton mass window for the selection of the Z boson is $66\,\mathrm{GeV} < m_{ll} < 116\,\mathrm{GeV}$ and jets are restricted to $|y| < 2.1$ and $p_{\mathrm{T}} > 40\,\mathrm{GeV}$. Furthermore, no overlap removal between jets and leptons is applied. The analysis has been repeated with adjusted phase space definitions to obtain the relative contribution from DPI events with a slightly larger cross section compared to the nominal phase space selection: $\sigma_{ee} \approx 0.51\,\mathrm{pb}$ and $\sigma_{\mu\mu} \approx 0.55\,\mathrm{pb}$. The estimated uncertainty is below two per mille and can therefore be neglected.

Since it is now known a priori that the extrapolation in the analysis phase space, especially to the lower b-jet p_{T} selection, is valid, the MPI contribution has also been estimated from ALPGEN MC by evaluating the truth event information (see [63] for details). These events have been reweighted conservatively by ±50 % and the resulting uncertainty is between 0.25 and 0.3 %.

7.6 Systematic uncertainty from gluon splitting contribution

The systematic uncertainty on the prediction of the number of events resulting from gluon splitting is obtained by scaling their contribution by ±100 %. Events where at least one b-quark originates from gluon splitting are identified on truth level by counting the number of b-hadrons

within $\Delta R < 0.3$ around the reconstructed b-jet. When there are at least two b-hadrons matched, the jet is assumed to originate from gluon splitting. For comparison, SHERPA predicts around half the number of double matched b-jets which is conservatively covered by the variation that is made. The symmetrised uncertainty is about 1.4 % in the electron channel and 1.6 % in the muon channel.

7.7 Uncertainty on the heavy flavour overlap procedure

To remove the heavy flavour overlap between the Z+jets and the $Z + b\bar{b}$ sample, events with $\Delta R(bb) < 0.4$ were taken from the parton shower (the Z+jets sample) and events with $\Delta R(bb) > 0.4$ were taken from the matrix element calculation i.e. the $Z + b\bar{b}$ sample (see Section 5.2.1). To assess an uncertainty on this assumption, a different method has been used: only events from the matrix element calculation (see blue line in Figure 5.2a) were used. The uncertainty obtained by comparing the two approaches is 1.2 % in the electron channel and 1 % in the muon channel.

Since it is not a priori known that the matrix element calculation yields the best description one would also try to use only events from the gluon splitting, but there are not enough events available to produce reasonable templates.

7.8 Lepton measurement uncertainties

The lepton uncertainties can be divided into two classes: first those that change scale factors and hence event weights, and secondly those that change the kinematic event topology and therefore lead to a different event selection. The first class includes the lepton reconstruction and identification efficiencies (see Section 5.2.2) and the trigger efficiencies (see Section 5.2.2). Both are varied up and down independently by $\pm 1\sigma$. In the electron channel, the reconstruction and identification efficiency are shifted simultaneously. The trigger efficiency scale factors are shifted simultaneously for both leptons. The second class contains lepton energy scale and energy resolution uncertainties. The energy of both leptons per event is shifted up and down by $\pm 1\sigma$ simultaneously. In a similar way the uncertainty on the lepton energy resolution is propagated to the cross sections. For the muon case the shift in the energy smearing is applied separately to the inner detector measurement (ID) and to the momentum from the muon spectrometer (MS). The resulting uncertainties are summarised in Table 7.4 and 7.5 for the electron channel and the muon channel, respectively. They are summed in quadrature for both channels. The differences between up and down variation are statistical fluctuations and hence the quoted total uncertainty is symmetrised by taking the average between up and down variations.

7.9 Uncertainty on missing transverse energy

The missing transverse energy is calculated from several terms each corresponding to a class of physics objects, e.g. a term for muons, a term for jets etc.(see Section). Energy scale and re-

Table 7.4: Fractional lepton systematic uncertainties in the electron channel. All numbers are in %. The up and down variations are represented by the arrows ↑ and ↓.

Systematic	$n_{2b,fit}$	ϵ_{2b}	C	σ
efficiency ↑	-1.79	-0.03	+0.76	-1.01
efficiency ↓	+1.72	+0.03	-0.58	+1.12
trigger ↑	-0.18	+0.02	+0.54	-0.74
trigger ↓	+0.18	-0.02	-0.54	+0.74
energy scale ↑	+0.15	-	-	+0.15
energy scale ↓	-0.15	-	-	-0.15
energy resolution ↑	-0.14	-0.03	+0.01	-0.12
energy resolution ↓	+0.15	+0.03	-0.01	+0.13
total (symmetrised)				±1.38

Table 7.5: Fractional lepton systematic uncertainties in the muon channel. All numbers are in %. The up and down variations are represented by the arrows ↑ and ↓.

Systematic	$n_{2b,fit}$	ϵ_{2b}	C	σ
efficiency ↑	-0.24	-	+0.69	-0.93
efficiency ↓	+0.24	-	-0.69	+0.94
trigger ↑	-0.18	-	+0.49	-0.67
trigger ↓	+0.18	-	-0.49	+0.68
energy scale ↑	-0.01	-0.01	+0.01	-0.01
energy scale ↓	-0.07	+0.03	-0.04	-0.06
energy resolution (MS) ↑	+0.02	-0.05	-0.03	+0.09
energy resolution (MS) ↓	+0.05	-0.04	+0.03	+0.06
energy resolution (ID) ↑	-0.08	+0.01	-	-0.10
energy resolution (ID) ↓	-	+0.01	+0.01	-0.01
total (symmetrised)				±1.16

solution uncertainties on leptons and jets are propagated consistently to the corresponding E_T^{miss} terms and hence to the total E_T^{miss}. However, there are terms that do not derive directly from such objects like the soft recoil terms $E_T^{\text{miss, softjets}}$ and $E_T^{\text{miss, CellsOut}}$. Their resolution and scale are varied simultaneously for both terms and the uncertainties are propagated to the analysis chain. The results are summarised in Table 7.6.

The terms for photons and τ leptons do not contribute significantly and are not further considered (see also Figure 4.4 on page 38).

Table 7.6: Systematic uncertainties in % obtained by the E_T^{miss} soft terms variations in the electron and in the muon channel. The up and down variations are represented by the arrows ↑ and ↓.

	electron channel				muon channel			
Systematic	$n_{2b,fit,e}$	$\epsilon_{2b,e}$	C_e	σ_e	$n_{2b,fit,\mu}$	$\epsilon_{2b,\mu}$	C_μ	σ_μ
Reso ↑	-0.10	+0.01	-0.04	-0.07	-0.17	-0.03	-0.01	-0.13
Reso ↓	+0.27	+0.06	+0.02	+0.18	-0.02	-0.02	+0.01	-0.01
Scale ↑	+0.42	-0.01	-0.12	+0.55	+0.21	-0.03	-0.05	+0.29
Scale ↓	-0.34	+0.04	+0.09	-0.47	-0.24	+0.01	+0.04	-0.29

7.10 Luminosity uncertainty

An uncertainty of 1.8 % on the total integrated luminosity is assumed based on measurements described in [22].

7.11 Combination

A summary of all systematic uncertainties is shown in Table 7.7. It is assumed that small differences between up and down variation are originating from statistical fluctuations. Hence they are symmetrised by taking the average.

The dominating contributions arise from the uncertainty on the b-tagging efficiency, the jet energy scale, the $t\bar{t}$ background normalisation and the uncertainty on the b-jet template shape. The total systematic uncertainty is obtained by summing all individual components in quadrature.

Table 7.7: Summary of fractional systematic uncertainties in %. Up- and down-variations are symmetrized by taking the average.

Systematic	Electron channel	Muon channel	Combination
b-jet tagging eff.	6.2 %	6.1 %	6.2 %
c-jet mistag rate	< 0.1 %	< 0.1 %	< 0.1 %
Light-jet mistag rate	2.4 %	2.3 %	2.4 %
JES	4.2 %	5.0 %	4.6 %
JER	1.0 %	1.9 %	1.4 %
b-jet template shape	5.4 %	4.4 %	4.8 %
c-jet template shape	0.6 %	0.6 %	0.6 %
Light-jet template shape	0.7 %	1.0 %	0.9 %
Flavour composition	2.5 %	2.1 %	2.3 %
Background normalisation	4.1 %	3.7 %	3.9 %
$t\bar{t}$ modelling	3.2 %	2.5 %	2.9 %
MPI	0.3 %	0.3 %	0.3 %
Gluon splitting	1.4 %	1.6 %	1.5 %
Heavy flavour overlap removal	1.2 %	1.0 %	1.1 %
MC statistics	2.1 %	1.9 %	2.0 %
Lepton scale and resolution	1.4 %	1.2 %	1.4 %
E_T^{miss} soft terms	0.5 %	0.3 %	0.4 %
Luminosity	1.8 %	1.8 %	1.8 %
Total	11.8 %	11.3 %	11.5 %

CHAPTER 8

Results and conclusions

The combined result of the cross section measurement is:

$$\sigma(Z + b\bar{b}) = 0.522 \pm 0.025(\text{stat.}) \pm 0.065(\text{syst.}) \tag{8.1}$$

Table 8.1 and Figure 8.1 summarise the theoretical predictions in leading order (LO) and next-to-leading order (NLO) and compare them to the result of this measurement.

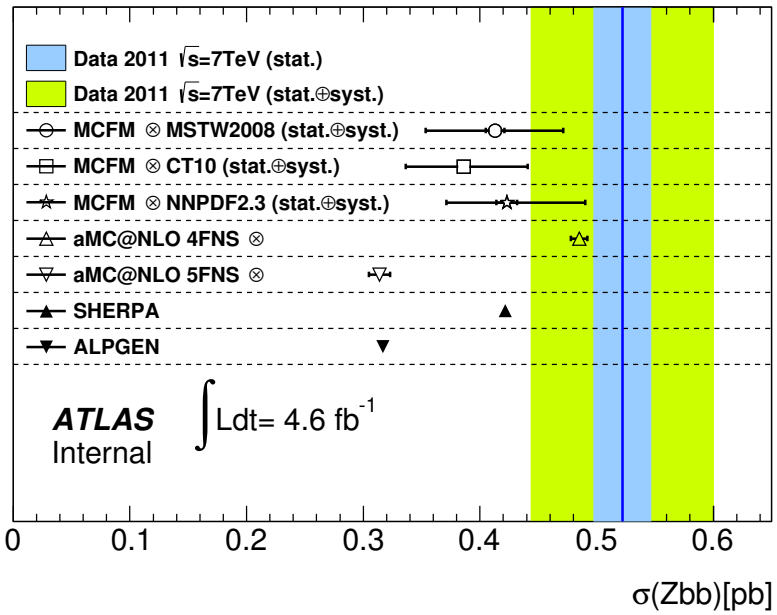

Figure 8.1: Measured cross sections in data compared to theoretical predictions in LO and NLO. The uncertainty prediction for aMC@NLO, SHERPA and ALPGEN are only statistical.

The LO prediction from ALPGEN (and also the quasi-LO prediction from aMC@NLO) strongly underestimate the measured result. Nevertheless, only statistical uncertainties were

Table 8.1: Measured cross sections in data compared to theoretical predictions in LO and NLO. The results measured by CMS are obtained with a tighter phase space definition as described in the text. The first quoted error refers to the statistical and the second to the systematic uncertainty.

	$\sigma(Zbb)$ in pb
Data measurements	
combined	$0.522 \pm 0.025 \pm 0.065$
electron channel	$0.483 \pm 0.036 \pm 0.052$
muon channel	$0.566 \pm 0.035 \pm 0.064$
Theory predictions	
MCFM, MSTW2008	$0.413 \pm 0.008\ ^{+0.057}_{-0.058}$
MCFM, CT10	$0.386 \pm 0.004\ ^{+0.055}_{-0.050}$
MCFM, NNPDF23	$0.423 \pm 0.009\ ^{+0.067}_{-0.051}$
aMC@NLO Zbb, MSTW2008	0.485 ± 0.007
aMC@NLO Zj, MSTW2008	0.314 ± 0.009
SHERPA, CT10	0.422 ± 0.002
ALPGEN, CTEQ6L1	0.317 ± 0.002
CMS measurements (in different phasespace)	
electron channel	$0.320 \pm 0.020 \pm 0.060$
muon channel	$0.380 \pm 0.020 \pm 0.070$
combined	$0.360 \pm 0.010 \pm 0.070$

calculated for these predictions and it must be assumed that such LO calculations have significant scale uncertainties. Furthermore, a theoretical scale-factor of 1.67 to go from LO to NLO has been calculated in [40] which is in good agreement with the observed difference. The NLO prediction from MCFM is within one standard deviation compatible to the measurement. The prediction from SHERPA gives similar results. However, there seems to be a consistent underestimate in the cross section by all theoretical predictions. The best description of the measurement is obtained from the aMC@NLO prediction which includes massive b-quarks and spin correlations between the final state leptons. On the other hand, no significant improvement of predictions in the five-flavour-scheme could be observed. This is in agreement with theoretical predictions in [41].

A similar measurement on the $Z + b\bar{b}$ cross section has been performed by the CMS experiment [111] with a tighter event selection: jets are required to have $p_{\mathrm{T}} > 25\,\mathrm{GeV}$ with $|\eta| < 2.1$ and leptons are within $|\eta| < 2.4$. Therefore it is expected that the measurement from CMS results in a lower cross section. To allow a comparison between the experiments the analysis has been repeated with adjusted phase space definition and a combined cross section of $\sigma(Zbb) = (0.302 \pm 0.031)\,\mathrm{pb}$ has been obtained. Only statistical uncertainties are quoted

here. Under the assumption that the systematic uncertainties do not decrease significantly in this phase space the measurements between ATLAS and CMS are compatible.

CHAPTER 9

Summary

In this thesis, the measurement of the inclusive production cross section for the production of at least two b-jets in association with a Z-boson has been presented. Both lepton final states for the Z-boson decay have been measured independently but also a combination of both was performed. The fiducial phasespace for this measurement is defined by the following criteria: b-jets are required to have $p_T > 20\,\text{GeV}$ and $|y| < 2.4$. The leptons are selected with $p_T > 20\,\text{GeV}$ and $|\eta| < 2.5$. The centre-of-mass energy is $\sqrt{s} = 7\,\text{TeV}$ and the amount of data corresponds to $4.58\,\text{fb}^{-1}$ taken at the ATLAS detector.

After the selection of $Z + b\bar{b}$ events, a maximum likelihood fit on a flavour sensitive variable has been performed to estimate the signal yield. In addition to the statistical uncertainties a large number of systematic effects have been evaluated. The dominant uncertainty contributions arise from the b-tagging efficiency, the jet energy scale, the modelling of the template shape and the normalisation of the background represented by $t\bar{t}$ and ZZ events.

The measurement has been corrected for detector effects and efficiencies to particle level which makes it possible to compare it to theory predictions in leading and subleading order. Predictions in LO underestimate the cross section in an expected way. NLO predictions have been calculated using MCFM and aMC@NLO. Even though both are compatible to the measurement, the prediction from aMC@NLO, which treats the b-quarks as massive and considers spin correlations of the final-state leptons, describes the data better. The prediction based on the four-flavour scheme was found to describe the data better than the five-flavor scheme.

APPENDIX A

Monte Carlo samples

Table A.1: Detailed information on the Monte Carlo samples that are used in this thesis. The k-factor is used to transform the cross section prediction to NLO. For the SHERPA samples that are used for systematic studies no cross section is quoted since they are used only for comparison of template shapes and therefore the total normalisation is irrelevant.

Process	Generator	σ [pb]	k-factor	N_{events}	comment
$Z + b\bar{b}$ ($\rightarrow ee$) + jets	ALPGEN	10.3	1.25	660k	up to 3 additional partons
$Z + b\bar{b}$ ($\rightarrow \mu\mu$) + jets	ALPGEN	10.3	1.25	655k	up to 3 additional partons
Z ($\rightarrow ee$) + jets	ALPGEN	858.1	1.25	1.07M	up to 5 additional partons
Z ($\rightarrow \mu\mu$) + jets	ALPGEN	857.9	1.25	1.07M	up to 5 additional partons
$t\bar{t}$	MC@NLO	79.01	1.219	15M	no fully hadronic decays
single-top ($\rightarrow e\nu$)	MC@NLO	14.6	1.079	900k	associated W production
single-top ($\rightarrow \mu\nu$)	MC@NLO	14.6	1.079	900k	associated W production
single-top ($\rightarrow e\nu$)	MC@NLO	0.47	1.064	300k	s-channel
single-top ($\rightarrow \mu\nu$)	MC@NLO	0.47	1.064	300k	s-channel
single-top ($\rightarrow e\nu$)	AcerMC	8.06	0.865	1M	t-channel
single-top ($\rightarrow \mu\nu$)	AcerMC	8.06	0.865	1M	t-channel
$ZZ(\rightarrow llqq)$	MC@NLO	0.559	–	25k	
W^+Z	MC@NLO	0.542	–	25k	
W^-Z	MC@NLO	0.294	–	100k	
Z ($\rightarrow ee$) + heavy jets	SHERPA	–	–	1M	for systematic studies
Z ($\rightarrow \mu\mu$) + heavy jets	SHERPA	–	–	1M	for systematic studies
Z ($\rightarrow ee$)	SHERPA	–	–	1M	for systematic studies
Z ($\rightarrow \mu\mu$)	SHERPA	–	–	1M	for systematic studies
$t\bar{t}$	POWHEG	80.85	1.191	500k	for systematic studies

APPENDIX B

Fit results and templates for other combinations

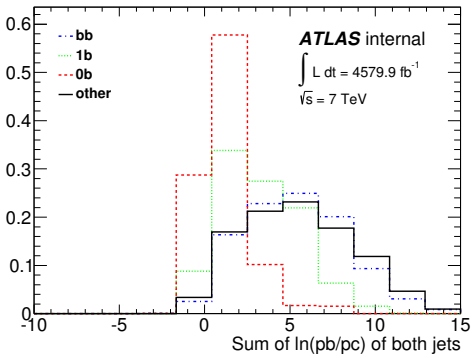

(a) $Z \to ee$ channel, $\ln(P_b/P_c)$

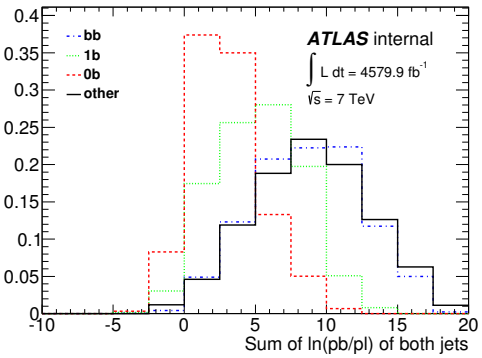

(b) $Z \to ee$ channel, $\ln(P_b/P_l)$

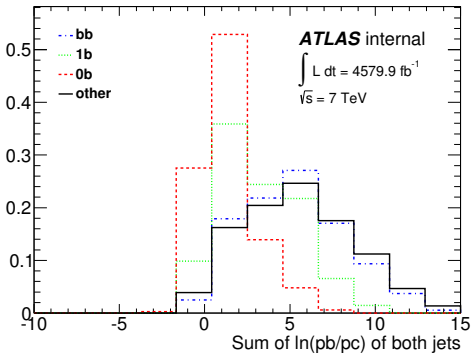

(c) $Z \to \mu\mu$ channel, $\ln(P_b/P_c)$

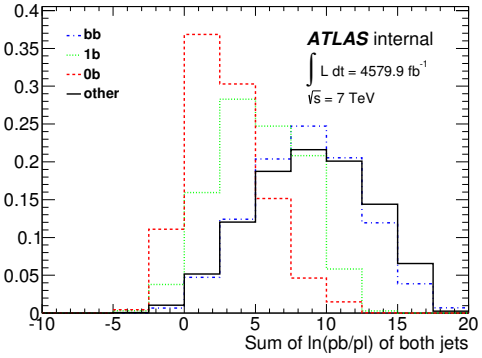

(d) $Z \to \mu\mu$ channel, $\ln(P_b/P_l)$

Figure B.1: Fit templates for Combination B

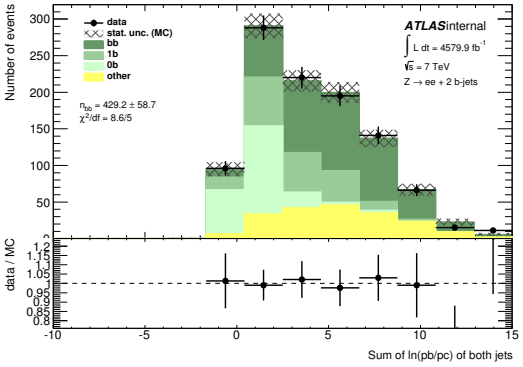

(a) $Z \to ee$ channel, $\ln(P_b/P_c)$

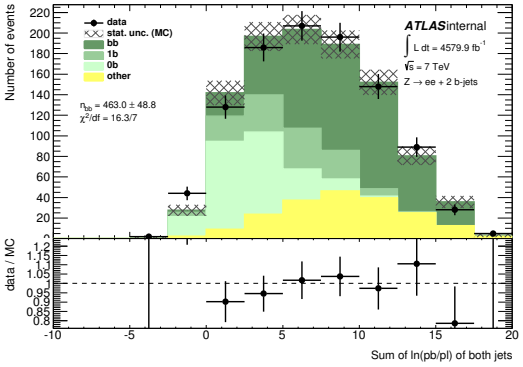

(b) $Z \to ee$ channel, $\ln(P_b/P_l)$

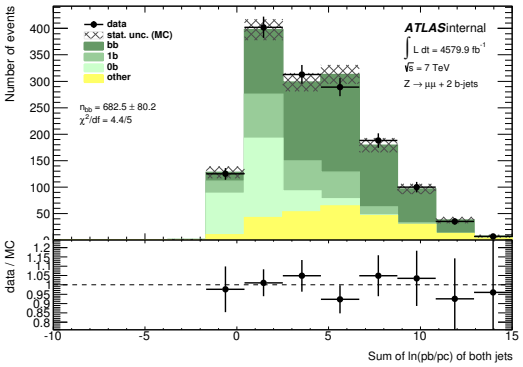

(c) $Z \to \mu\mu$ channel, $\ln(P_b/P_c)$

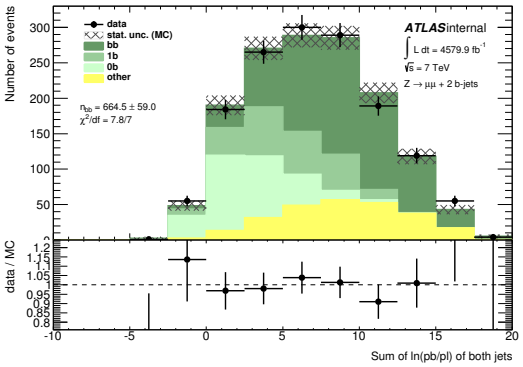

(d) $Z \to \mu\mu$ channel, $\ln(P_b/P_l)$

Figure B.2: Fit results for Combination B

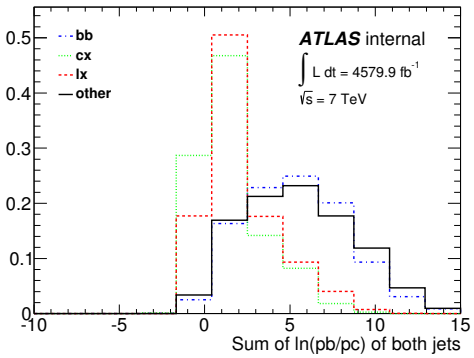

(a) $Z \to ee$ channel, $\ln(P_b/P_c)$

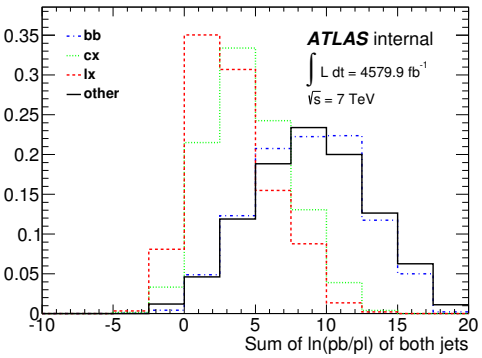

(b) $Z \to ee$ channel, $\ln(P_b/P_l)$

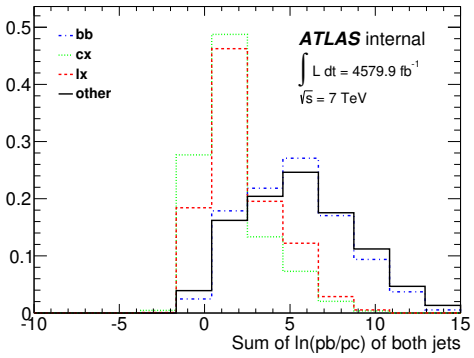

(c) $Z \to \mu\mu$ channel, $\ln(P_b/P_c)$

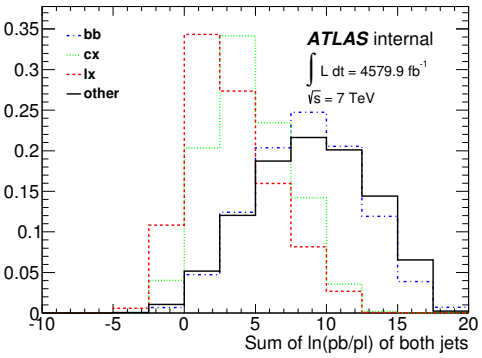

(d) $Z \to \mu\mu$ channel, $\ln(P_b/P_l)$

Figure B.3: Fit templates for Combination C

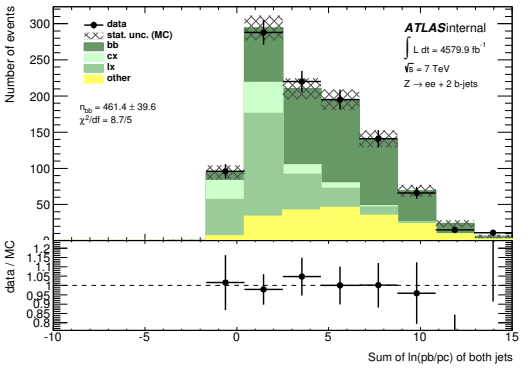

(a) $Z \to ee$ channel, $\ln(P_b/P_c)$

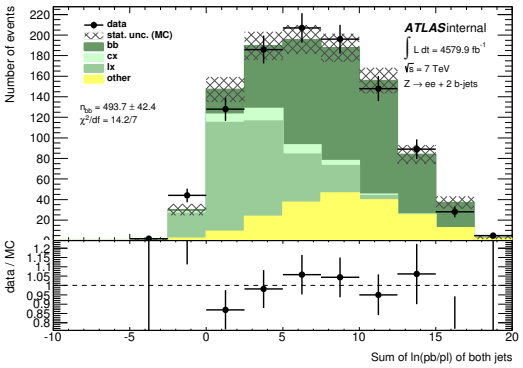

(b) $Z \to ee$ channel, $\ln(P_b/P_l)$

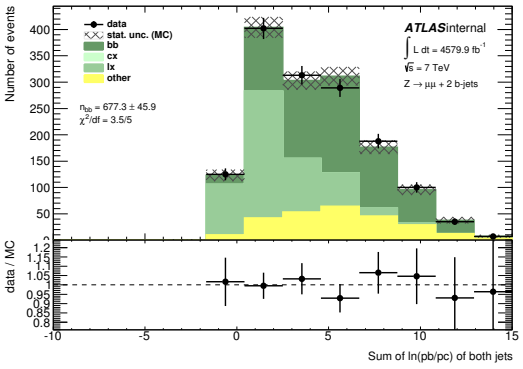

(c) $Z \to \mu\mu$ channel, $\ln(P_b/P_c)$

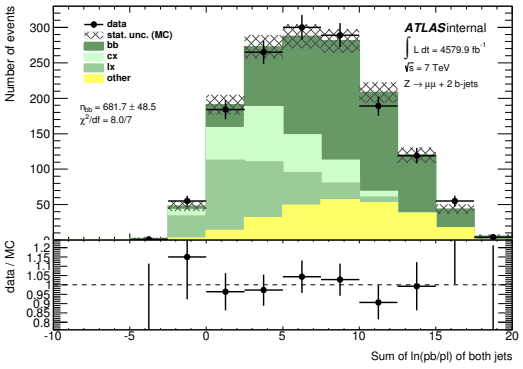

(d) $Z \to \mu\mu$ channel, $\ln(P_b/P_l)$

Figure B.4: Fit results for Combination C

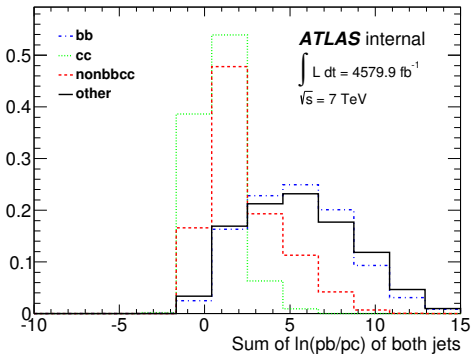

(a) $Z \to ee$ channel, $\ln(P_b/P_c)$

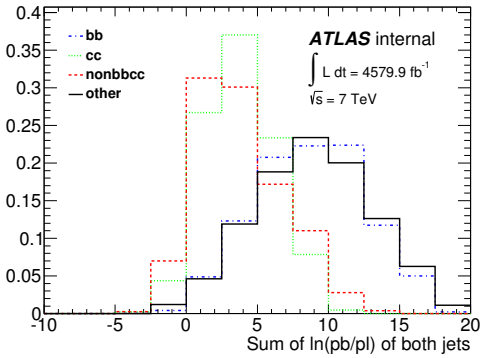

(b) $Z \to ee$ channel, $\ln(P_b/P_l)$

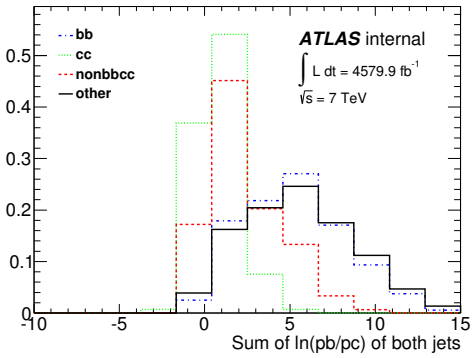

(c) $Z \to \mu\mu$ channel, $\ln(P_b/P_c)$

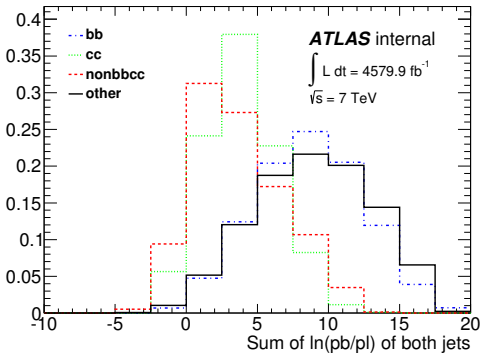

(d) $Z \to \mu\mu$ channel, $\ln(P_b/P_l)$

Figure B.5: Fit templates for Combination D

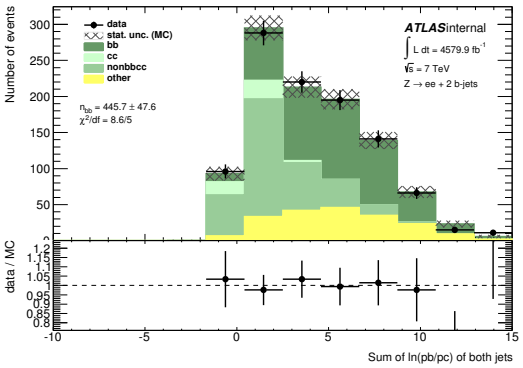

(a) $Z \to ee$ channel, $\ln(P_b/P_c)$

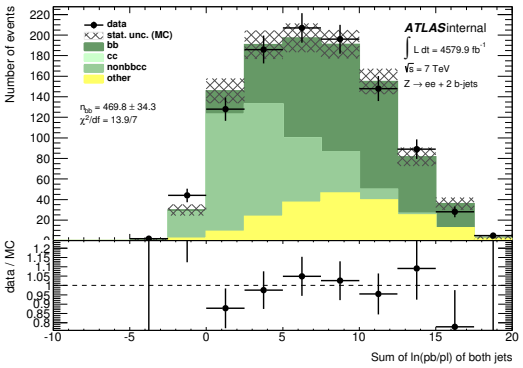

(b) $Z \to ee$ channel, $\ln(P_b/P_l)$

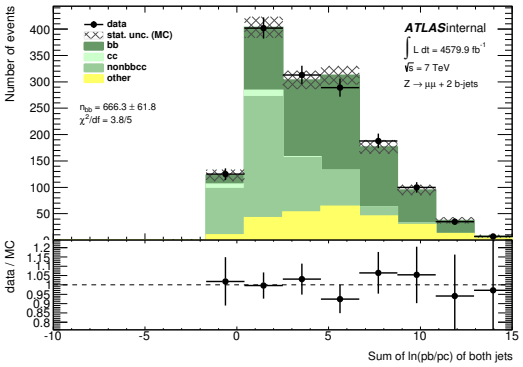

(c) $Z \to \mu\mu$ channel, $\ln(P_b/P_c)$

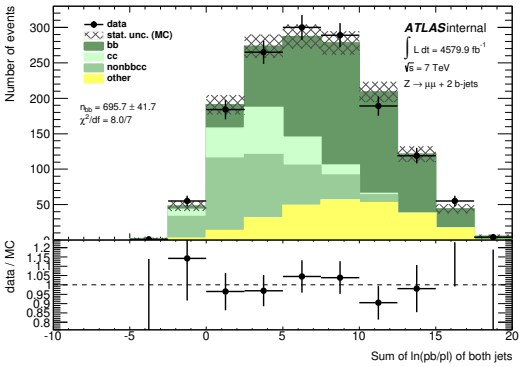

(d) $Z \to \mu\mu$ channel, $\ln(P_b/P_l)$

Figure B.6: Fit results for Combination D

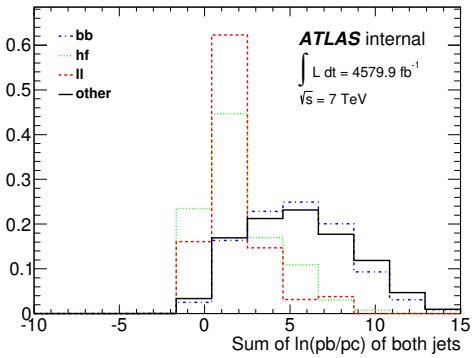

(a) $Z \to ee$ channel, $\ln(P_b/P_c)$

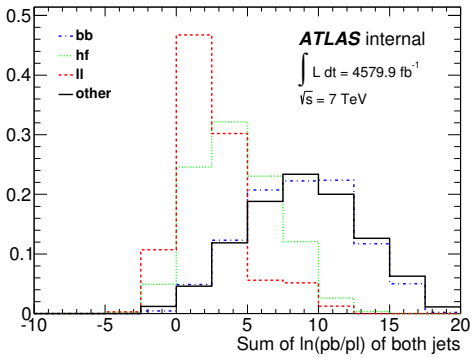

(b) $Z \to ee$ channel, $\ln(P_b/P_l)$

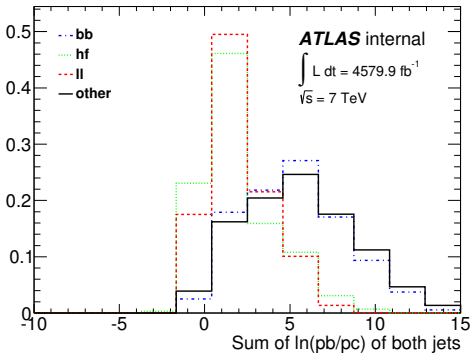

(c) $Z \to \mu\mu$ channel, $\ln(P_b/P_c)$

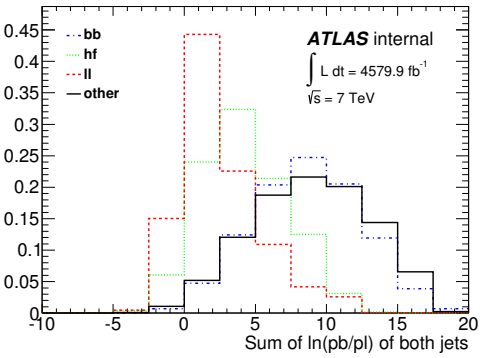

(d) $Z \to \mu\mu$ channel, $\ln(P_b/P_l)$

Figure B.7: Fit templates for Combination E

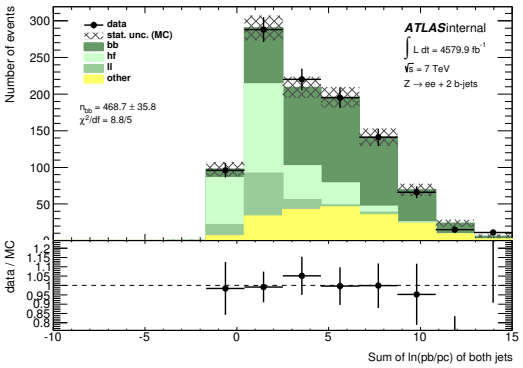

(a) $Z \to ee$ channel, $\ln(P_b/P_c)$

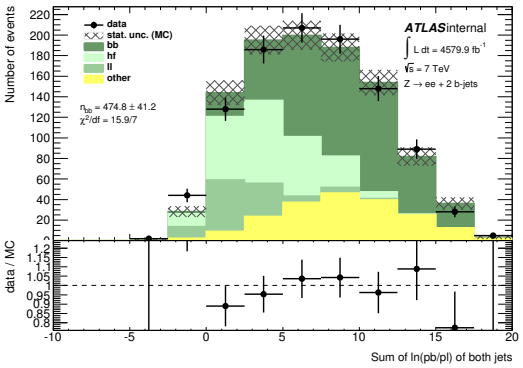

(b) $Z \to ee$ channel, $\ln(P_b/P_l)$

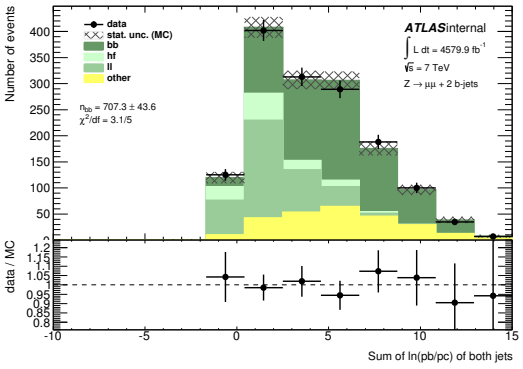

(c) $Z \to \mu\mu$ channel, $\ln(P_b/P_c)$

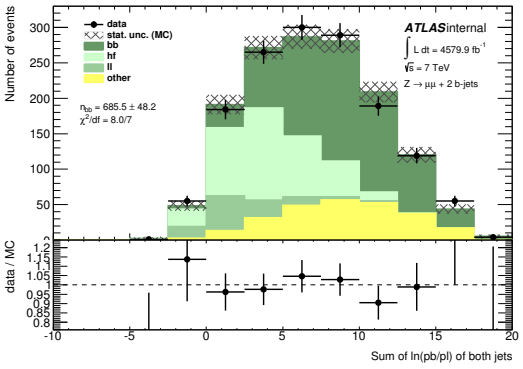

(d) $Z \to \mu\mu$ channel, $\ln(P_b/P_l)$

Figure B.8: Fit results for Combination E

APPENDIX C

Fit validation

C.1 Validation results for alternative fit variable

C.2 Validation of results for combining electron and muon channel

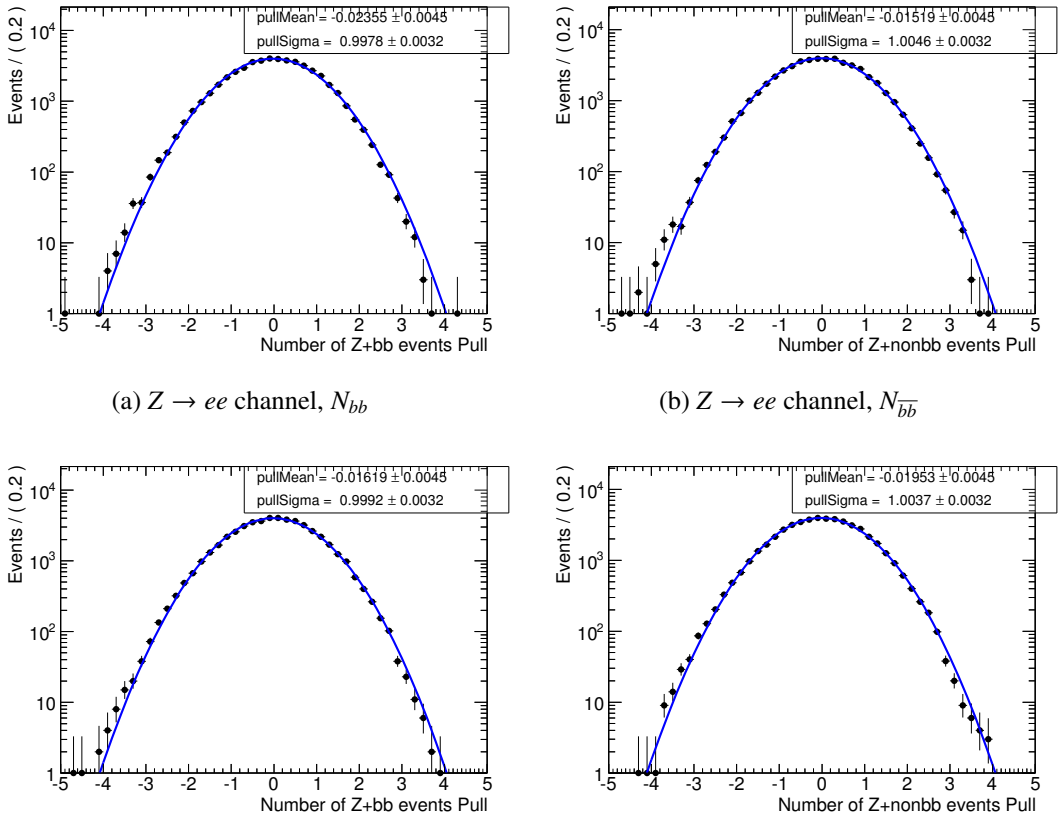

(a) $Z \to ee$ channel, N_{bb}

(b) $Z \to ee$ channel, $N_{\overline{bb}}$

(c) $Z \to \mu\mu$ channel, N_{bb}

(d) $Z \to \mu\mu$ channel, $N_{\overline{bb}}$

Figure C.1: Pull distributions for fitting with $\ln(P_b/P_l)$. Left side: N_{bb}, right side: $N_{\overline{bb}}$

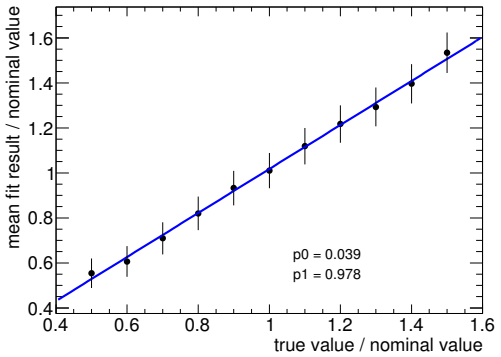

(a) $Z \to ee$ channel, N_{bb}

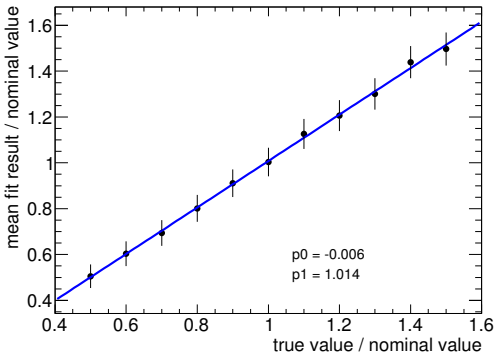

(b) $Z \to ee$ channel, $N_{\overline{bb}}$

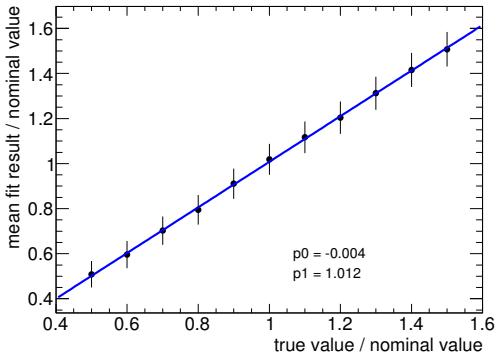

(c) $Z \to \mu\mu$ channel, N_{bb}

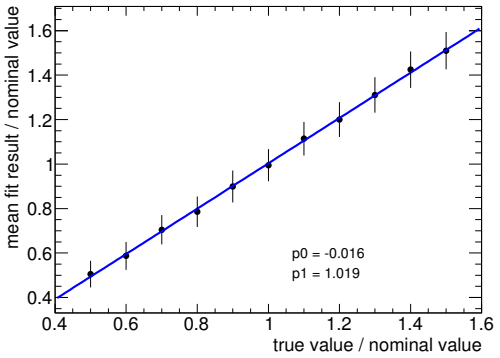

(d) $Z \to \mu\mu$ channel, $N_{\overline{bb}}$

Figure C.2: Linearity distributions for fitting with $\ln(P_b/P_l)$. The error bars in these plots do not represent the statistical uncertainty, but the RMS of the fitted values. Left side: N_{bb}, right side: $N_{\overline{bb}}$

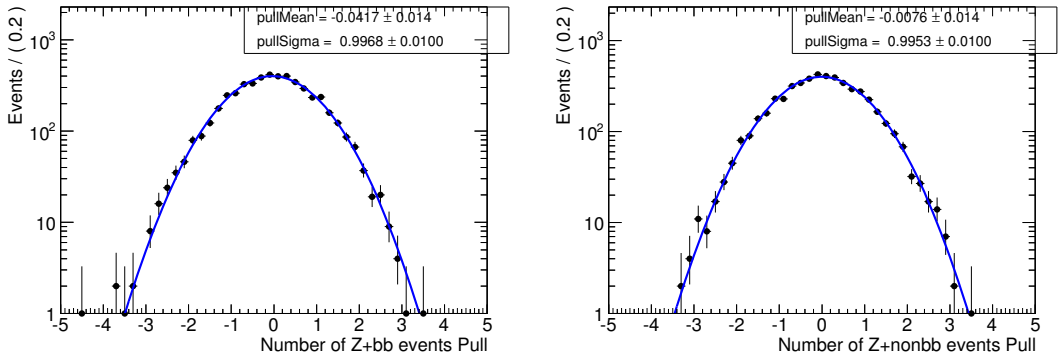

(a) $\ln(P_b/P_l)$, N_{bb} (b) $\ln(P_b/P_l)$, $N_{\overline{bb}}$

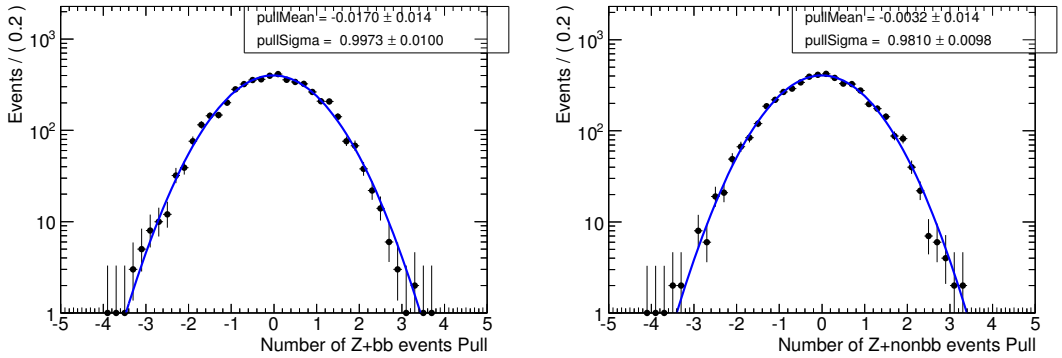

(c) $\ln(P_b/P_c)$, N_{bb} (d) $\ln(P_b/P_c)$, $N_{\overline{bb}}$

Figure C.3: Pull distributions for the combined fit with $\ln(P_b/P_c)$ and $\ln(P_b/P_l)$. Left side: N_{bb}, right side: $N_{\overline{bb}}$

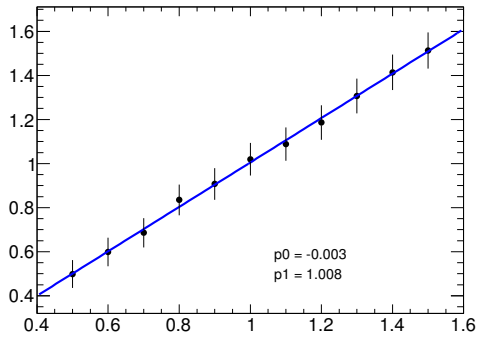

(a) $\ln(P_b/P_l)$, N_{bb}

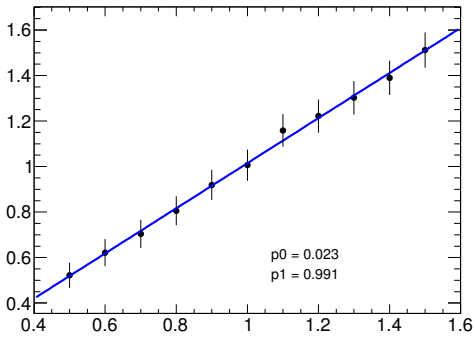

(b) $\ln(P_b/P_l)$, $N_{\overline{bb}}$

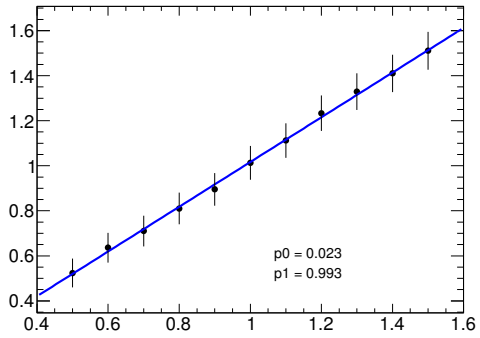

(c) $\ln(P_b/P_c)$, N_{bb}

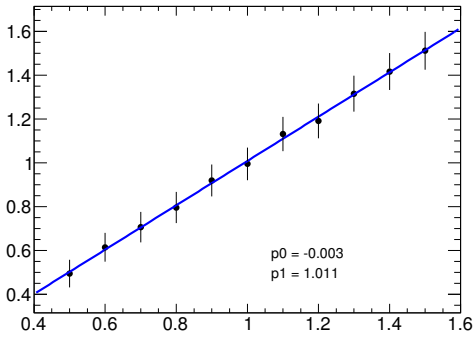

(d) $\ln(P_b/P_c)$, $N_{\overline{bb}}$

Figure C.4: Linearity distributions for the combined fit with $\ln(P_b/P_l)$ and $\ln(P_b/P_c)$. The error bars in these plots do not represent the statistical uncertainty, but the RMS of the fitted values. Left side: N_{bb}, right side: $N_{\overline{bb}}$

APPENDIX D

Validation of single-b fit

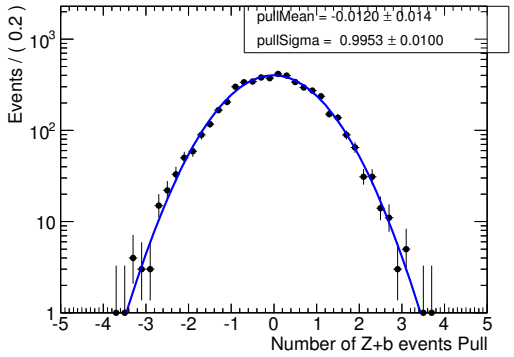

(a) $Z \to ee$ channel, N_b

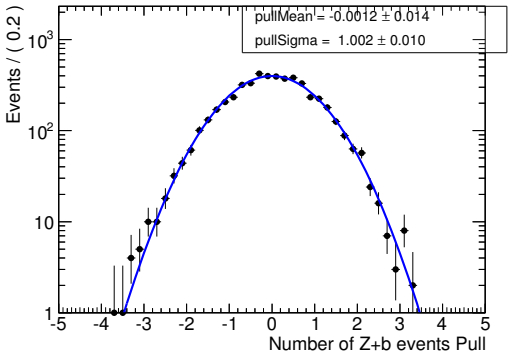

(b) $Z \to \mu\mu$ channel, N_b

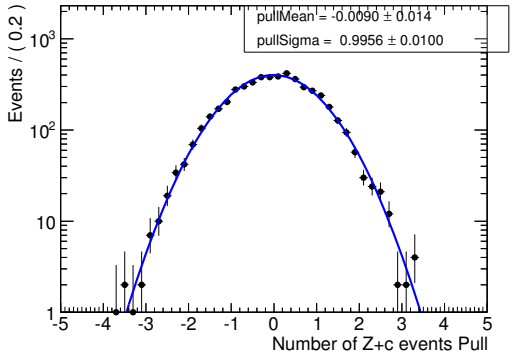

(c) $Z \to ee$ channel, N_c

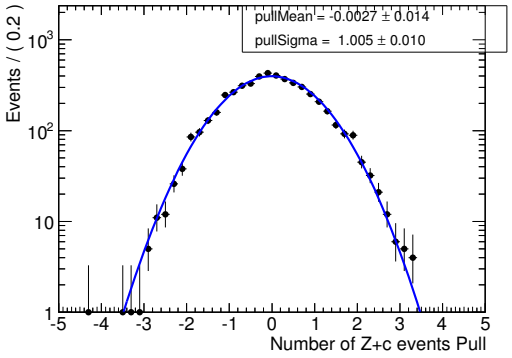

(d) $Z \to \mu\mu$ channel, N_c

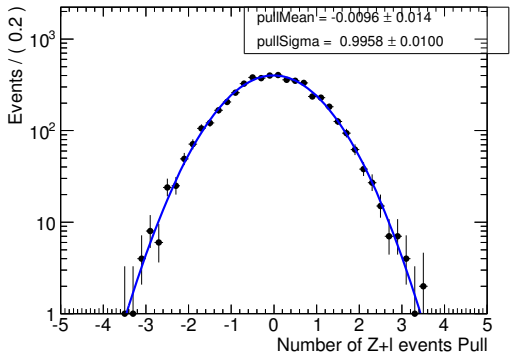

(e) $Z \to ee$ channel, N_l

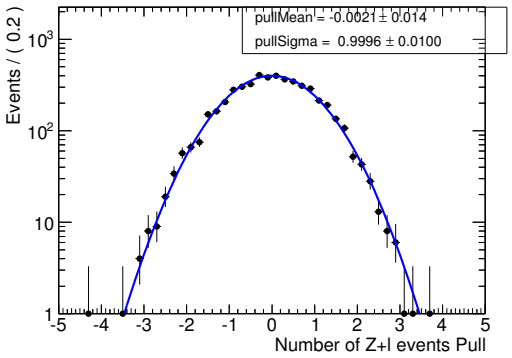

(f) $Z \to \mu\mu$ channel, N_l

Figure D.1: Pull distributions for the single-b fit using $\ln(P_b/P_l)$ as a fit variable. Left side: electron channel, right side: muon channel

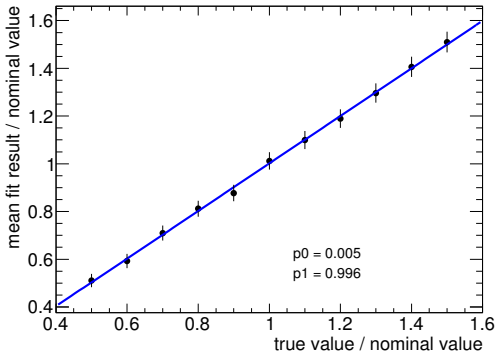

(a) $Z \to ee$ channel, N_b

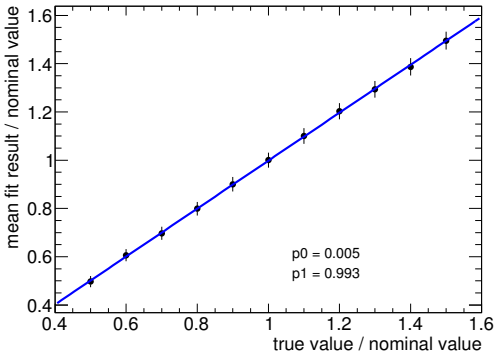

(b) $Z \to \mu\mu$ channel, N_b

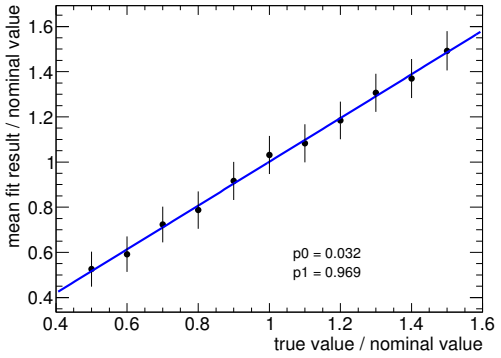

(c) $Z \to ee$ channel, N_c

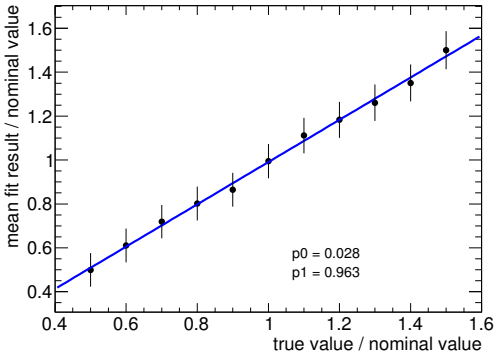

(d) $Z \to \mu\mu$ channel, N_c

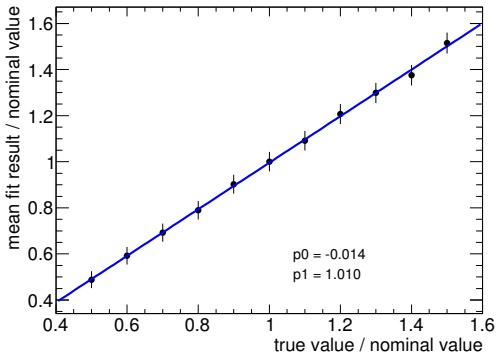

(e) $Z \to ee$ channel, N_l

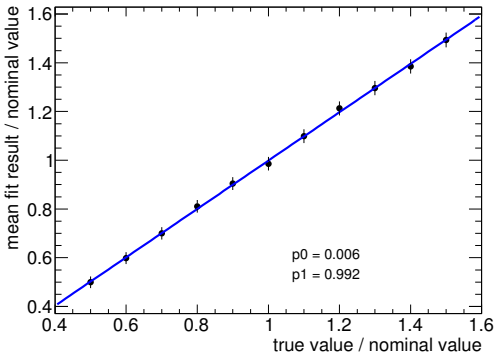

(f) $Z \to \mu\mu$ channel, N_l

Figure D.2: Linearity for the single-b fit using $\ln(P_b/P_l)$ as a fit variable. The error bars in these plots do not represent the statistical uncertainty, but the RMS of the fitted values. Left side: electron channel, right side: muon channel

Bibliography

[1] F. Abe et al., "Observation of top quark production in $\bar{p}p$ collisions", *Phys.Rev.Lett.* 74 (1995) 2626–2631, DOI: 10.1103/PhysRevLett.74.2626, arXiv:hep-ex/9503002 [hep-ex].

[2] S. Abachi et al., "Observation of the top quark", *Phys.Rev.Lett.* 74 (1995) 2632–2637, DOI: 10.1103/PhysRevLett.74.2632, arXiv:hep-ex/9503003 [hep-ex].

[3] K. Kodama et al., "Observation of tau neutrino interactions", *Phys.Lett.* B504 (2001) 218–224, DOI: 10.1016/S0370-2693(01)00307-0, arXiv:hep-ex/0012035 [hep-ex].

[4] G. Aad et al., "Observation of a new particle in the search for the Standard Model Higgs boson with the ATLAS detector at the LHC", *Phys.Lett.* B716 (2012) 1–29, DOI: 10.1016/j.physletb.2012.08.020, arXiv:1207.7214 [hep-ex].

[5] S. Chatrchyan et al., "Observation of a new boson at a mass of 125 GeV with the CMS experiment at the LHC", *Phys.Lett.* B716 (2012) 30–61, DOI: 10.1016/j.physletb.2012.08.021, arXiv:1207.7235 [hep-ex].

[6] F. Englert and R. Brout, "Broken Symmetry and the Mass of Gauge Vector Mesons", *Phys. Rev. Lett.* 13 (9 Aug. 1964) 321–323, DOI: 10.1103/PhysRevLett.13.321, URL: http://link.aps.org/doi/10.1103/PhysRevLett.13.321.

[7] P. Higgs, "Broken symmetries, massless particles and gauge fields", *Physics Letters* 12.2 (1964) 132 –133, ISSN: 0031-9163, DOI: http://dx.doi.org/10.1016/0031-9163(64)91136-9, URL: http://www.sciencedirect.com/science/article/pii/0031916364911369.

[8] P. W. Higgs, "Broken Symmetries and the Masses of Gauge Bosons", *Phys. Rev. Lett.* 13 (16 Oct. 1964) 508–509, DOI: 10.1103/PhysRevLett.13.508, URL: http://link.aps.org/doi/10.1103/PhysRevLett.13.508.

[9] G. S. Guralnik, C. R. Hagen and T. W. B. Kibble, "Global Conservation Laws and Massless Particles", *Phys. Rev. Lett.* 13 (20 Nov. 1964) 585–587, DOI: 10.1103/PhysRevLett.13.585, URL: http://link.aps.org/doi/10.1103/PhysRevLett.13.585.

[10] P. W. Higgs, "Spontaneous Symmetry Breakdown without Massless Bosons", *Phys. Rev.* 145 (4 May 1966) 1156–1163, DOI: 10.1103/PhysRev.145.1156, URL: http://link.aps.org/doi/10.1103/PhysRev.145.1156.

[11] T. W. B. Kibble, "Symmetry Breaking in Non-Abelian Gauge Theories", *Phys. Rev.* 155 (5 Mar. 1967) 1554–1561, DOI: 10.1103/PhysRev.155.1554, URL: http://link.aps.org/doi/10.1103/PhysRev.155.1554.

[12] G. Chiodini et al., "Measurement of the production cross-sections of at least one and at least two b-jets in association with a Z boson in proton-proton collisions at 7 TeV with the ATLAS detector", tech. rep. ATL-COM-PHYS-2014-037, CERN, Jan. 2014.

[13] (.) Evans and (.) Bryant, "LHC Machine", *JINST* 3 (2008) S08001, DOI: 10.1088/1748-0221/3/08/S08001.

[14] C. Lefèvre, "The CERN accelerator complex. Complexe des accélérateurs du CERN", Dec. 2008.

[15] URL: https://twiki.cern.ch/twiki/bin/view/AtlasPublic/MuonPerformancePublicPlots.

[16] T. A. Collaboration, "The ATLAS Experiment at the CERN Large Hadron Collider", *Journal of Instrumentation* 3.08 (2008) S08003, URL: http://stacks.iop.org/1748-0221/3/i=08/a=S08003.

[17] J. Pequenao, "Computer generated image of the whole ATLAS detector", Mar. 2008.

[18] J. Pequenao, "Computer generated image of the ATLAS inner detector", Mar. 2008.

[19] "Performance of primary vertex reconstruction in proton-proton collisions at $\sqrt{s}$ =7 TeV in the ATLAS experiment", tech. rep. ATLAS-CONF-2010-069, CERN, July 2010.

[20] J. Pequenao, "Computer Generated image of the ATLAS calorimeter", Mar. 2008.

[21] J. Beringer et al., "Review of Particle Physics (RPP)", *Phys.Rev.* D86 (2012) 010001, DOI: 10.1103/PhysRevD.86.010001.

[22] G. Aad et al., "Improved luminosity determination in pp collisions at $\sqrt{s}$ = 7 TeV using the ATLAS detector at the LHC", *Eur.Phys.J.* C73 (2013) 2518, DOI: 10.1140/epjc/s10052-013-2518-3, arXiv:1302.4393 [hep-ex].

[23] D. Griffiths, *Introduction to elementary particles*, New York: Wiley, 1987, ISBN: 0471603864.

[24] I. Aitchison, *Gauge theories in particle physics a practical introduction*, Bristol Philadelphia: Institute of Physics Pub, 2003, ISBN: 9780585445502.

[25] S. Glashow, "Partial Symmetries of Weak Interactions", *Nucl.Phys.* 22 (1961) 579–588, DOI: 10.1016/0029-5582(61)90469-2.

[26] S. Weinberg, "A Model of Leptons", *Phys.Rev.Lett.* 19 (1967) 1264–1266, DOI: 10.1103/PhysRevLett.19.1264.

[27] A. Salam, "Weak and Electromagnetic Interactions", *Conf.Proc.* C680519 (1968) 367–377.

[28] J. C. Collins, D. E. Soper and G. F. Sterman, "Factorization of Hard Processes in QCD", *Adv.Ser.Direct.High Energy Phys.* 5 (1988) 1–91, arXiv:hep-ph/0409313 [hep-ph].

[29] L. Lipatov, "The parton model and perturbation theory", *Sov.J.Nucl.Phys.* 20 (1975) 94–102.

[30] V. Gribov and L. Lipatov, "e+ e- pair annihilation and deep inelastic e p scattering in perturbation theory", *Sov.J.Nucl.Phys.* 15 (1972) 675–684.

[31] G. Altarelli and G. Parisi, "Asymptotic Freedom in Parton Language", *Nucl.Phys.* B126 (1977) 298, DOI: 10.1016/0550-3213(77)90384-4.

[32] Y. L. Dokshitzer, "Calculation of the Structure Functions for Deep Inelastic Scattering and e+ e- Annihilation by Perturbation Theory in Quantum Chromodynamics.", *Sov.Phys.JETP* 46 (1977) 641–653.

[33] A. Martin et al., "Parton distributions for the LHC", *Eur.Phys.J.* C63 (2009) 189–285, DOI: 10.1140/epjc/s10052-009-1072-5, arXiv:0901.0002 [hep-ph].

[34] G. Aad et al., "Measurement of underlying event characteristics using charged particles in pp collisions at $\sqrt{s} = 900GeV$ and 7 TeV with the ATLAS detector", *Phys.Rev.* D83 (2011) 112001, DOI: 10.1103/PhysRevD.83.112001, arXiv:1012.0791 [hep-ex].

[35] V. Sudakov, "Vertex parts at very high-energies in quantum electrodynamics", *Sov.Phys.JETP* 3 (1956) 65–71.

[36] X. Artru and G. Mennessier, "String model and multiproduction", *Nucl.Phys.* B70 (1974) 93–115, DOI: 10.1016/0550-3213(74)90360-5.

[37] S. Drell and T.-M. Yan, "Massive Lepton Pair Production in Hadron-Hadron Collisions at High-Energies", *Phys.Rev.Lett.* 25 (1970) 316–320, DOI: 10.1103/PhysRevLett.25.316.

[38] J. M. Campbell, J. Huston and W. Stirling, "Hard Interactions of Quarks and Gluons: A Primer for LHC Physics", *Rept.Prog.Phys.* 70 (2007) 89, DOI: 10.1088/0034-4885/70/1/R02, arXiv:hep-ph/0611148 [hep-ph].

[39] G. Aad et al., "Measurement of the production cross section of jets in association with a Z boson in pp collisions at $\sqrt{s} = 7$ TeV with the ATLAS detector", *JHEP* 1307 (2013) 032, DOI: 10.1007/JHEP07(2013)032, arXiv:1304.7098 [hep-ex].

[40] R. Frederix et al., "W and $Z/\gamma*$ boson production in association with a bottom-antibottom pair", *JHEP* 1109 (2011) 061, DOI: 10.1007/JHEP09().01()061, arXiv:1106.6019 [hep-ph].

[41] F. Febres Cordero, L. Reina and D. Wackeroth, "W- and Z-boson production with a massive bottom-quark pair at the Large Hadron Collider", *Phys.Rev.* D80 (2009) 034015, DOI: 10.1103/PhysRevD.80.034015, arXiv:0906.1923 [hep-ph].

[42] J. M. Campbell and R. K. Ellis, "Radiative corrections to Z b anti-b production", *Phys.Rev.* D62 (2000) 114012, DOI: 10.1103/PhysRevD.62.114012, arXiv:hep-ph/0006304 [hep-ph].

[43] J. M. Campbell and R. Ellis, "MCFM for the Tevatron and the LHC", *Nucl.Phys.Proc.Suppl.* 205-206 (2010) 10–15, DOI: 10.1016/j.nuclphysbps.2010.08.011, arXiv:1007.3492 [hep-ph].

[44] F. Febres Cordero, L. Reina and D. Wackeroth, "NLO QCD corrections to $Zb\bar{b}$ production with massive bottom quarks at the Fermilab Tevatron", *Phys.Rev.* D78 (2008) 074014, DOI: 10.1103/PhysRevD.78.074014, arXiv:0806.0808 [hep-ph].

[45] A. Stange, W. J. Marciano and S. Willenbrock, "Associated production of Higgs and weak bosons, with H to b anti-b, at hadron colliders", *Phys.Rev.* D50 (1994) 4491–4498, DOI: 10.1103/PhysRevD.50.4491, arXiv:hep-ph/9404247 [hep-ph].

[46] T. Sjostrand et al., "Pythia 6.3 physics and manual" (2003), arXiv:hep-ph/0308153 [hep-ph].

[47] G. Corcella et al., "HERWIG 6: An Event generator for hadron emission reactions with interfering gluons (including supersymmetric processes)", *JHEP* 0101 (2001) 010, DOI: 10.1088/1126-6708/2001/01/010, arXiv:hep-ph/0011363 [hep-ph].

[48] M. L. Mangano et al., "ALPGEN, a generator for hard multiparton processes in hadronic collisions", *JHEP* 0307 (2003) 001, DOI: 10.1088/1126-6708/2003/07/001, arXiv:hep-ph/0206293 [hep-ph].

[49] T. Gleisberg et al., "Event generation with SHERPA 1.1", *JHEP* 0902 (2009) 007, DOI: 10.1088/1126-6708/2009/02/007, arXiv:0811.4622 [hep-ph].

[50] J. Butterworth, J. R. Forshaw and M. Seymour, "Multiparton interactions in photoproduction at HERA", *Z.Phys.* C72 (1996) 637–646, DOI: 10.1007/s002880050286, arXiv:hep-ph/9601371 [hep-ph].

[51] M. Bahr et al., "Herwig++ Physics and Manual", *Eur.Phys.J.* C58 (2008) 639–707, DOI: 10.1140/epjc/s10052-008-0798-9, arXiv:0803.0883 [hep-ph].

[52] M. L. Mangano, M. Moretti and R. Pittau, "Multijet matrix elements and shower evolution in hadronic collisions: $Wb\bar{b}$ + n jets as a case study", *Nucl.Phys.* B632 (2002) 343–362, DOI: 10.1016/S0550-3213(02)00249-3, arXiv:hep-ph/0108069 [hep-ph].

[53] S. Frixione and B. R. Webber,
"Matching NLO QCD computations and parton shower simulations",
JHEP 0206 (2002) 029, DOI: 10.1088/1126-6708/2002/06/029,
arXiv:hep-ph/0204244 [hep-ph].

[54] P. Nason,
"A New method for combining NLO QCD with shower Monte Carlo algorithms",
JHEP 0411 (2004) 040, DOI: 10.1088/1126-6708/2004/11/040,
arXiv:hep-ph/0409146 [hep-ph].

[55] S. Frixione, P. Nason and C. Oleari, "Matching NLO QCD computations with Parton Shower simulations: the POWHEG method", *JHEP* 0711 (2007) 070,
DOI: 10.1088/1126-6708/2007/11/070, arXiv:0709.2092 [hep-ph].

[56] S. Alioli et al., "A general framework for implementing NLO calculations in shower Monte Carlo programs: the POWHEG BOX", *JHEP* 1006 (2010) 043,
DOI: 10.1007/JHEP06(2010)043, arXiv:1002.2581 [hep-ph].

[57] D. Lange, "The EvtGen particle decay simulation package",
Nucl.Instrum.Meth. A462 (2001) 152–155,
DOI: 10.1016/S0168-9002(01)00089-4.

[58] B. P. Kersevan and E. Richter-Was, "The Monte Carlo event generator AcerMC versions 2.0 to 3.8 with interfaces to PYTHIA 6.4, HERWIG 6.5 and ARIADNE 4.1",
Comput.Phys.Commun. 184 (2013) 919–985, DOI: 10.1016/j.cpc.2012.10.032,
arXiv:hep-ph/0405247 [hep-ph].

[59] URL: http://amcatnlo.web.cern.ch/amcatnlo/.

[60] J. Alwall et al., "MadGraph 5 : Going Beyond", *JHEP* 1106 (2011) 128,
DOI: 10.1007/JHEP06(2011)128, arXiv:1106.0522 [hep-ph].

[61] S. Agostinelli et al., "GEANT4: A Simulation toolkit",
Nucl.Instrum.Meth. A506 (2003) 250–303,
DOI: 10.1016/S0168-9002(03)01368-8.

[62] R. Brun and F. Rademakers, "ROOT: An object oriented data analysis framework",
Nucl.Instrum.Meth. A389 (1997) 81–86, DOI: 10.1016/S0168-9002(97)00048-X.

[63] A. Bundock et al.,
"Measurement of Zb and Zbb cross sections with 4.6 fb-1 of 7 TeV ATLAS data",
tech. rep. ATL-COM-PHYS-2012-1504, CERN, Oct. 2012.

[64] H.-L. Lai et al., "New parton distributions for collider physics",
Phys.Rev. D82 (2010) 074024, DOI: 10.1103/PhysRevD.82.074024,
arXiv:1007.2241 [hep-ph].

[65] R. D. Ball et al., "A first unbiased global NLO determination of parton distributions and their uncertainties", *Nucl.Phys.* B838 (2010) 136–206,
DOI: 10.1016/j.nuclphysb.2010.05.008, arXiv:1002.4407 [hep-ph].

[66] E. Barberio, B. van Eijk and Z. Was,
"PHOTOS: A Universal Monte Carlo for QED radiative corrections in decays",
Comput.Phys.Commun. 66 (1991) 115–128,
DOI: 10.1016/0010-4655(91)90012-A.

[67] P. Golonka and Z. Was,
"PHOTOS Monte Carlo: A Precision tool for QED corrections in Z and W decays",
Eur.Phys.J. C45 (2006) 97–107, DOI: 10.1140/epjc/s2005-02396-4,
arXiv:hep-ph/0506026 [hep-ph].

[68] G. Aad et al., "Electron performance measurements with the ATLAS detector using the 2010 LHC proton-proton collision data", *Eur.Phys.J.* C72 (2012) 1909,
DOI: 10.1140/epjc/s10052-012-1909-1, arXiv:1110.3174 [hep-ex].

[69] "Expected electron performance in the ATLAS experiment",
tech. rep. ATL-PHYS-PUB-2011-006, CERN, Apr. 2011.

[70] M. Cacciari, G. P. Salam and G. Soyez, "The Anti-k(t) jet clustering algorithm",
JHEP 0804 (2008) 063, DOI: 10.1088/1126-6708/2008/04/063,
arXiv:0802.1189 [hep-ph].

[71] W. Lampl et al., "Calorimeter Clustering Algorithms: Description and Performance",
tech. rep. ATL-LARG-PUB-2008-002. ATL-COM-LARG-2008-003,
CERN, Apr. 2008.

[72] M. Cacciari, G. P. Salam and G. Soyez, "FastJet User Manual",
Eur.Phys.J. C72 (2012) 1896, DOI: 10.1140/epjc/s10052-012-1896-2,
arXiv:1111.6097 [hep-ph].

[73] M. Cacciari and G. P. Salam, "Dispelling the N^3 myth for the k_t jet-finder",
Phys.Lett. B641 (2006) 57–61, DOI: 10.1016/j.physletb.2006.08.037,
arXiv:hep-ph/0512210 [hep-ph].

[74] S. Catani et al.,
"Longitudinally invariant K_t clustering algorithms for hadron hadron collisions",
Nucl.Phys. B406 (1993) 187–224, DOI: 10.1016/0550-3213(93)90166-M.

[75] S. D. Ellis and D. E. Soper,
"Successive combination jet algorithm for hadron collisions",
Phys.Rev. D48 (1993) 3160–3166, DOI: 10.1103/PhysRevD.48.3160,
arXiv:hep-ph/9305266 [hep-ph].

[76] G. Aad et al., "Jet energy measurement with the ATLAS detector in proton-proton collisions at $\sqrt{s} = 7$ TeV", *Eur.Phys.J.* C73 (2013) 2304,
DOI: 10.1140/epjc/s10052-013-2304-2, arXiv:1112.6426 [hep-ex].

[77] M. Aharrouche et al., "Energy linearity and resolution of the ATLAS electromagnetic barrel calorimeter in an electron test-beam",
Nucl.Instrum.Meth. A568 (2006) 601–623, DOI: 10.1016/j.nima.2006.07.053,
arXiv:physics/0608012 [physics].

[78] "Data-Quality Requirements and Event Cleaning for Jets and Missing Transverse Energy Reconstruction with the ATLAS Detector in Proton-Proton Collisions at a Center-of-Mass Energy of *sqrts* = 7 TeV", tech. rep. ATLAS-CONF-2010-038, CERN, July 2010.

[79] F. Filthaut and C. Weiser, "Performance of b-Jet Identification in the ATLAS Experiment", tech. rep. ATL-COM-PHYS-2012-824, CERN, June 2012.

[80] "Performance of the ATLAS Secondary Vertex b-tagging Algorithm in 7 TeV Collision Data", tech. rep. ATLAS-CONF-2010-042, CERN, July 2010.

[81] "Measurement of the b-tag Efficiency in a Sample of Jets Containing Muons with $5 fb^{-}1$ of Data from the ATLAS Detector", tech. rep. ATLAS-CONF-2012-043, CERN, Mar. 2012.

[82] "Measuring the b-tag efficiency in a top-pair sample with $4.7 fb^{-}1$ of data from the ATLAS detector", tech. rep. ATLAS-CONF-2012-097, CERN, July 2012.

[83] G. Aad et al., "Performance of Missing Transverse Momentum Reconstruction in Proton-Proton Collisions at 7 TeV with ATLAS", *Eur.Phys.J.* C72 (2012) 1844, DOI: 10.1140/epjc/s10052-011-1844-6, arXiv:1108.5602 [hep-ex].

[84] "Expected photon performance in the ATLAS experiment", tech. rep. ATL-PHYS-PUB-2011-007, CERN, Apr. 2011.

[85] "Tau Reconstruction and Identification Performance in ATLAS", tech. rep. ATLAS-CONF-2010-086, CERN, Oct. 2010.

[86] "Performance of the ATLAS Electron and Photon Trigger in p-p Collisions at sqrts = 7 TeV in 2011", tech. rep. ATLAS-CONF-2012-048, CERN, May 2012.

[87] "Performance of the ATLAS muon trigger in 2011", tech. rep. ATLAS-CONF-2012-099, CERN, July 2012.

[88] J. Pumplin et al., "New generation of parton distributions with uncertainties from global QCD analysis", *JHEP* 0207 (2002) 012, arXiv:hep-ph/0201195 [hep-ph].

[89] "New ATLAS event generator tunes to 2010 data", tech. rep. ATL-PHYS-PUB-2011-008, CERN, Apr. 2011.

[90] P. M. Nadolsky et al., "Implications of CTEQ global analysis for collider observables", *Phys.Rev.* D78 (2008) 013004, DOI: 10.1103/PhysRevD.78.013004, arXiv:0802.0007 [hep-ph].

[91] URL: https://twiki.cern.ch/twiki/bin/viewauth/AtlasProtected/WZElectroweakCommonTopics2011.

[92] "A measurement of the ATLAS muon reconstruction and trigger efficiency using J/psi decays", tech. rep. ATLAS-CONF-2011-021, CERN, Mar. 2011.

[93] S. Heim et al., "Update of Electron Efficiency Plots (Sep 2013): For Approval", tech. rep. ATL-COM-PHYS-2013-1287, CERN, Sept. 2013.

[94] URL: https://twiki.cern.ch/twiki/bin/view/AtlasPublic/MuonPerformancePublicPlots.

[95] K. Nakamura et al., "Review of particle physics", *J.Phys.* G37 (2010) 075021, DOI: 10.1088/0954-3899/37/7A/075021.

[96] A. Ceccucci, Z. Ligeti and Y. Sakai, "The CKM quark-mixing matrix" (2008).

[97] "Measurements of multijet production cross sections in proton-proton collisions at 7 TeV center-of-mass energy with the ATLAS Detector", tech. rep. ATLAS-CONF-2010-084, CERN, Oct. 2010.

[98] D. Vladoiu, "Study of the Z+bb Production with the ATLAS Detector at the LHC", PhD thesis: LMU Munich, July 2013.

[99] W. Verkerke and D. P. Kirkby, "The RooFit toolkit for data modeling", *eConf* C0303241 (2003) MOLT007, arXiv:physics/0306116 [physics].

[100] F. James and M. Roos, "Minuit - a system for function minimization and analysis of the parameter errors and correlations", *Computer Physics Communications* 10.6 (1975) 343 –367, ISSN: 0010-4655, DOI: http://dx.doi.org/10.1016/0010-4655(75)90039-9, URL: http://www.sciencedirect.com/science/article/pii/0010465575900399.

[101] G. Aad et al., "Measurement of the cross-section for b^- jets produced in association with a Z boson at $\sqrt{s} = 7$ TeV with the ATLAS detector", *Phys.Lett.* B706 (2012) 295–313, DOI: 10.1016/j.physletb.2011.11.059, arXiv:1109.1403 [hep-ex].

[102] URL: https://twiki.cern.ch/twiki/bin/view/AtlasPublic/FlavourTaggingPublicResultsCollisionData.

[103] "Jet energy scale and its systematic uncertainty in proton-proton collisions at sqrt(s)=7 TeV with ATLAS 2011 data", tech. rep. ATLAS-CONF-2013-004, CERN, Jan. 2013.

[104] "Close-by Jet Effects on Jet Energy Scale Calibration in pp Collisions at sqrt(s)=7 TeV with the ATLAS Detector", tech. rep. ATLAS-CONF-2011-062, CERN, Apr. 2011.

[105] "Light-quark and Gluon Jets in ATLAS", tech. rep. ATLAS-CONF-2011-053, CERN, Apr. 2011.

[106] "Jet energy resolution and selection efficiency relative to track jets from in-situ techniques with the ATLAS Detector Using Proton-Proton Collisions at a Center of Mass Energy *sqrts* = 7 TeV", tech. rep. ATLAS-CONF-2010-054, CERN, July 2010.

[107] G. Aad et al., "Measurement of the top quark-pair production cross section with ATLAS in pp collisions at $\sqrt{s} = 7$ TeV", *Eur.Phys.J.* C71 (2011) 1577, DOI: 10.1140/epjc/s10052-011-1577-6, arXiv:1012.1792 [hep-ex].

[108] G. Aad et al., "Measurement of hard double-parton interactions in $W(\rightarrow l\nu)$+ 2 jet events at $\sqrt{s}$=7 TeV with the ATLAS detector", *New J.Phys.* 15 (2013) 033038, DOI: 10.1088/1367-2630/15/3/033038, arXiv:1301.6872 [hep-ex].

[109] G. Aad et al., "Measurement of the inclusive and dijet cross-sections of b^- jets in pp collisions at $\sqrt{s}$ = 7 TeV with the ATLAS detector", *Eur.Phys.J.* C71 (2011) 1846, DOI: 10.1140/epjc/s10052-011-1846-4, arXiv:1109.6833 [hep-ex].

[110] G. Aad et al.,
"Measurement of the inclusive $W^\pm$ and Z/gamma cross sections in the electron and muon decay channels in pp collisions at $\sqrt{s}$ = 7 TeV with the ATLAS detector", *Phys.Rev.* D85 (2012) 072004, DOI: 10.1103/PhysRevD.85.072004, arXiv:1109.5141 [hep-ex].

[111] S. Chatrchyan et al., "Measurement of the production cross sections for a Z boson and one or more b jets in pp collisions at $\sqrt{s}$ = 7 TeV" (2014), arXiv:1402.1521 [hep-ex].

List of Figures

List of Tables

Danksagung

Ich möchte an dieser Stelle die Gelegenheit nutzen, um mich bei alljenen zu bedanken, die maßgeblich zum Gelingen dieser Arbeit beigetragen haben.

Zunächst möchte ich mich bei Prof. Norbert Wermes bedanken. Er hat mir die Möglichkeit gegeben, in seiner Arbeitsgruppe und in der ATLAS Kollaboration mitzuwirken und diese in vielerlei Hinsicht aufregende Zeit in der Teilchenphysik an vorderster Front mitzuerleben und mitzugestalten. Ich möchte mich außerdem bei Dr. Sonja Hillert bedanken, die diese Analyse während der ersten zweieinhalb Jahre begleitet und mich permanent unterstützt hat. Insbesondere möchte ich mich aber dafür bedanken, dass sie mir auch danach immer mit Rat und Tat zur Seite gestanden und diese Arbeit Korrektur gelesen hat.

Ich möchte mich auch bei allen Kolleginnen und Kollegen bedanken, die die vergangenen Jahre in Bonn und Genf trotz aller Anstrengungen zu einer sehr angenehmen Zeit gemacht haben, auf die ich immer mit Freude zurückblicken werde. Sei es beispielsweise in zahllosen Kaffeepausen, bei Videoabenden, Wein- und Whiskyproben — es wurde nie langweilig!

Weiterhin möchte ich mich auch bei meinen lieben Freundinnen und Freunden außerhalb der Physik dafür bedanken, dass sie es mir verziehen haben, wenn ich nicht immer so viel Zeit für sie hatte, wie ich es eigentlich wollte. Ich danke meinen Eltern Gabi und Kalle für Ihre bedingungslose Unterstützung. Zu guter Letzt danke ich Judith dafür, dass sie mir immer zur Seite gestanden und mich in der stressigen Endphase dieser Arbeit ohne Wenn und Aber ertragen hat.